ISTANBUL TECHNICAL UNIVERSITY ★ GRADUATE SCHOOL OF SCIENCE
ENGINEERING AND TECHNOLOGY

STUDIES OF SPIN AND BEAM DYNAMICS AND ELECTRIC FIELD ISSUES FOR THE PROTON EDM EXPERIMENT IN AN ALL ELECTRIC STORAGE RING

Ph.D. THESIS

Selçuk HACIÖMEROĞLU

Department of Physics Engineering

Physics Engineering Programme

OCTOBER 2012

ISTANBUL TECHNICAL UNIVERSITY ★ GRADUATE SCHOOL OF SCIENCE
ENGINEERING AND TECHNOLOGY

STUDIES OF SPIN AND BEAM DYNAMICS AND ELECTRIC FIELD ISSUES FOR THE PROTON EDM EXPERIMENT IN AN ALL ELECTRIC STORAGE RING

Ph.D. THESIS

Selçuk HACIÖMEROĞLU
(509052103)

Department of Physics Engineering

Physics Engineering Programme

Thesis Advisor: Prof. Dr. Cenap Ş. ÖZBEN

OCTOBER 2012

İSTANBUL TEKNİK ÜNİVERSİTESİ ★ FEN BİLİMLERİ ENSTİTÜSÜ

ELEKTRİKSEL SAKLAMA HALKASINDA PROTON EDM DENEYİ İÇİN SPİN ve IŞIN DİNAMİĞİ İLE ELEKTRİK ALAN KONULARINDA ÇALIŞMALAR

DOKTORA TEZİ

Selçuk HACIÖMEROĞLU
(509052103)

Fizik Mühendisliği Anabilim Dalı

Fizik Mühendisliği Programı

Tez Danışmanı: Prof. Dr. Cenap Ş. ÖZBEN

EKİM 2012

Selçuk HACIÖMEROĞLU, a Ph.D. student of ITU Graduate School of Science 509052103 successfully defended the thesis entitled **"STUDIES OF SPIN AND BEAM DYNAMICS AND ELECTRIC FIELD ISSUES FOR THE PROTON EDM EXPERIMENT IN AN ALL ELECTRIC STORAGE RING"**, which he prepared after fulfilling the requirements specified in the associated legislations, before the jury whose signatures are below.

Thesis Advisor : **Prof. Dr. Cenap Ş. ÖZBEN** ....
İstanbul Technical University

Co-advisor : **Dr. Yannis K. SEMERTZIDIS** ....
Brookhaven National Laboratory

Jury Members : **Prof. Dr. Cem GÜÇLÜ** ....
İstanbul Technical University

Prof. Dr. Serkant Ali ÇETİN ....
Doğuş University

Assoc. Prof. Dr. A. İskender REYHANCAN ....
İstanbul Technical University

Assoc. Prof. Dr. Yeşim ÖKTEM ....
İstanbul University

Assist. Prof. Dr. Zuhal ER ....
İstanbul Technical University

Date of Submission : 12 September 2012
Date of Defense : 12 October 2012

Hayatımın her aşamasında desteklerini gördüğüm anneme, babama, kardeşlerime ve eşime,

FOREWORD

I am grateful to all the people who helped and supported me during my PhD study. While it is difficult to name all of them here, I would like to acknowledge a few of them explicitly.

Firstly, I have been really fortunate to work with my thesis advisor Dr. Cenap Ş. Özben from Istanbul Technical University (ITU), my supervisor Dr. Yannis K. Semertzidis and Dr. William Morse from Brookhaven National Laboratory (BNL). I would like to thank them for all their efforts, encouragement and wise advises. It is a pleasure to work with them, and have them as friends.

Then, I would like to thank Richard Larsen, John Benante, Dr. Peter Thieberger, Leonard DeSanto, Peter Cameron and Russell Burns from BNL, for all their contributions to my thesis. They have always been eager to help me.

I also thank the comitee members for their time and suggestions.

Additionally, I would like to thank Dr. Richard Talman and Dr. Yuri Orlov from Cornell University for their valuable discussions.

I am specially grateful to Dr. Alfredo Luccio for making my life easier at BNL.

Finally, I would like to thank my parents, sister, brother and wife for their full support both in my life and PhD study.

October 2012

Selçuk HACIÖMEROĞLU
(Physicist)

TABLE OF CONTENTS

ABBREVIATIONS

SM : Standard Model
SUSY : Supersymmetry
EDM : Electric Dipole Moment
MDM : Magnetic Dipole Moment
HV : High Voltage
CP : Charge-Parity
CPT : Charge-Parity-Time
QCD : Quantum Chromodynamics
SCT : Spin Coherence Time
CW : Clockwise
CCW : Counterclockwise
BPM : Beam Position Monitor
RF : Radio Frequency
HPR : High Pressure Water Rinsing
GCIB : Gas Cluster Ion Beams
HV : High Voltage
DAQ : Data Acquisition
I/O : Input Output

LIST OF TABLES

Page

LIST OF FIGURES

Page

STUDIES OF SPIN AND BEAM DYNAMICS AND ELECTRIC FIELD ISSUES FOR THE PROTON EDM EXPERIMENT IN AN ALL ELECTRIC STORAGE RING

SUMMARY

Search for permanent electric dipole moment (EDM) of fundamental particles is an important subject in particles physics. Because, measurement of an EDM above the limits of Standard Model means a new source of CP violation, hence “new physics”.

There are various critical questions concerning an EDM experiment in an all-electric storage ring. One of them is about the spin coherence time (SCT), which indicates the alignment of the spin and momentum in the same direction. For an EDM measurement, the spin precession due to systematic errors should be less than the EDM effect. Therefore, one needs to know the effects of the straight sections, field index, fringe fields etc. on SCT.

This thesis concerns the proposed proton EDM experiment in Brookhaven National Laboratory in USA. It includes two parts. In the first part, the beam and spin dynamics of the proton in an electrostatic storage ring is simulated using 4^{th} order Runge Kutta Method. Thus, the SCT of the proton is calculated for various cases of ring design and initial conditions. It is seen that the SCT of the proton is long enough to make the experiment with a reasonable lattice design and the desired sensitivity of 10^{-29} $e \cdot cm$. Besides, some of the parameters of magnetic rings, such as phase slip factor and dispersion and betatron oscillation are found to have different behaviour in electric and magnetic rings. Finally, it is observed that electric rings provide a compensation mechanism for g-2 precession, which increases the SCT by an order of magnitude. To our knowledge, this effect is first mentioned in this thesis.

In the second part of the thesis, high voltage tests were conducted on metal plates. Since the electrostatic storage ring will utilize plates with high electric fields (i.e, 10.5 MV/m for 3 cm gap), the plates should be conditioned prior to use. Otherwise it sparks and damages the plates and the uniformity of the electric field. The achievability and stability of the high gradient is another critical question. There are some methods for conditioning metal surfaces. In this study, we used electropolished and high pressure water rinsed plates and then made spark conditioning in small gaps. Before the conditioning, at 1 mm of gap, the plates could have maximum electric field of 8 MV/m with 6 nA of dark current. Then they were sparking. After the conditioning, it increased to 48 MV/m with 74nA and the β parameter of the surface which defines its condition decreased to 20% of its initial value.

ELEKTRİKSEL SAKLAMA HALKASINDA PROTON EDM DENEYİ İÇİN SPİN ve IŞIN DİNAMİĞİ İLE ELEKTRİK ALAN KONULARINDA ÇALIŞMALAR

ÖZET

Yük (C), parite (P) ve zaman (T) simetrisi Standart Modelde önemli yer tutar. Hiçbir fiziksel süreçte üçünün toplu ihlali (CPT-ihlali) olmadığı kabul edilmekle birlikte, bazı süreçlerde tekli ya da ikili olarak simetri ihlalleri gözlenmiştir.

Standart Model CP-ihlalini CKM mekanizması ile açıklamıştır. CKM mekanizması, elemanları deneysel verilerle belirlenen CKM matrisi vasıtasıyla d, s ve b kuarkları arasındaki geçişleri belirler. CKM matrisinin içerdiği bir faz faktörü CP-ihlaline yol açmaktadır. Bu mekanizma K^0 ve B^0 bozunmalarındaki CP-ihlalini açıklayabilmektedir. Bununla birlikte, Standart Modelde açıklanmayan CP-ihlalleri de olduğu düşünülmektedir. Örneğin evrendeki madde-antimadde asimeterisini açıklamak için Sakharov, CKM mekanizması ile açıklanamayacak kadar büyük bir CP-ihlalini gerekli bulmuştur. Öte yandan SUSY, Sol-sağ süpersimetrik model, Weinberg çoklu-Higgs modeli gibi Standart Model ötesi bazı modeller de daha güçlü CP-ihlali kaynakları önermektedir.

Elektrik dipol momenti (EDM) CP-ihlali yapan bir fiziksel büyüklüktür. Standart Model, temel parçacıklar için çok küçük EDM değerleri öngörmektedir (örneğin nötron için 10^{-32}e ·cm). Günümüz teknolojisiyle henüz bu hassasiyette deneyler yapılamamaktadır. Fakat yukarıda bahsedilen modeller günümüz deneysel limitlerine çok yakın değerler öngörmektedir. Bu yüzden temel parçacıklar için EDM deneyleri, aynı zamanda yukarıdaki modelleri de test edecektir ve olası bir sıfırdan farklı ölçüm "yeni fizik" anlamına gelmektedir.

ABD'de, Brookhaven Ulusal Laboratuvarı'nda gerçekleştirilmesi önerilen "saklama halkasında proton EDM deneyi", proton EDM'ini 10^{-29} e ·cm hassasiyetle ölçmeyi önermektedir. Bu önerilen metotta proton halka içinde "sihirli momentum" değerinde 1000 s kadar saklanacaktır. Sihirli momentum değeri parçacığın g-faktörüne bağlı olarak belirlenir. Proton için yaklaşık 0.7007 GeV/c'dir. Parçacık sihirli momentum değerinde halka içinde saklanabilirse, spini g-2 presesyonuna maruz kalmaz. Dolayısıyla spin ve momentum arasındaki bu açıyı değiştirebilecek tek etki, EDM ve MDM (manyetik dipol momenti)'dir. Eğer halka içindeki manyetik alan bir şekilde sıfırlanabilirse deney sonunda olası bir sıfırdan farklı açı ölçümü parçacığın EDM'inin de ölçümü demektir. Ne var ki, bir halkanın içinde tamamı sihirli momentuma sahip çok sayıda parçacık saklanamaz. Bu yüzden parçacıkların spin ve momentumu arasındaki açı bir süre sonra çok büyür ve EDM sinyali görünmez olur. 1000s sonunda açının 1 rad olması için gereken süre spin uyum süresi (SUS) olarak tanımlanmıştır.

Saklama halkasında EDM deneyi yapılmadan önce ışın ve spin dinamiği bazı kritik sorular cevaplanmalıdır: Örneğin halkaya nasıl bir ışın sığdırılabileceği, SUS'un uzunluğu vb. önceden tahmin edilmelidir.

Saklama halkasındaki ışının spin uyum süresinin saklama halkasındaki toplam düz bölge uzunluğu, elektrik alan indisi, levhaların kenarlarındaki saçak alanları gibi çeşitli parametrelerden etkilendiği bilinmektedir. Bu konuda manyetik alanlı halkalar için çesitli analitik hesaplar yapılmış olmakla birlikte, elektrik alanla ilgili yeterli analitik çalışma bulunmamaktadır. Manyetik halka çözümleri kinetik enerji sabit tutularak yapılmıştır ve parçacığın elektrik alan içindeki momentumu elektrik alana çok kuvvetli bir şekilde bağlı olduğu için manyetik alan için yapılan çözümler elektrik alanda kullanılamamaktadır. Bu yüzden Runge-Kutta gibi nümerik integrasyon yöntemleri, elektriksel saklama halkasındaki ışın ve spin dinamiği problemlerinde önemli yer tutmaktadır.

Bu tez, yukarıda bahsedilen proton EDM deneyi ile ilgili çalışmalar içermektedir ve iki kısımdan oluşur. Birinci kısımda 4. dereceden Runge Kutta Metodu kullanılarak protonun elektrostatik saklama halkasındaki ışın ve spin dinamiği incelenmiş, böylece protonun SUS'u hesaplanmış, halkadaki düz bolgelerin uzunluğunun ve alan indisinin SUS'u nasıl etkilediği tespit edilmiş ve manyetik halka ile elektrik halka arasındaki temel farklar ortaya konmuştur.

Simulasyonlarda saklama halkası ardışık 14 adet kıvrılan ve düz bölgeden oluşmaktadır. Düz bölgelerin toplam uzunluğu 15-30 m mertebesinde ve kıvrılan bölgelerin toplam çevresi de yaklaşık 250 m'dir. Elektrik alan kıvrılan bölgelerde belli bir m alan indisi ile yaklaşık 10.5 MV/m olarak uygulanmaktadır. Düz bölgelerde ise elektrik alan bulunmamaktadır. Düz ve kıvrılan bölgeler arasındaki saçak alanları, SUS'un kısalmasında önemli yer tutarlar. Bu saçak alanları, “sert kenar” şeklinde modellenmiştir. Bu modele göre geçişlerde toplam enerji sabit kalacak şekilde potansiyel ve kinetik enerji dönüşümleri yapılarak parçacığın hareketine müdahale edilmektedir. Simülasyonlar tek proton üzerinden yapılıp, protonun başlangıç koşullarına göre spin ve momentumunun evrimi incelenmiştir.

Simulasyonlar sonunda protonun SUS'unun, deneyi yukarıda anlatılan örgü tasarımıyla ve istenen hassasiyetle (10^{-29}e·cm) yapmak için yeterli olacağı görülmüştür. Düz bölgelerin uzunluğu için çok sıkı bir kısıtlama olmadığı, gerektiği durumlarda uzatılabileceği gözlenmiştir.

Bunun yanısıra manyetik halkalarda önemli parametreler olan faz kayma faktörü, dispersiyon, betatron salınımı gibi bazı kavramların elektrik ve manyetik halkalarda farklı davranışlar sergilediği gözlenmiştir.

Son olarak, elektrostatik halkanın g-2 presesyonu için bir telafi mekanizması sağladığı, dolayısıyla SUS'u uzattığı gözlenmiştir. Bu faktör dikkate alınmadığında salınımlardan ötürü parçacığın momentumu “sihirli momentum” dan sürekli farklı olacağı için SUS'un çok kısa olacağı düşünülür. Fakat simulasyonlarda parçacık üzerine etkiyen elektrik alanın parçacığın hız vektörüne göre farklı ağırlıklarda spinini etkilediği, bu etkinin de SUS'u beklenmedik ölçüde artırdığı görülmüştür. Bu etki bildiğimiz kadarıyla ilk defa bu çalışmada belirtilmektedir.

Elektrostatik halka vakum içinde yüksek elektrik alan taşıyan levhalar içereceğinden (3 cm mesafede 10.5 MV/m), levhalar kullanılmadan önce işlenmelidir. Aksi halde kıvılcımlar oluşur ve bu da elektrik alanın düzgünlüğüne zarar verir. Bu bağlamda, 3 cm'lik mesafede en fazla ne kadar elektrik alana ulaşılabileceği, bu elektrik alanın levhalar arasındaki mesafeye bağlı olup olmadığı, oluşan kıvılcımlar yüzünden levhalarda oluşan hasarın ne ölçüde düzeltilebileceği gibi kritik sorulara cevap verilmesi gerekmektedir. Tezin ikinci kısmında bu sorulara cevap aramak üzere metal levhalarda yüksek gerilim testleri yapılmıştır.

Kıvılcım mekanizması tam olarak anlaşılamasa da katot yüzeyindeki elektronların kuantum tünelleme yoluyla vakuma sızması (karanlık akım) ve bunun sonucunda levhalar arasında bir plazma oluşmasıyla başladığı bilinmektedir. Bu plazma ortamı belli bir yoğunluğa ulaştıktan sonra bir boşalma (breakdown) meydana gelir ve kıvılcım ortaya çıkar. Bu kıvılcımlar bazen μA seviyesine ulaşır. Mekanizması tam olarak bilinmediğinden kıvılcımların ne zaman oluşacağı önceden öngörülemez. Bu; levhalar arasındaki mesafe, lavhaların malzeme yapısı, nasıl işlendiği gibi birçok faktöre bağlıdır.

Levhaların işlenmesi, üzerlerindeki pürüzlerin giderilmesi ve malzemenin yüzeyindeki iş fonksiyonunun artırılması maksadıyla yapılmaktadır ve çeşitli süreçler içerir. Bunun için levhalar ilk önce cilalanır. Daha sonra iyon yerleştirme ya da yüksek basınçlı suda yıkama gibi yöntemlerle işlenir. Ardından vakum ortamında son işlemelere tabi tutulur ve artık havayla temas ettirilmez. Bu son işlemeler akımla işleme, kıvılcımla işleme, gazla işleme gibi çeşitli şekillerde olabilir.

Levha yüzeyinin işlenmişliği β ve A_e şeklinde iki parametre ile ifade edilir. Bu parametreler 1928 yılında Fowler ve Nordheim tarafından “karanlık akım” formüle edildiğinde ortaya konmuştur. β, elektrik alan yükseltme faktörü olarak adlandırılır ve levhanın belli bir noktasındaki (pürüzdeki) elektrik alanın ortalama elektrik alandan kaç kat fazla olduğunu gösterir. A_e ise bu pürüzün alanını ifade eder.

Bu çalışmada önceden cilalanmış ve yüksek basınçlı suyla yıkanmış olan levhalar kısa mesafede akım işlemesine tabi tutulmuşlardır. İşlemeden önce levhalar 1 mm mesafede 6 nA karanlık akımla 8 MV/m elektrik alan taşıyabilirken, işlemeden sonra bu alan 74 nA karanlık akımla 48 MV/m’ye yükseldiği gözlenmiştir. Aynı A_e değerine karşılık gelen β parametresinin de yaklaşık olarak başlangıçtakinin %20’sine düştüğü görülmüştür.

1. INTRODUCTION

The Standard Model [1] (SM) is a very successful theory explaining most of the experimental results in particle physics. All the current measurements are consistent with the SM predictions. However, there are severe internal inconsistencies, like the stability of the masses of the W and Z bosons, the carriers of the weak interactions, hinting to physics beyond the SM. One of the major inadequacies of the SM is the observed asymmetry of the matter and antimatter in our universe. This gap was filled by a number of extensions to SM, like Supersymmetry (SUSY).

Most of the current experiments in particle physics aim to probe these extensions to SM. Search for permanent electric dipole moment (EDM) of fundamental particles is one of such experiments.

The SM predicts CP violation through the CKM mechanism, which defines the mixing of three generations of quarks: down, strange and bottom. Here, the CP violation comes from a single phase factor in CKM matrix. This mechanism gives very small values to the EDM of fundamental particles. On the other hand, extensions to SM like SUSY, two Higgs doublet model, Left-Right supersymmetric model etc. predict much higher values, near current experimental limits. This makes the experiments on EDM searches particularly important, since a possible non-zero EDM measurement may mean a new source of CP violation, hence new physics.

This thesis concerns the EDM experiment in storage ring, proposed by the proton EDM (pEDM) collaboration at Brookhaven National Laboratory [2]. The experiment will utilize "frozen spin" method. In this method, the protons will be injected with their spins polarized in the momentum direction, and the polarization will not be lost as long as the proton has some specific momentum value, called "magic momentum".

For an EDM experiment in a storage ring, there are several critical questions to be answered. For instance, how long a beam can be fitted to the ring? While the number of particles improves the statistics, the acceptance should be sufficient for the beam injection.

Another critical question is about the spin coherence time (SCT) of the proton beam in the ring. Since the EDM will be estimated by spin measurements, effects of the systematic errors on the spin precession should be less than the effect of the EDM. In other words, without the EDM effect being taken into account, the spin should remain polarized to some level during storage. SCT is the time over which the spin polarization is lost. In the pEDM experiment, this should be about 1000s. SCT is a critical question, because there is no agreement on how to determine it analytically for an all-electric ring.

Estimations show that SCT is affected by several parameters of the ring such as the length of the straight sections, electric field index, fringe field and so on.

In the first part of the thesis, an all-electric storage ring has been simulated to determine the SCT and the acceptance. Using the hard-edge approximation for fringe fields, the effect of the length of the straight sections and field index are studied. Besides, some differences from magnetic ring are specified. For example, the SCT of the beam is found to be an order of magnitude more than what naive estimations give. Because, the velocity of the particle and the electric field that it sees change continuously as it makes oscillations in the ring. To our knowledge, this effect is first mentioned in this study.

The proposed pEDM experiment requires 10.5MV/m at 3cm gap of parallel plates for a ring with 40m of radius. The second part of the thesis concerns some critical questions about the electric field between the parallel plates. One question is if this electric field can be achieved at 3cm, and does the maximum electric field depend on gap? If a spark occurs, can the plates be recovered?

The second part of the thesis deals with electric field issues mentioned above. It is based on current conditioning of the plates at small gaps. It is seen that the conditioning at small gaps is an effective method, because it produces less energetic sparks, hence less damage during conditioning.

The outline of the thesis as follows:

Chapter 2 gives an overview of the basic concepts related to the EDM, such as discrete symmetries. Then, it focuses on CP-violation and gives the relationship between CP violation and EDM.

Chapter 3 gives the basics of EDM experiments. It overviews the critical concepts like Ramsey's resonance method and the Shielding problem. Then, it explains the Storage Ring Method and the systematic errors related to it. It also explains the Frozen Spin Method, which refers to the cancelling of the horizontal spin precession, known also as g-2 spin precession.

Chapter 4 outlines some concepts from beam dynamics which will be seen in later chapters. While the vast majority of the beam dynamics in the literature deals with magnetic rings, this chapter shows some differences between magnetic and electric rings.

The explanation of the lattice parameters and the simulation are given in Chapter 5. It starts with an overview of the ring. Then, it gives the differential equations of spin and momentum of the particle. These equations are integrated using 4^{th} order Runge-Kutta method. It also introduces the hard-edge approximation used for modelling fringe fields. Finally, the simulation results are given at the end of this chapter. It studies the effects of the total length of straights sections and field index value along with initial conditions of position and momentum on SCT. It is also shown that the spin coherence time of the beam is long enough to store them for 1000s. Besides, some of the parameters in beam dynamics are shown to have different behaviours in all-electric rings and all-magnetic rings.

Chapter 6 firstly introduces the basics of HV tests, treatment methods etc. Then, it gives details of the experimental setup and the methods used for HV tests. The test results are presented at the end of this chapter. They show that conditioning the plates at small gaps is quite an effective method to achieve high electric field strengths.

Finally, the conclusions and future plans are given in Chapter 7.

2. MOTIVATION

Discrete symmetries describe non-continuous changes in a physical system. Time, parity and charge are three discrete symmetries which are almost always conserved in SM. Among others, CP (charge-parity) symmetry is particularly important, because some observations (like matter-antimatter asymmetry) and some models beyond SM (like SUSY) require higher CP-violation sources than SM predictions.

EDMs of fundamental particles are CP-violating physical quantities. Therefore, EDM experiments are critical due to their potential of finding physics not contained in SM.

This chapter firstly introduces discrete symmetries, and CP-violation. Then, it explains the relationship between EDM and CP-violation, reviewing the experimental and theoretical limits of EDMs of fundamental particles.

2.1 Discrete Symmetries

Transformations of physical observables under certain rules have corresponding symmetries. Three discrete symmetries play an important role in the standard model: Parity (P), time (T) and charge (C).

P symmetry corresponds to reversing the signs of the space coordinates of the particles. Polar vectors change sign under parity transformation (e.g. velocity ($\vec{v} = d\vec{r}/dt$) and momentum ($\vec{p} = m\vec{v}$)). Axial vectors like $\vec{J} = \vec{r} \times \vec{p}$ do not change sign under parity transformation.

If the sign of the time coordinate is reversed (T symmetry), some physical quantities like position vector and E-field do not change sign, while some others, those involving time, momentum and B-field do change their sign (See Figure 2.1).

Charge symmetry is a concept from relativistic quantum mechanics and does not have a definition in classical or non-relativistic quantum mechanics. According to this symmetry, every particle has a corresponding anti-particle, which has the same mass, but opposite charge.

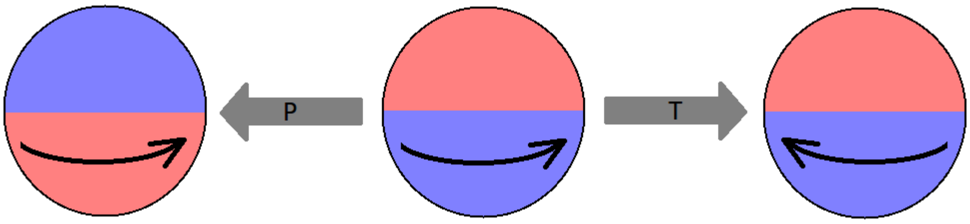

Figure 2.1: Representation of symmetry violation. The direction of arrow after T transformation shows T-violation and the exchange of colors pink and blue after P transformation shows P-violation.

There is a strong confidence that combination of these three symmetries (CPT) is not violated in any interactions. There are some theories that include a violation of CPT but so far there is no experimental evidence of it.

2.1.1 C,P and T violations

After parity violation [3] [4] was observed, theorists assumed that the combination of charge and parity (CP) symmetry is conserved. However, in 1964 it was also observed to be violated in the K_L^0 decays [5], then in B^0 decays in 2001 [6].

This observation was explained through a single CP-violating phase in the CKM matrix, part of the weak interactions theory [7].

2.1.2 Other CP violation sources

It is known that the universe almost entirely consists of matter. The general acceptance is that, there was a symmetry in baryon and anti-baryon number at the beginning of the universe. Sakharov proposed three conditions for the currently observed asymmetry to take place: CP-violation, Baryon number and C-symmetry violation, and the existence of a non-equilibrium phase after the Big Bang [8]. The known weak interaction CP violation is not sufficient for the observed matter-antimatter asymmetry. Therefore some stronger CP violation source is needed.

Secondly, some extensions to SM like SUSY, Left-right supersymmetric model [9], Weinberg multi-Higgs model [10], two Higgs doublet model [11] etc. can provide stronger CP violation sources than predicted by SM (See [12] for more detail).

2.2 Electric Dipole Moment (EDM)

EDM was first mentioned by Dirac [13]. It is defined as:

$$\vec{d} = \int \rho(\vec{x})\vec{x}d^3x \qquad \mathbf{2.1}$$

with ρ the charge density and $\vec{x}$ the position vector in the volume. For neutral particle with equal separated charges, the EDM is defined as the value of the charge times their distance.

For a non-relativistic elementary particle, the dependence of the Hamiltonian on electric $\vec{E}$ and magnetic $\vec{B}$ fields is as follows:

$$H = -\left(\vec{d} \cdot \vec{E} + \vec{\mu} \cdot \vec{B}\right) \qquad \mathbf{2.2}$$

where $\vec{d} = \eta \frac{e}{2m}\vec{s}$ and $\vec{\mu} = g\frac{e}{2mc}\vec{s}$ are electric dipole moment (EDM) and magnetic dipole moment (MDM) respectively. Both $\vec{\mu}$ and $\vec{d}$ are aligned with the spin direction.

Considering only the E-field dependence in Equation 2.2 , the same Hamiltonian is written as:

$$H = -d\vec{E} \cdot \frac{\vec{s}}{|\vec{s}|} \qquad \mathbf{2.3}$$

Since $\vec{E}$ is a polar vector and $\vec{s}$ is an axial vector, the Hamiltonian is odd under both P and T transformations. Therefore, a non-zero EDM means P and T (also CP, assuming CPT invariance) violations at the same time.

With the currently known CP violation sources, SM suggests the EDMs of elementary particles to be much less than the current experimental limits.

First experiment on EDM search was done by Ramsey and Purcell in 1950. The experiment aimed to search for the neutron EDM [14]. Then, the sensitivity of 10^{-20}e·cm was achieved [15].

Since then, EDM experiments showed significant improvement over each decade. Searches of EDM in atomic systems started in 60s. Then, storage ring method was first used in 70s. Molecular systems were studied in 80s and the experiments using molecules started in 90s.

Table 2.1: EDM values of some particles predicted by Standard Model and the present experimental limits.

Particle	EDM [e·cm] (exp.)	Reference
e^-	$< 1.6 \times 10^{-27}$	[17]
p, n	$< 2.9 \times 10^{-26}$	[18]
^{199}Hg	$< 3.1 \times 10^{-29}$	[19]

Table 2.1 gives the experimental limits of the EDMs of some particles. Standard Model predicts much smaller values than these, such as at the level 10^{-36} e·cm for electron and 10^{-32} e·cm for neutron [16]. The difference between the SM predictions and the experimental limits is several orders of magnitude. However, the above mentioned extensions to the SM predict EDM values very close to the current experimental limits.

Currently, the EDM experiments are divided into 3 groups:

- Neutron EDM.
- Permanent EDM in atoms or molecules
- EDM of charged particles

EDM of charged particles requires polarized particles to be trapped in a storage ring. In the storage ring proton EDM experiment proposed at Brookhaven National Laboratory, the EDM of proton is going to be searched with a sensitivity of 10^{-29} e·cm.

2.2.1 EDM contributions from QCD and SUSY

The QCD Lagrangian has a CP-violating term:

$$\mathscr{L}^{\theta}_{QCD} = \theta \frac{{g_s}^2}{32\pi^2} G_{\mu\nu} \tilde{G}^{\mu\nu} \qquad \textbf{2.4}$$

where, g_s is the coupling constant and the gluonic field strength tensor $G_{\mu\nu}$ is defined as $G_{\mu\nu} = [\partial_\mu + ig_s A_\mu, \partial_\nu + ig_s A_\nu]$ in terms of gluon field A_μ and $\tilde{G}_{\mu\nu} = \varepsilon_{\mu\nu\alpha\beta} G^{\alpha\beta}/2$.

This term violates both P and T symmetries (and CP, assuming CPT invariance). However, the parameter θ is known to be very small, rather than being of order one. This peculiarity is known as the “strong CP problem”.

Another parameter $\tilde{\theta}$ is obtained after including weak interactions and performing chiral transformation on θ [20] , and it is related to proton and neutron EDMs as [21]

$$d_n \approx -d_p \approx 3.6 \times 10^{-16} \tilde{\theta} e \cdot cm \qquad \textbf{2.5}$$

Then, neutron EDM of $|d_n| < 3 \times 10^{-26}$ e·cm as shown in Table 1 makes $\tilde{\theta} < 10^{-10}$. The current experimental limit of $\tilde{\theta}$ is the one that pEDM experiment proposes.

On the other hand, SUSY predicts several contributions to quark EDMs and quark color EDMs for neutron and proton [22], [23] :

$$d_n \simeq 1.4(d_d - 0.25 d_u) + 0.83e(d_u^c + d_d^c) - 0.27e(d_u^c - d_d^c) \qquad \textbf{2.6}$$

$$d_p \simeq 1.4(d_d - 0.25 d_u) + 0.83e(d_u^c + d_d^c) + 0.27e(d_u^c - d_d^c) \qquad \textbf{2.7}$$

where, d_q are the quark EDMs, d_q^c are the quark color EDMs and u and d denote the “up” and “down” quarks. It follows that, measurement of a non-zero neutron EDM requires also a non-zero proton EDM to be measured at the same order of magnitude, if Equation 2.5 holds. However, their values may be quite different if Equations 2.6 and 2.7 hold. That is, EDM values originating from $\tilde{\theta}$ and SUSY could differ by a few orders of magnitude. Therefore, the possible neutron and proton EDM measurements together will determine the source of CP-violation.

To sum up, there are three major sources that can give rise to hadronic EDM: Quark electromagnetic EDM, chromo EDM and the CP-violating $\tilde{\theta}$ parameter of QCD. While the first two comes from models beyond SM, the third one comes from the strong interactions in SM.

3. EDM EXPERIMENTS

EDM experiments of fundamental particles are done either by probing the EDM of the particle itself (as in the neutron case), or making the experiment on the atoms, and then extracting the EDM values of the constituent fundamental particles (as in the electron case). In these experiments, the particles are kept under a high electric field for a while, and the coupling of EDM with this electric field changes the orientation of the spins of the particles. This change in the spin direction is a measure of EDM.

Measuring the EDMs of charged particles are particularly difficult, since the electric field moves the particles away very quickly. Therefore, the EDM limits of electron and proton are mostly based on the experiments done with certain atoms like thallium and mercury. Another way of measuring EDM of a charged particle is using storage rings. Within a storage ring, the charged particles make revolutions for a certain storage time under a high electric field. The particles are slowly extracted from the ring in each revolution. Then, their spins are measured. The change of spin direction gives the EDM measurement.

In every EDM experiment, the largest systematic error is the magnetic field. Because it has a very strong coupling with MDM (magnetic dipole moment); even a very small magnetic field (about $10^{-17}T$) dominates the effect of EDM coupling. Therefore, each EDM experiment should have a method to eliminate the effect of the magnetic field.

This chapter overviews the experimental methods in EDM measurements. After giving brief information on neutron and atomic EDM measurements, it focuses on storage rings. After it introduces frozen spin method, magic momentum and polarimeters, it discusses typical systematic errors in a storage ring.

3.1 Experimental Methods

A typical EDM experiment is done in three steps:

1. Polarization of the beam.

2. Electric field is applied to the particles for a time determined by the spin coherence time (SCT). Therefore, the higher the electric field and the SCT, the better the statistical sensitivity of the experiment.
3. Effect of the E-field on spin evolution is measured.

Experimental searches of EDMs include studies of nucleons and leptons. For the search of electron EDM, paramagnetic or diamagnetic atoms are used.

3.1.1 Ramsey's resonance method

If a spin 1/2 particle with magnetic moment μ is placed in a magnetic field $\vec{H}_0$, its spin precesses around the $\vec{H}_0$ direction with Larmor frequency $\vec{\omega}_0$ as shown in Fig 3.1 according to:

$$\omega_0 = 2\pi\nu_0 = \frac{2\mu H_0}{\hbar} \qquad \textbf{3.1}$$

Placing a rotating magnetic field $\vec{H}_1$ around $\vec{H}_0$ causes the spin precess also around the perpendicular direction to $\vec{H}_0$. Then, the value of ϕ oscillates. If $\vec{H}_1$ rotates with frequency ω_0, then the spin precesses both around $\vec{H}_0$ and the perpendicular axis. This can easily be seen from the spin rest frame. This specific configuration causes the angle ϕ to oscillate with the maximum possible angle over time.

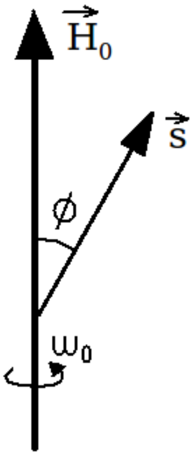

Figure 3.1: Spin precession around a magnetic field $\vec{H}_0$.

Figure 3.2 shows a typical dependence of ϕ on ω, frequency of rotation of $\vec{H}_1$ in a neutron experiment. The ϕ angle maximizes at Larmor frequency. Therefore, this method is used to measure the Larmor frequency of a precessing spin 1/2 particle.

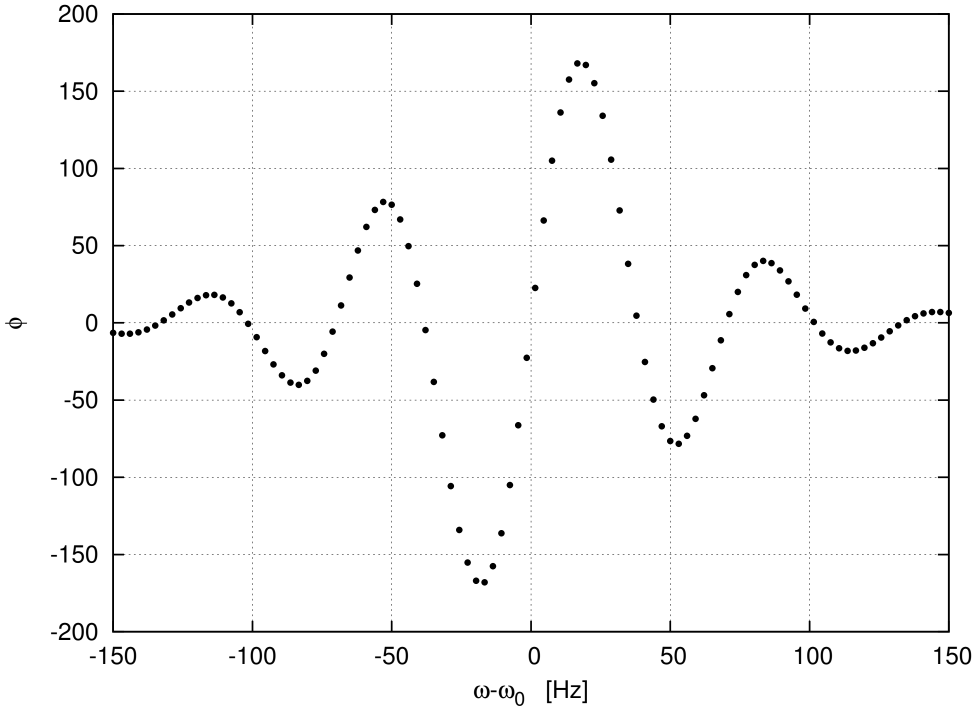

Figure 3.2: A typical resonance curve. Resonance of the neutron is defined by the distribution of the ϕ angle over an experiment for various ω rotation frequency values of $\vec{H}_0$. The highest ϕ value is obtained when $\omega = \omega_0$, the Larmor frequency.

Ramsey's resonance method makes a slight improvement over the resonance method mentioned above. The change is about the application of $\vec{H}_1$. Rather than being applied continuously, $\vec{H}_1$ is applied twice for a short time of τ (See Figure 3.3). Within time T between these two applications, only $\vec{H}_0$ is applied on the spin. So the particle experiences the constant $\vec{H}_0$ and oscillating $\vec{H}_1$ for τ seconds, then only $\vec{H}_0$ for T seconds, and finally again constant $\vec{H}_0$ and oscillating $\vec{H}_1$ for τ seconds. This way, the problem with the initial angle $\phi = 0$ is avoided, because $\vec{H}_1$ makes the spin gain some angle ϕ at the beginning of the process (See [24] for more detail).

3.1.2 The shielding problem

If an electric field is applied on a neutral atom or molecule of point particles which interact through electrostatic forces, the charge reconfiguration of that atom/molecule shields the E-field. Therefore, neutral atoms and molecules were considered to be useless for EDM searches.

Schiff theorem [25] shows that there are loopholes in this shielding problem (See also [26]):

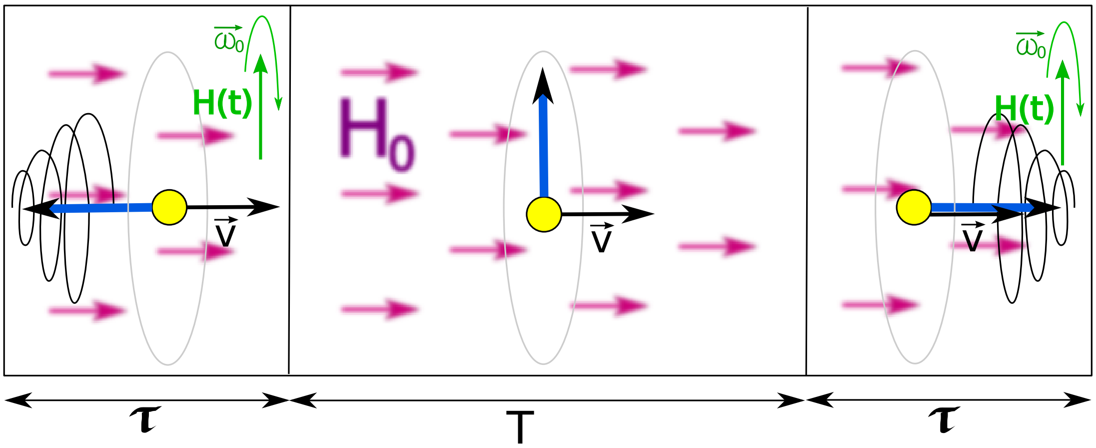

Figure 3.3: The particle runs through three regions. In all of the regions there is a constant $\vec{H}_0$ in the direction of the motion. In the first and the third regions it also has $\vec{H}_1$, rotating at Larmor frequency. After passing the first region, the spin of the particle rotates by $\pi/2$. Then, it just makes Larmor precession in the second region. In the third region, its spin rotates another $\pi/2$, provided that it has the same length with the first region. T should be much longer than τ.

- Finite size: If the finite size of the atomic nucleus is taken into account, the dipole moment inside it turns out to be somewhat unshielded. This effect is parametrized by the Schiff moment, which is the misalignment between charge distribution and the EDM of the nucleus. Generally the heavier the nuclei, the bigger the Schiff moment is.

  It has been estimated that in certain atoms, the cancellation of atomic EDM due to the Schiff moment can be minimized. This least cancellation leads a small residual EDM to remain. This effect is biggest in heavy diamagnetic atoms. As an example, for ^{225}Ra, the effect can further be enhanced due to its octupole-deformed nuclei [27].

  So far, the most precise EDM measurement for diamagnetic atoms was made for ^{199}Hg, but the physics sensitivity is reduced by a factor of 1000 due to Schiff moment.

- Relativistic effects: In paramagnetic atoms, relativistic effects can cause the EDM of the valance electron to induce an atomic EDM. This enhancement ($R = d_a/d_e$) is proportional to approximately $10Z^3\alpha^2$, where Z is the atomic number and α is the structure constant [28]. For heavy atoms, this causes a big amplification of the electron EDM. For example thallium atom, with $Z = 81$, has an enhancement factor of R=-585 [29].

There are a variety of systems to measure electron EDM, including YbF [30] and PbO [31] molecules.

It is worth noting that one can also set limit to the proton EDM, once the molecular EDM is measured making use of the Schiff theorem (See [32] for more detail).

3.1.3 Neutron EDM

Because of the difficulties of storing a charged particle and the shielding problem, neutron is the first particle used for EDM search. The first experiment was done by Smith, Purcell and Ramsey in Oak Ridge reactor in 1949 [14].

The experiments on neutron EDM are based on measuring the change of Larmor precession frequency of the neutron beams for different E-field orientations (parallel and anti-parallel to B-field), which undergo a resonance as explained above.

In a neutron experiment, the neutrons are first polarized by scattering them off a thin magnetized ferromagnetic film. Zeeman interaction between those two defines a critical angle for the neutron. This causes the neutrons with certain spin states be transmitted and the others reflected when sent below that critical angle to the film.

The second step of the experiment includes the interaction with E-field. The Hamiltonian of the particle is defined as in Equation 2.2. If the polarized neutron beam is placed in a region to resonate as in Ramsey's resonance method with collinear constant electric and magnetic fields $\vec{E}_0$ and $\vec{B}_0$ respectively, the Larmor frequency of the spin precession is

$$\omega_0 = \frac{2\mu B_0 \pm 2dE_0}{\hbar} \qquad \textbf{3.2}$$

where μ and d are the magnetic and electric dipole moments respectively. Here, $\pm$ sign shows if E_0 is parallel or anti-parallel to B_0. This means, inverting the direction of E_0 gives two different Larmor frequencies if d is non-zero. The difference is:

$$\Delta\omega = \frac{4dE}{\hbar} \qquad \textbf{3.3}$$

Finally, the average polarization of the neutron beam is measured using the same technique as in the first step: The neutrons are reflected or transmitted off the ferromagnetic film. Then the number of neutrons reflected and transmitted are compared to get the intensity of the neutrons and to calculate the EDM:

$$d = \frac{\hbar}{4}\left(\frac{\Delta N}{E}\frac{dN}{d\omega}\right) \qquad \textbf{3.4}$$

The neutron beams used in the above experiment have about 0.4 eV of kinetic energy. The experiments using ultra-cold neutrons (UCN) have a typical energy of 100 meV or less [33]. This lower energy prolongs spin coherence time of the particles, hence better statistical sensitivity.

3.1.4 Storage ring method

The above mentioned neutron EDM experiments, where a large electric field is applied to the neutrons, cannot be applied to charged particles. The particle would move and will be lost in a very short time. However, if the charged particles are stored in a ring, then the centrifugal force balances the radial electric field (See [34] and [35] for muon EDM search). The velocity of the particle changes under electric and magnetic field as follows:

$$\frac{d\vec{\beta}}{dt} = \frac{e}{\gamma m}\left[\frac{\vec{E}}{c} + \vec{\beta}\times\vec{B} - \vec{\beta}\frac{(\vec{\beta}\cdot\vec{E})}{c}\right] \qquad \textbf{3.5}$$

where β, e and m are the particle speed over speed of light, charge and mass of the particle respectively, $\gamma = (1-\beta^2)^{1/2}$, and c is the speed of light.

The E-field coupling with the EDM of the particle can precess its spin in the vertical direction. The spin precession of a relativistic particle under $\vec{E}$ and $\vec{B}$ fields is given by T-BMT equation with the dipole moment term [36]:

$$\begin{aligned}\frac{d\vec{s}}{dt} = \frac{e}{m}\vec{s}\times\Bigg[&\left(\frac{g}{2}-\frac{1-\gamma}{\gamma}\right)\vec{B} - \left(\frac{g}{2}-1\right)\frac{\gamma}{\gamma+1}\left(\vec{\beta}\cdot\vec{B}\right)\vec{\beta} - \\ &\left(\frac{g}{2}-\frac{\gamma}{\gamma+1}\right)\frac{\vec{\beta}\times\vec{E}}{c} + \frac{\eta}{2}\left(\vec{\beta}\times\vec{B} + \frac{\vec{E}}{c} - \frac{\gamma}{\gamma+1}\frac{\vec{\beta}\cdot E}{c}\right)\Bigg]\end{aligned} \qquad \textbf{3.6}$$

where and g is the g-factor. The last term is the EDM term, with the dimensionless parameter η, playing the same role with g-factor of magnetic dipole moment. In this study, η is set to zero, so that it will not be included in the calculations.

For a particle at rest, the spin precession due to EDM and MDM is given by:

$$\frac{d\vec{s}}{dt} = \vec{d}\times\vec{E} + \vec{\mu}\times\vec{B} \qquad \textbf{3.7}$$

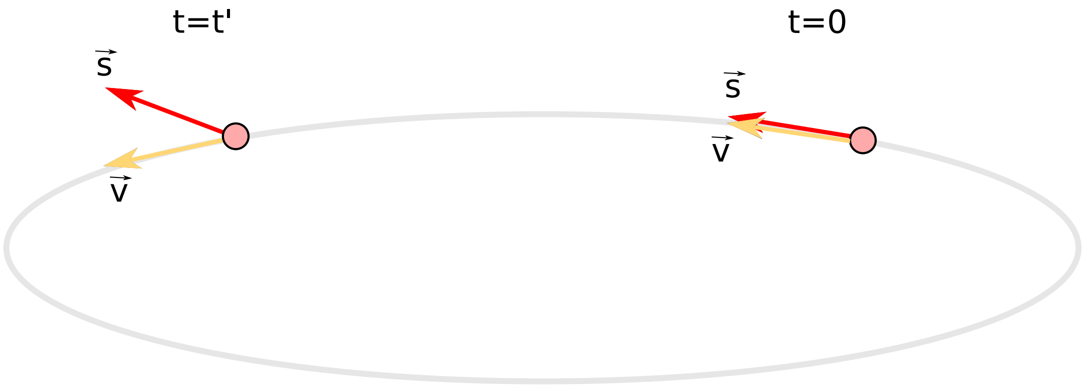

Figure 3.4: The injected particle is initially polarized. However, if it is off-magic momentum, the angle between its spin and momentum increases over time, while circulating around the ring under electric field. This is called spin decoherence.

For a moving particle the Thomas precession (the fact that the particle is in an accelerated frame) needs to be taken onto account. When $\vec{B} = 0$ the rate of change of the angle between the spin and momentum vectors is given by [37]:

$$\vec{\omega}_a = \frac{e}{m}\left[\frac{1}{\gamma^2 - 1} - a\right]\frac{\vec{\beta} \times \vec{E}}{c} \qquad \textbf{3.8}$$

where a is the anomalous magnetic moment. As seen in Eq 3.8, a special value of $\gamma = \sqrt{\frac{1}{a} + 1}$ locks the angle between spin and momentum to the initial value. The method making use of this property is called “frozen spin method” [38]. By the definition of the relativistic momentum, $\vec{p} = \vec{\beta}\gamma mc$, a specific momentum of $p_0 = m/\sqrt{a}$ is called “magic momentum”. For a proton, $p_0 = 0.7007$ GeV/c. For any particle with $a > 0$, there is such a unique momentum which freezes the angle between momentum and spin in electric field regions. For magnetic fields this happens only when the particle g-factor is equal to 2.

If the particle moves at magic momentum, the spin will be frozen. Otherwise, spin starts precessing and after a while, the angle between spin and momentum increases (See Figure 3.4). This effect (also called spin decoherence) spoils the EDM signal. Therefore, it should be minimized in an EDM experiment.

Once it becomes negligible, the only factor that affects the spin precession is EDM:

$$\frac{d\vec{s}}{dt} = \vec{d} \times \vec{E} \qquad \textbf{3.9}$$

(In the vertical direction there is no acceleration and therefore there is no Thomas precession. Hence the spin precession rate is given by the simple equation 3.9). So, for a particle running in an all-electric ring (i.e. $\vec{B} = 0$) at the magic momentum, measurement of a spin precession in the vertical direction is evidence of non-zero EDM. Because, the only term causing this precession is due to the coupling between $\vec{d}$ and $\vec{E}$.

In the experiment, the measurements will start with the spin of the protons polarized in the direction of the momentum. Then, the coupling between the E-field and the EDM moves the spin vertically. During 1000s, the particles will rotate around the ring and some of them will be scattered off the polarimeter target. At the end of the run, all the particles will hit the target to give the change of spin direction over time.

3.1.5 Polarimeter

The small changes in the vertical component of the beam polarization will be measured using a polarimeter. The particles are scattered off a suitable target under certain conditions for the measurement. In pEDM experiment, this is planned to be done via forward-angle elastic scattering from carbon nuclei.

The thickness of the target is planned to be about 6 cm. Before reaching the target, the size of the beam in the vertical phase space will be increased so that the particles at the edge of the beam will intercept the target. This will be done by changing the vertical tune. Then the scattered particles hit the detector to give the polarization, using the signal counts on the up-down and left-right detectors. The scattering angle will be between 5^o and 20^o. (See Figure 3.5).

The particles farther away from the magic momentum will be lost from the beam first, since they will be the ones on the edge to hit the target. This feature will increase the spin coherence time. Then, the whole beam will be extracted in 1000 seconds.

Between the target and the detector is placed an absorber, which will remove inelastic and high Q-value events, so that the particles hitting the detector will be the ones with higher polarization dependence.

The candidate detector types to be used are multi-resistive plate chambers, micro-megas chambers and gas electron multiplier chambers, due to minimum dead time and small systematic errors.

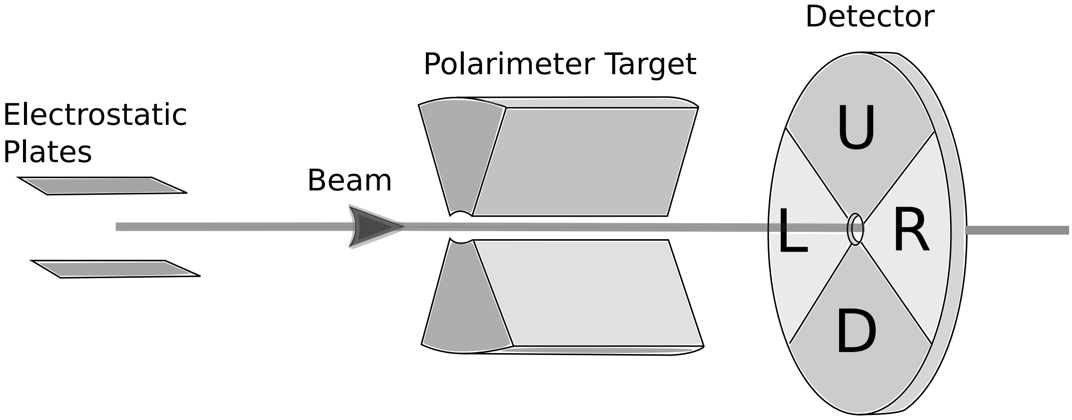

Figure 3.5: Main elements of the pEDM polarimeter. The beam first passes through the electrostatic plate to have a bigger size in vertical phase space. Then the particle hits and penetrates through the polarimeter target and gets scattered into the detector.

The vector polarization is defined as $p_v = f_+ - f_-$, the difference between the fractions of up and down polarized particles in the beam. Cross ratio formulation gives the polarization as $p = \varepsilon/A$, with

$$\varepsilon = \frac{r-1}{r+1} \tag{3.10}$$

$$r^2 = \frac{C_L(+)C_R(-)}{C_L(-)C_R(+)} \tag{3.11}$$

where the $C_S(\pm)$ are the count rates for the normal (+) and reversed (-) polarizations and the events detected to the left and right of the beam when the vertical polarization is measured, and A is the effective analysing power. While most of the linear effects of the geometric and rate systematic errors are eliminated by this formula, second-order effects such as the ones related to beam drifting will be eliminated after corrections to the polarization.

3.1.6 Systematic errors

The common systematic error for all EDM experiments is that if there is a magnetic field in the direction of the applied electric field, it couples with MDM and mimics the EDM effect (see Eq 2.2). To avoid this effect, the following condition should be satisfied in the experiment:

$$\vec{d}\cdot\vec{E} > \vec{\mu}\cdot\vec{B} \tag{3.12}$$

where $\mu \approx -8 \times 10^{-8}$ eV/T for proton. For an E-field of 10 MV/m and EDM measurement of 10^{-29} e·cm, the radial magnetic field should be less than 10^{-17} T in order to suppress the MDM effect.

The earth's magnetic field is about 30μT. It cancels out to first order since it has the same direction in the ring. Besides, it is mostly a vertical B-field, not radial. However, this field is going to be reduced by large Helmholtz coils inside the ring tunnel, then shielding system with shielding factor of 10^5 and then a Helmholtz coil inside the beam tube. These three elements will reduce the magnetic field by a factor of $\sim 10^9$.

Besides earth, the city environment is another source of magnetic field. This is generally of the order of several $\mathrm{nT}/\sqrt{Hz}$ for 0.1-1 Hz.

The measurement of radial magnetic field (B_r) requires measurement of the distance between clockwise (CW) and counter-clockwise (CCW) beams using beam position monitors (BPM). In the absence of no radial magnetic field, the distance between the center of mass of the two will be zero, hence no signal on the BPM. In case of radial magnetic field, they split due to the Lorentz force. The distance between them will be proportional to B_r.

The position measurement of a beam using a BPM relies on the asymmetry of the signal generated on it. Some BPMs like stripline BPMs measure the image charges, some others like RF cavity BPMs measure EM field and so on. If the beam passes above the center of the BPM, it induces a bigger signal on the above port and vice versa (See Figure 3.6). For two identical beams moving in opposite directions, the BPM measures the distance between them. There is no signal if they are at the same position. If there is an the induced signal, then it is a measure of the distance between them.

Another possible systematic error for storage rings is about the multipoles of the E-field which is due to the edge effects of the parallel plates. The possible resonances on spin/beam dynamics due to these multipoles are potential cause for instabilities or short spin coherence time.

Wake fields is another potential systematic error for storage rings. The electromagnetic field due to the beam may reflect at some parts of the ring to cause resonances, which may affect both spin and beam dynamics. These effects can be controlled by clever design of the ring. For our ring design, preliminary studies showed that they are below our sensitivity level.

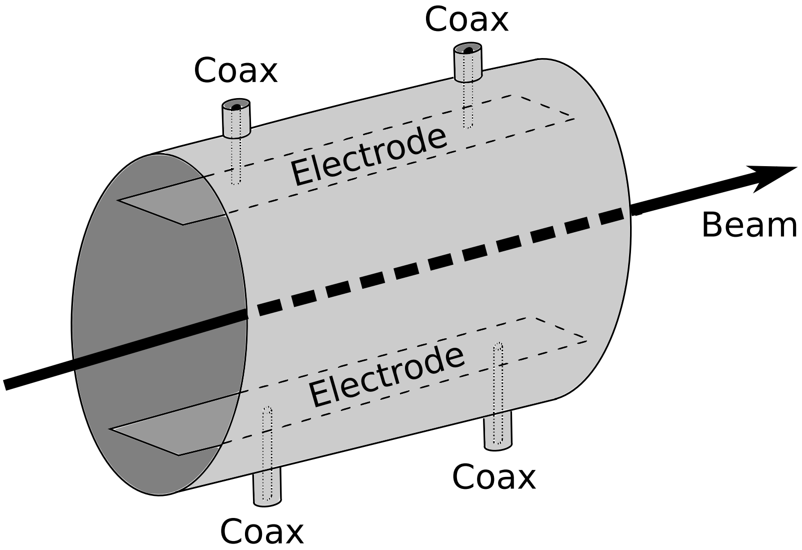

Figure 3.6: Schematic view of a stripline BPM. While the beam passes through, it induces charges on top and bottom electrodes. The signals due to the image charges on top and bottom electrodes are compared to determine tha position of the beam.

4. BEAM DYNAMICS

A beam of particles moves under the Lorentz force in a ring. The general equations of motion of the beam originate from relativistic Hamiltonian mechanics and the solutions are basically oscillations about the design orbit. Some of these parameters describing this motion may not be well applicable to both magnetic and electric rings (See [39] and [40] for some analytical calculations on electric rings).

The motion of a particle in an electric field differs radically from the magnetic field, because the electric field changes the kinetic energy of the particle. Since the electric field in a ring depends on the position of the particle, the beam behaves in a much different way in electric rings. This effect is more visible in radial motion than vertical. Therefore, the vertical motion of the particle in an electric ring is closer to the magnetic ring than radial motion.

The difference between the motion of a particle in electric and magnetic fields cause some parameters defined in magnetic rings to show different behaviour in electric rings. While some of them are estimated in analytical calculations, some others can be estimated only numerically.

Despite the title, this chapter does not intend to cover all of the beam dynamics. There are several books to meet the needs of an interested reader in the subject (such as [41] and [42]). This chapter basically introduces some parameters that will be encountered in the later chapters of this thesis.

4.1 Betatron Oscillation

The motion of the particle inside the ring is defined by the electromagnetic field that it sees. For an electric ring, using Maxwell's equations, the electric field in the bending section is approximated as (See Appendix A):

$$E_R = E_0 \left(\frac{R_0}{R}\right)^n \left[1 - \frac{n^2-1}{2}\frac{z^2}{R^2} + \frac{1}{24}(n^2-1)(n+1)(n+3)\frac{z^4}{R^4} + O(z^6)\right] \qquad \textbf{4.1}$$

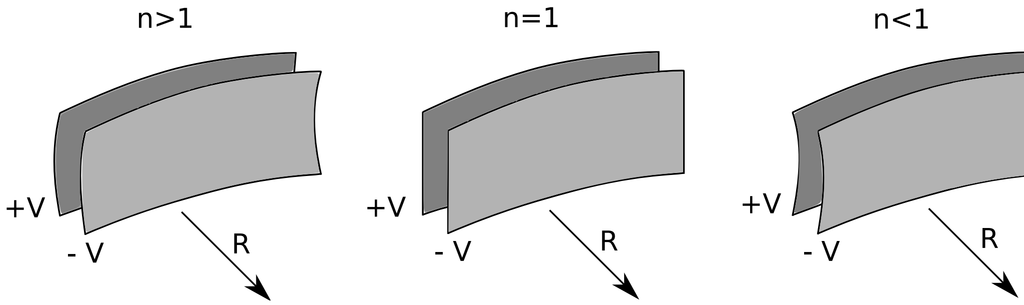

Figure 4.1: Shape of the parallel plates determines the field index (n).

$$E_z = E_0 \left(\frac{R_0}{R}\right)^n \left[(n-1)\frac{z}{R} - \frac{1}{6}(n^2-1)(n+1)\frac{z^3}{R^3} + O(z^5)\right] \qquad \textbf{4.2}$$

where R is the radial position of the particle with respect to the center of the circle with radius R_0, z is the vertical position, E_0 is the electric field at $R = R_0$ and $z = 0$, $n = 1 - m$ where m is the field index. n value is determined by the shape of the E-field plates as shown in Figure 4.1.

In a magnetic ring, when the radial and vertical coordinates of the particle do not change during storage, that particle is called the "ideal particle" and that orbit is called the "design orbit" of the ring. Otherwise it oscillates around the design orbit. Figure 4.2 shows a particle oscillating in both radial (x) and vertical (z) directions around the design orbit. These oscillations are called "betatron oscillations". Vertical betatron oscillation and horizontal betatron oscillation regularly have different frequencies as also seen in the figure. These frequencies are determined by the field index $m = 1 - n$. Unlike magnetic rings, particles in an electric ring may have betatron oscillations around a nonzero value.

4.2 Betatron Tune

Number of oscillations per turn is called tune. For a magnetic ring with a weak focusing field index m, the horizontal and vertical tunes are defined as

$$Q_x = \sqrt{1-m} \qquad \textbf{4.3}$$

$$Q_z = \sqrt{m} \qquad \textbf{4.4}$$

respectively. However, Lorentz factor γ is introduced in electric rings due to the fact that the particle energy is oscillating. For an electric ring with small field index m, the

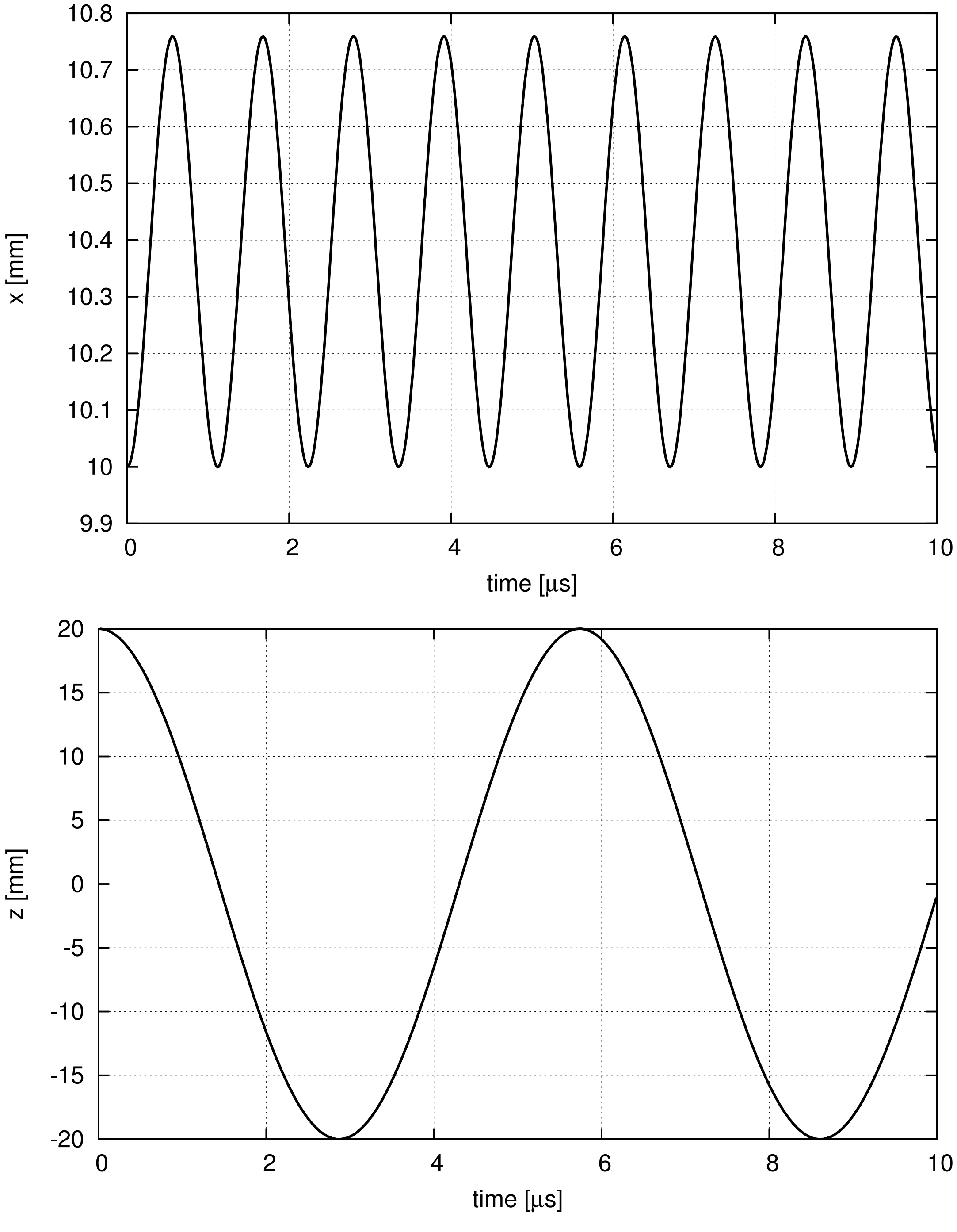

Figure 4.2: The betatron oscillations of the particle in radial (x) and vertical (z) directions are shown in upper and lower figures respectively. The ring has no RF in the ring. The initial radial and vertical positions are 1cm and 2cm respectively. It is seen that the design orbit is at $x \approx 10.4$mm in radial direction and at $z = 0$ in vertical direction. This is where electric ring differs from magnetic ring. In a magnetic ring, the betatron oscillations are always around zero.

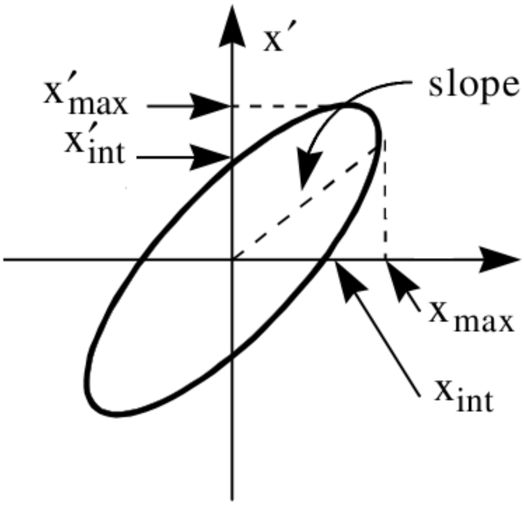

Figure 4.3: Emittance is the area of the ellipse in phase space and it is characterized by the twiss parameters α, β and γ.

horizontal and vertical tunes turn out to be [40]:

$$Q_x = \sqrt{1 + \frac{1}{\gamma^2} - m} \tag{4.5}$$

$$Q_z = \sqrt{m} \tag{4.6}$$

4.3 Emittance

Emittance is the area that the beam occupies in phase space (See Figure 4.3):

$$\varepsilon = \gamma x^2 + 2\alpha x x' + \beta x'^2 \tag{4.7}$$

where $\alpha = -\frac{1}{2}\frac{d\beta(s)}{ds}$ and $\gamma = \frac{1+\alpha^2}{\beta(s)}$. α, β and γ are called “twiss parameters” and they are defined using Figure 4.3 as follows:

$$x_{max} = \sqrt{\beta\varepsilon} \tag{4.8}$$

$$x'_{max} = \sqrt{\gamma\varepsilon} \tag{4.9}$$

$$x_{int} = \sqrt{\varepsilon/\gamma} \tag{4.10}$$

$$x'_{int} = \sqrt{\varepsilon/\beta} \tag{4.11}$$

$$slope = -\alpha/\beta \tag{4.12}$$

Emittance limits the beam properties like size, momentum spread ($\Delta p/p$) and initial angle of the beam to be injected. It’s a parameter of the ring design, not the beam.

The points in the phase space may form a thick line if there are straight sections in the ring (Figure 4.4). The thickness of the line comes from the change of the position of

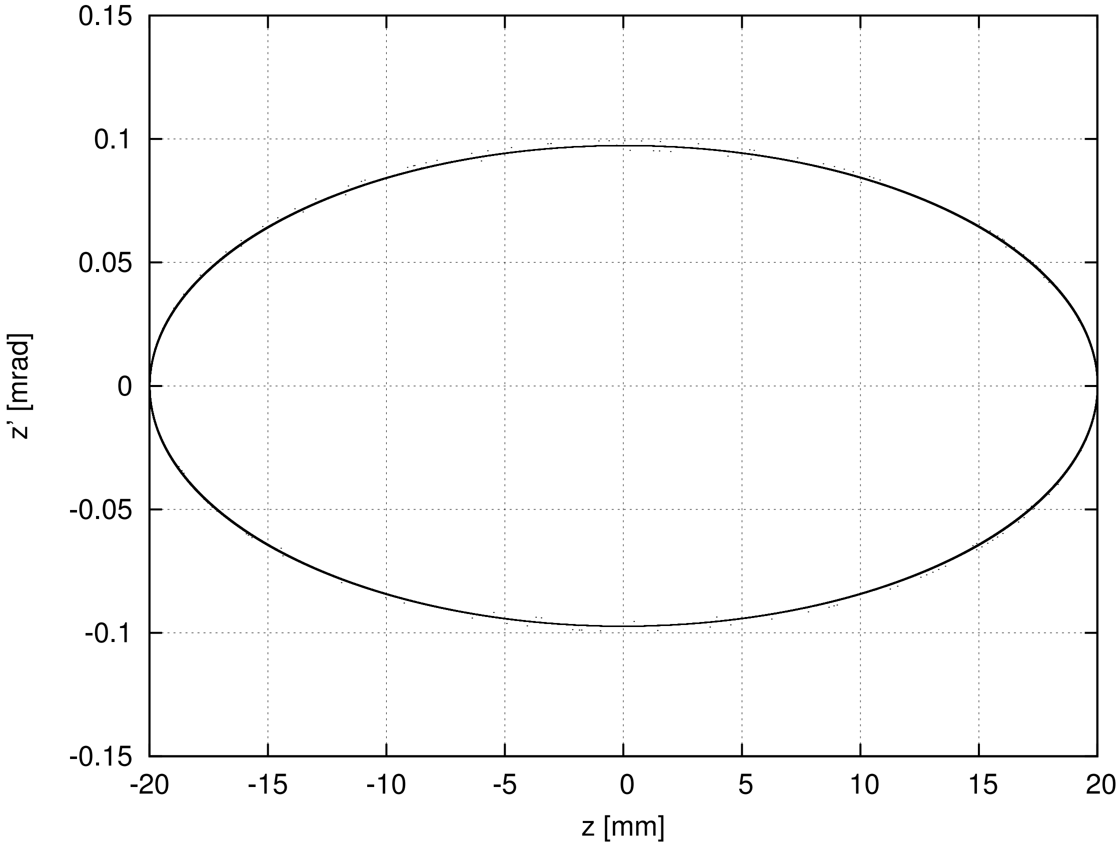

Figure 4.4: $z - z'$ plot for a ring with straight sections. z is the vertical position of the particle and z' is the angle between vertical and longitudinal velocities. The particle starts from $z_0 = 2$cm at magic momentum. In the straight sections no electromagnetic force is applied on the particle. Therefore it makes a motion with constant velocity through the straight sections. This causes its deviation to increase without any change in its velocity after it passes through some of the straight sections. Hence a thick line.

the particle before and after straight sections. Since there is no electromagnetic field in the straight sections, the velocity of the particle does not change after it passes through the straight section, while its position with respect to the ideal orbit may change. More detail is given in Section 5.2.

4.4 Synchrotron Oscillation

Momentum deviations make the particle move faster or slower than the ideal particle. Its momentum can be controlled using kickers such as RF cavity. RF cavity makes the energy of the particle oscillate about the energy of the ideal particle. This oscillation is called "synchrotron oscillation". Figure 4.5 shows an RF cavity. Oscillating potential V_{rf} causes an oscillating E-field in the longitudinal (y) direction, on which the beam travels.

Considering that the V_{rf} potential changes sinusoidally, each time it passes through the cavity, the particle will gain or lose an energy of

$$W = W_0 sin(\omega_{rf} t + \phi) \qquad \textbf{4.13}$$

where ω_{rf} is the angular frequency of revolution of the ideal particle, and ϕ is the phase.

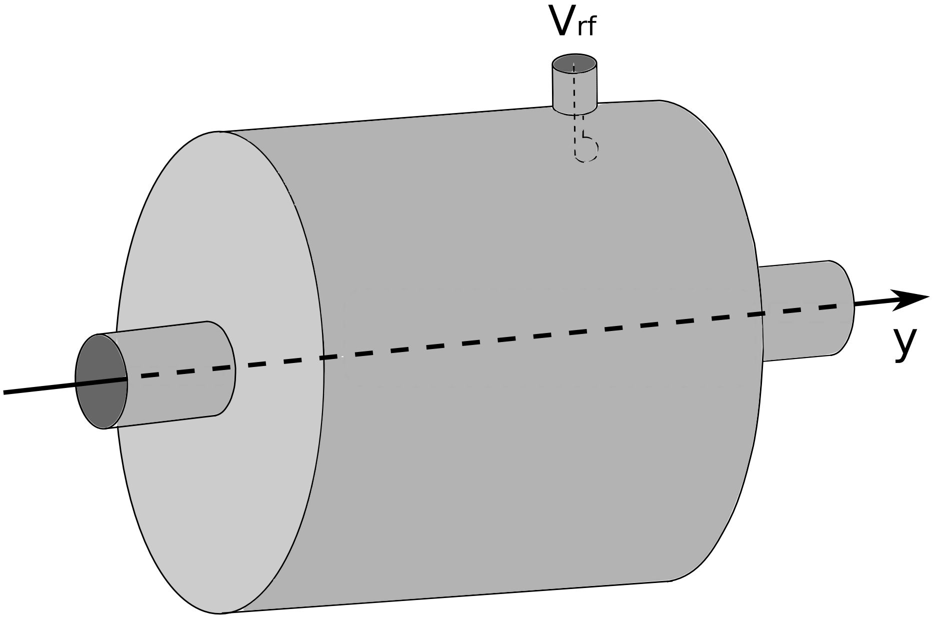

Figure 4.5: RF Cavity generates an oscillating E-field in longitudinal direction (y), along which the particle travels.

RF oscillation frequency is defined as

$$f_{rf} = \sqrt{\frac{2\pi h \eta V_{max} \cos\phi}{E}} f_{rev} \qquad \textbf{4.14}$$

where η is the slip factor to be defined below, h is the harmonic number of the RF cavity, V_{max} is the maximum value applied in the RF cavity, ϕ is the RF-phase and

f_{rev} is the revolution frequency. It is worth noting that the frequency f_{rf} depends on $\sqrt{hV_{max}}$.

4.5 Synchrotron Tune

The number of synchrotron oscillations over one turn is called “synchrotron tune”. Its value is typically much smaller than the betatron tunes.

4.6 Dispersion Function

If the momentum of the particle is different from the ideal momentum, that particle moves on another closed orbit. In magnetic rings, dispersion function relates the radial deviation of the particle to the change in the momentum:

$$x(s) = D\frac{\Delta p}{p} \qquad \textbf{4.15}$$

where x is the horizontal deviation of the particle from the ideal orbit at any longitudinal position s.

However, in this thesis, it’s shown that this relation is much different in electric rings.

4.7 Momentum Compaction

Momentum compaction measures the change of the circumference length of the closed orbit for any change in the momentum:

$$\alpha = \frac{\Delta L/L}{\Delta p/p} \qquad \textbf{4.16}$$

where α is the momentum compaction factor and L is the circumference of the orbit.

4.8 Phase Slip Factor

The phase slip factor η relates the momentum change to the revolution time:

$$\frac{\Delta T}{T} = \eta\frac{\Delta p}{p} \qquad \textbf{4.17}$$

with

$$\eta = \alpha - 1/\gamma^2 \qquad \textbf{4.18}$$

where T is the revolution time, α is the momentum compaction factor and γ is the Lorentz factor.

Using Equations 4.17 and 4.18 "transition energy" is defined as $\gamma_t = \sqrt{1/\alpha}$:

Below this energy ($\eta < 0$), the revolution time of the particle decreases for high-energy particles and increases for low-energy particles. This causes the particle tend to be stable around the ideal momentum with a certain synchrotron oscillation. This can be seen by imagining two particles, one with higher-energy and the other with lower-energy than the ideal particle:

Higher-energy particle moves faster than the ideal particle. According to Equation 4.13, next time it will reach the cavity at an earlier phase. Since ideal particle reaches at phase $\phi = 0$, this high energy particle reaches at a slightly more negative phase. This makes the particle lose some energy.

With the same token, the lower-energy particle reaches the cavity next time at a slightly more positive phase. This makes the particle gain some energy in the cavity.

With this mechanism, the non-ideal particles gain and lose energy within the beam to make synchrotron oscillation.

This property means that the stable RF-phase is 180 degrees apart for particles below and above transition, while the synchrotron oscillations are still stable. It is possible that the particle momentum spread implies an energy spread that is above the maximum energy that can be gained in the RF-cavity per revolution. In that case the particles are not captured by the RF and it jumps from bunch to bunch.

In this thesis, it is shown that unlike magnetic ring, the slip factor has a strong dependence on both momentum spread and radial offset in electric ring.

5. SIMULATION AND LATTICE DESIGN

Strong dependence of kinetic energy on the position of the particles makes analytical solutions extremely difficult. Even 1mm of radial displacement causes a change $\Delta p/p \approx 2.5\times 10^{-5}$ in momentum. Since most of the analytical solutions in accelerator physics rely on the constancy of kinetic energy, they become useless in electric rings. Then, precision tracking turns out to be a good way to study this kind of a system.

The effects of the field index and the total length of straight sections (L_{str}) on SCT are critical issues for a proton beam in a storage ring. L_{str} should be long enough to put several elements like BPMs, quadrupoles etc. in the ring. On the other hand, one should make sure that this length does not cause a decrease in SCT. Therefore, one needs to determine the effect of L_{str} on SCT. Similarly, the experiment requires a small value of field index and it must be optimized for the SCT too. Another critical issue is how much beam can be fitted in the ring, which addresses the admittance.

This chapter starts with the details of the lattice design used in the simulations, including the way the electric field in the bending sections and at the edges are handled. Then, the simulation results are discussed. These include the effect of L_{str} and field index on SCT, admittance calculations and the behaviour of the g-2 spin precession. Among these results, the most important one is the last one, which shows the effect of the $\vec{\beta}\times\vec{E}$ of Equation 3.8.

The simulated ring is composed of 14 bending and straight sections (see Figure 5.1). One of the straight sections includes an RF cavity.

The ring lies on the x-y plane. Then the vertical plane (out of paper) is denoted by z.

The simulations were done with one particle, with some initial offset in position, momentum and angle from the ideal case.

5.1 Bending Section

The particle moves in the bending section of 40m radius, obeying Equations 3.6, 4.1 and 4.2. For some measurement reasons, the vertical tune in the experiment is planned to be $Q_z = 0.2$. From Equation 4.6, this corresponds to $n = 1.04$ for the simulations which don't include separate quadrupoles.

The position and spin of the particle are calculated by integrating the following equations [36] with 4^{th} order Runge-Kutta method (See Appendix B for an overview of the method):

$$\frac{d\vec{\beta}}{dt} = \frac{e}{\gamma mc}\left[\vec{E} + \vec{\beta}(\vec{\beta}\cdot\vec{E})\right] \tag{5.1}$$

$$\frac{d\vec{s}}{dt} = -\frac{e}{mc}\vec{s}\times\left(\frac{g}{2} - \frac{\gamma}{\gamma+1}\right)\vec{\beta}\times\vec{E} \tag{5.2}$$

where e, m and $\vec{s}$ are the charge, mass and the spin of the particle respectively, c is speed of light, $\beta = v/c$, $\gamma = (1-\beta^2)^{-1/2}$, g is the g-factor, $\vec{E}$ is the radial E-field in the lattice. Magnetic field is not included in these equations, since it is going to be shielded in the experiment. Equation 5.2 is the above-mentioned "T-BMT equation".

5.2 Straight Section

Straight sections in a ring include the measurement and alignment devices such as quadrupole, sextupole, BPM, RF cavity. Ideally, these are the only sources of E and B-field in the straight section. In practice, the field in the bending section extends to the straight section, forming a fringe field region. In hard-edge approximation, the fringe field is approximated as a sharp transition from a field region to no-field region. This is done by keeping the total energy conserved in the transition between the bending and the straight sections as shown in Figure 5.2.

The energy conversion at the edges of the straight section is made by changing the magnitude of the longitudinal velocity of the particle, keeping the transverse components of the velocity constant. This is a good approximation, since the longitudinal component of the velocity of the particle is much bigger than the transverse components.

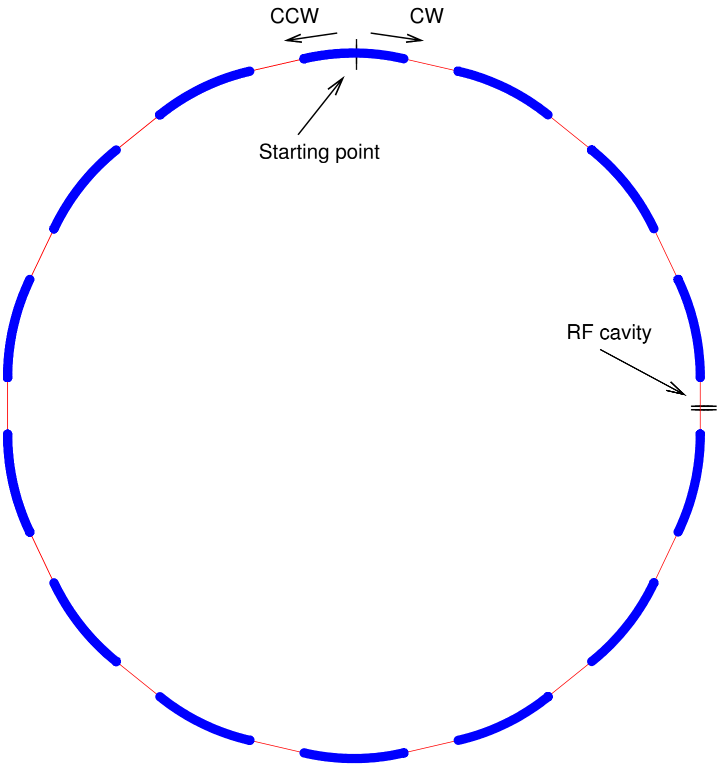

Figure 5.1: The ring includes 14 bending and straight sections, with one RF cavity.

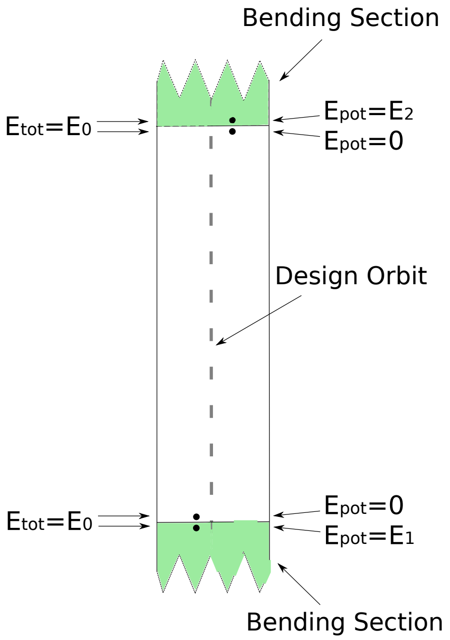

Figure 5.2: At the interface of bending and straight sections, kinetic and potential energy changes are made keeping the total energy conserved. The fringe region is assumed to be hard edged. The black spots represent the points just before and after crossing the boundary.

Since there is no field, the particle moves inside the straight section with no force acting on it. For the straight section with RF-cavity, the energy is changed at the center of it by:

$$\Delta W = qV_0 sin(\omega_{rf}t + \phi) \qquad \textbf{5.3}$$

where V_0 is the maximum voltage in the RF-cavity, ϕ is the synchrotron phase and ω_{rf} is the synchrotron frequency defined as:

$$\omega_{rf} = h\frac{2\pi}{T_{rev}} \qquad \textbf{5.4}$$

with h, the harmonic number and T_{rev}, the revolution time of the ideal particle. In the simulations for a ring with 14m of straight section, the parameters in Equations 5.3 and 5.4 are $V_0 = 10^6$ V, $h = 1$, $T_{rev} \approx 1.48\mu$s and $\omega_{rf} \approx 4.25 \times 10^6$ cycles per second. Note that for a certain synchrotron frequency, V_0 and h are inversely proportional (e.g, $h = 100$ and $V_0 = 10^4$ V give the same synchrotron frequency of $\omega_{rf} \approx 4.25 \times 10^6$ cycles per second for the above configuration) (See Equation 4.14).

After the RF-cavity, the particle moves to the end with this updated energy. This energy change is also done by changing the longitudinal velocity.

When the particle reaches the bending section, its energy is shared by kinetic and potential energy, according to its radial position, again changing the longitudinal component of the velocity.

For example a particle at 1 cm from the design orbit has a potential energy of about 105 keV. According to the simulation results, this corresponds to $\Delta p/p_0 \approx 5 \times 10^{-4}$, which is significant. The code is given in Appendix C

5.3 Results

5.3.1 Energy conservation in the simulation

In the ideal case, where the particle starts with ideal momentum on the ideal orbit and the ring does not contain RF cavity, the total energy of the particle should be constant. Figure 5.3 shows that the change in the total energy of the particle is similar for several straight section lengths ranging from 14cm to 49m. A closer look at the plot gives 0.24 eV/s of rate of change. The initial energy of the ideal particle is about 233 MeV. This means that the change is about 1 ppm over 1000s.

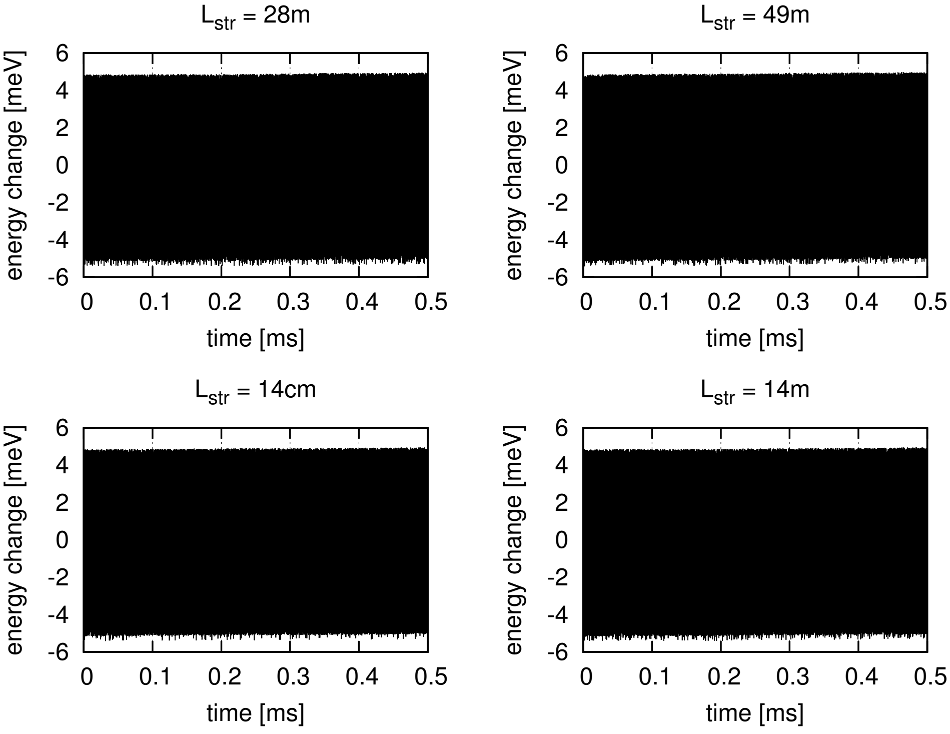

Figure 5.3: In the ideal case, the change in the total energy of the particle is almost same for several straight section lengths. It oscillates between about ±5 meV values, with an average slope of 0.24 eV/s.

5.3.2 Effect of straight section length on spin coherence time (SCT)

The first part of the study shows how the straight section length influences SCT. These simulations were done for 14cm, 14m, 28m, 49m of total straight section lengths. In the simulations, zero and non-zero cases of $\Delta p/p$ and z_0 are studied separately for various straight section lengths (L_{str}). x_0 is kept at zero for all cases.

Figure 5.4 shows the angle between the spin and momentum of the particle over 1 ms for several straight section lengths. The final angle between spin and momentum is about 1.7 μrad in 1ms, hence 1.7 mrad over 1 s. This means that 1.7 mrad/s is to be subtracted from the subsequent results.

Figure 5.5 shows the angle between spin and momentum for initial momentum error of $\Delta p/p = 2 \times 10^{-4}$. The visible oscillation is due to the RF cavity. The decoherence cannot be seen because of the scaling.

Figure 5.6 and 5.7 shows the highest and the lowest points of the oscillations seen in Figure 5.5. It is seen that although L_{str} affects the amplitude of the oscillations, the

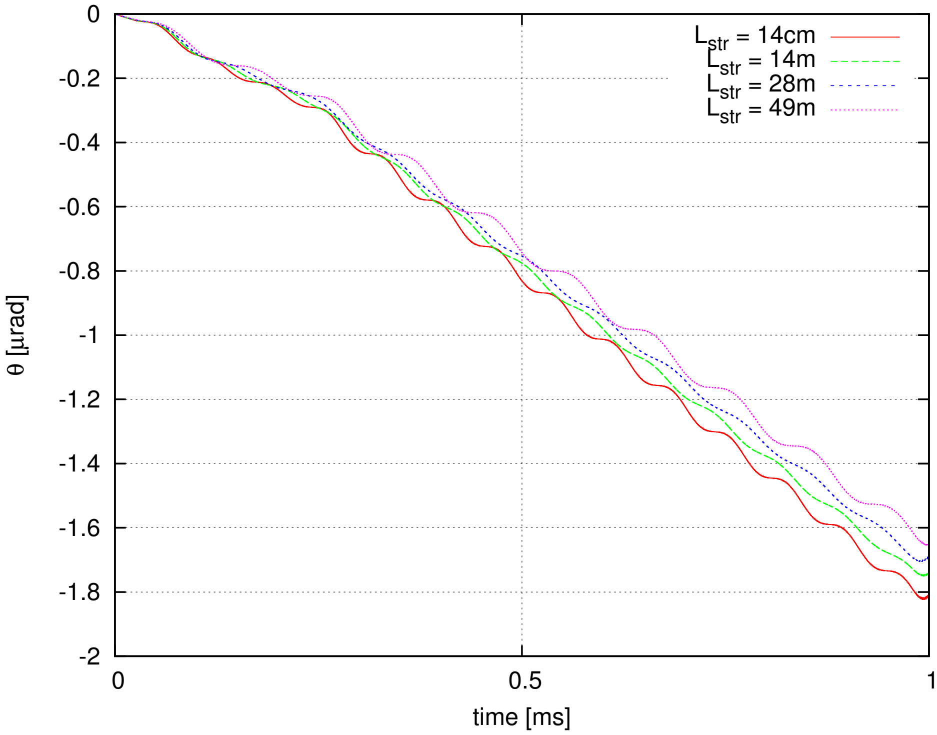

Figure 5.4: In the simulation with the RF cavity, small spin precession is observed even in the ideal case, because of the numerical precision of the approach. The rate of change is about 1.7 mrad/s. Therefore, it needs to be subtracted from the simulation results.

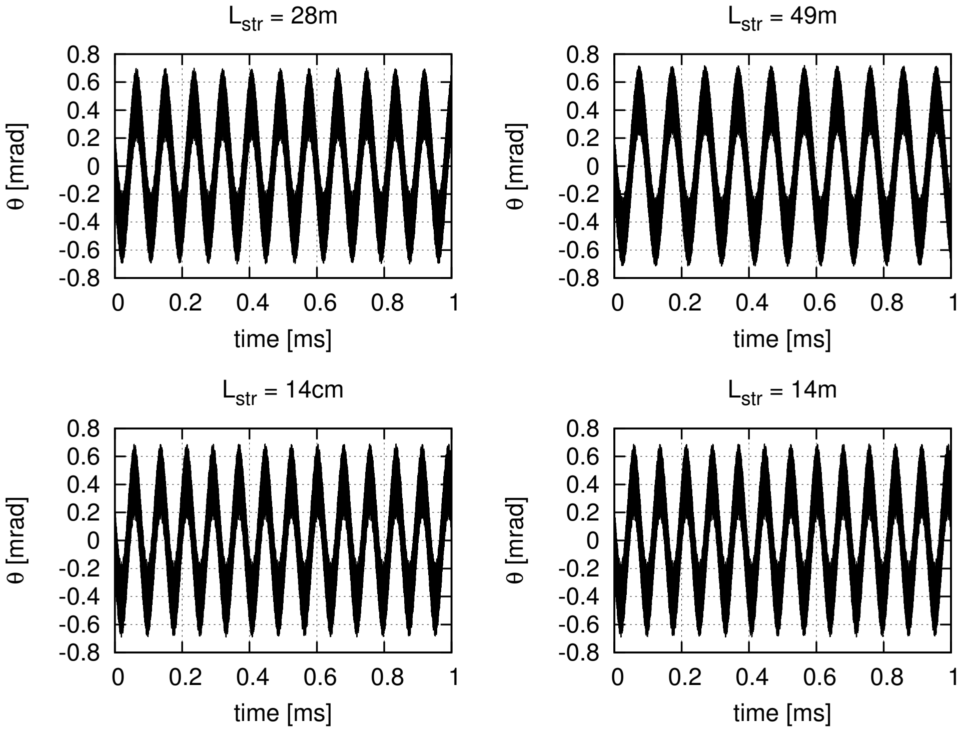

Figure 5.5: Angle between spin and momentum for $\Delta p/p = 2 \times 10^{-4}$. SCT can not be determined because of the scale. L_{str} is the length of the total straight section.

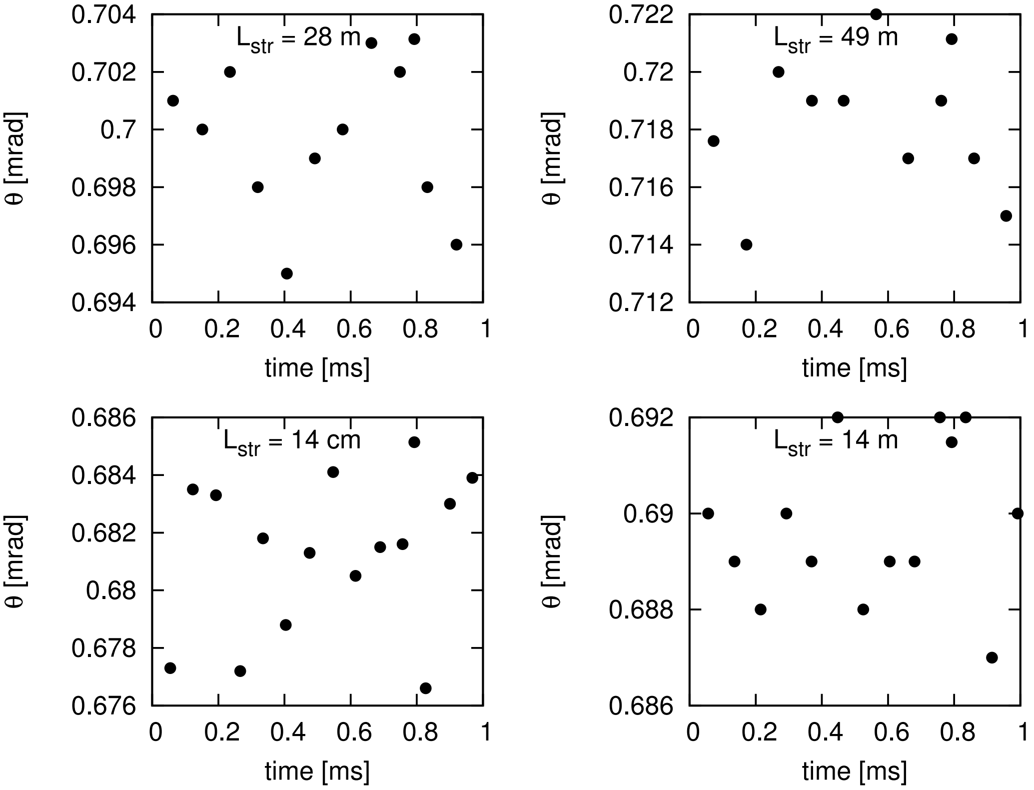

Figure 5.6: The highest points of the oscillations of Figure 5.5. The spread of the points are at the same order of magnitude for each straight section length.

change of amplitude is similar in all cases. Therefore, it can be concluded that no visible effect of L_{str} is observed on SCT for the case of $\Delta p/p = 2 \times 10^{-4}$. SCT of this case for 14m of L_{str} will be calculated more precisely in Section 5.3.6.

In magnetic rings, $t_{rev} - \gamma$ (revolution time vs gamma) is a line-curve. It is also a function of L_{str} and $d^2 t_{rev}/d\gamma^2$ contributes to spin decoherence.

Figure 5.8 shows the relationship between γ (proportional to the energy) of the particle and the revolution time around the ring. It is seen that for an electric ring, $t_{rev} - \gamma$ is not a line-curve at all, but a band. Although its pattern depends on the length of L_{str}, some symmetry in each pattern is clearly visible. This symmetry may be the reason of the independence (or weak dependence) of SCT on L_{str}.

For the ideal particle, the plot consists of only one point, corresponding to the magic momentum. Since the particle in this study has an offset of $\Delta p/p = 2 \times 10^{-4}$ in momentum, its energy will be different at a specific point in the ring in each turn. So, the RF cavity gives it some oscillation over time.

As explained above, tune is defined as the number of oscillations per turn: $Q = t_{rev}/t_{osc}$

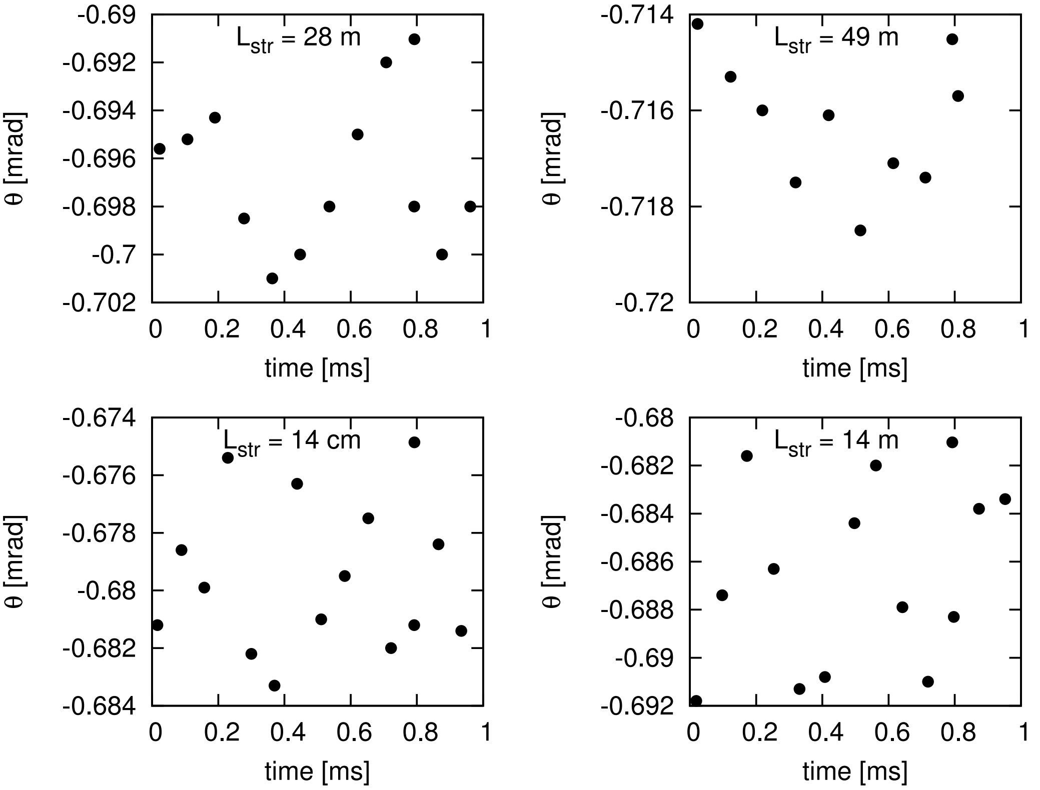

Figure 5.7: The lowest points of the oscillations of Figure 5.5. As in 5.6, the spread of the points are at the same order of magnitude for each straight section length.

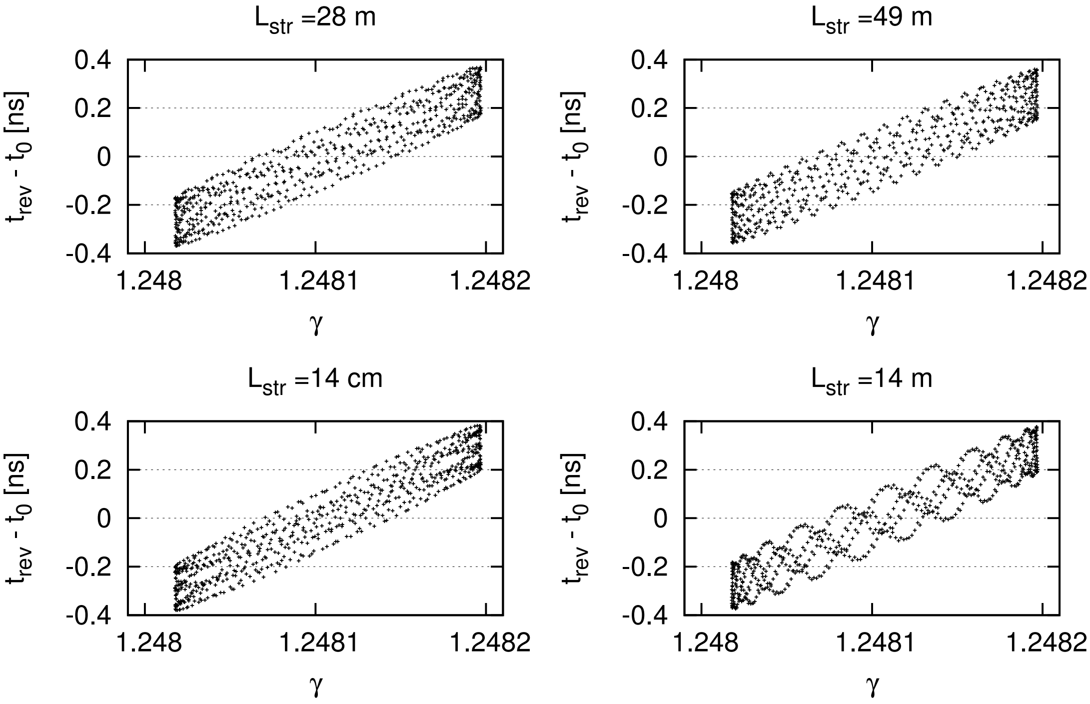

Figure 5.8: $t_{rev} - \gamma$ (revolution time vs gamma) is a band, rather than a curve. The symmetry of the band may be the reason of long SCT.

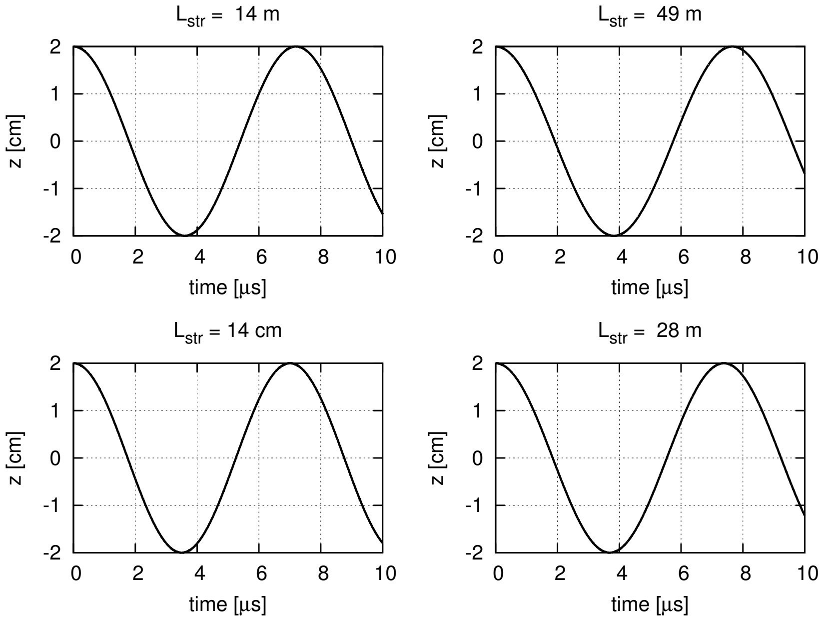

Figure 5.9: Vertical positions for z_0=2cm case. Vertical tune is defined as the ratio of revolution time around the ring to the vertical oscillation time. Thus, the tune in each case is $Q_z = t_{rev}/t^z_{osc} \approx 0.2$. Note that the revolution time of the particle around the ring is about 1.4μ s.

Figure 5.9 shows the vertical position of the particle for the case of $\Delta p/p = 0$ and $z_0 = 2$ cm. The plots show that in each case, the field index of $m = 0.04$ in electric ring gives about the same vertical tune of 0.2. The difference due to L_{str} is negligible.

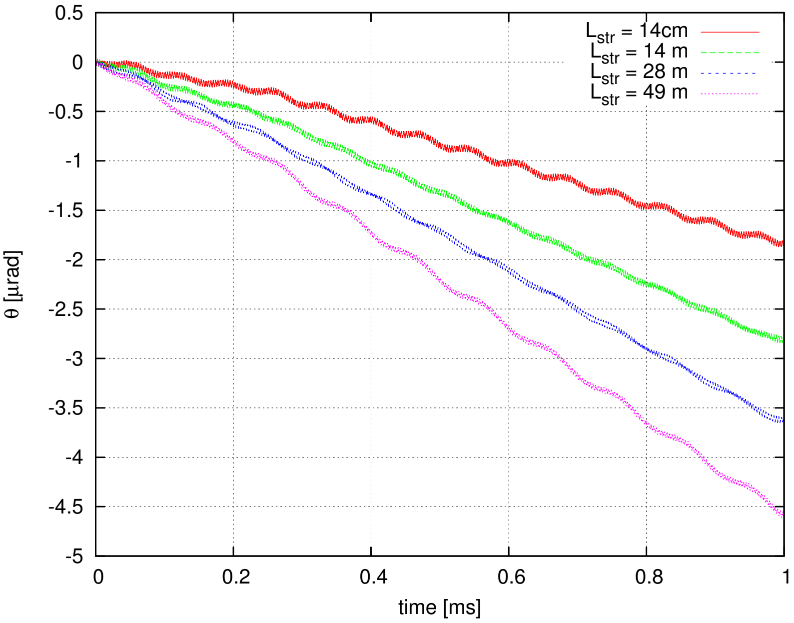

Figure 5.10: Angle between spin and momentum for $z_0 = 2$cm case. Spin decoherence seems to be 1.8 mrad/s for 14cm straight section, and about 2.8 mrad/s for 14m. Note that 1.7 mrad/s should be subtracted from the results (See Figure 5.4). Therefore, 14cm case has almost no spin decoherence and 14m case has about 1.1 mrad/s.

Figure 5.10 shows that the angle between the spin and momentum vectors changes by 1.8 mrad/s for 14cm. Subtracting 1.7 mrad/s from these results gives about 0.1 mrad/s of spin decoherence. In this study, the spin coherence time (SCT) is defined as the time needed to have 1 rad of angle between spin and momentum. Then, $z_0 = 2$cm of initial vertical position gives about 10^4s for 14cm, 900 s of SCT for 14m and about 500s for 28m. That is, despite visible dependence on the straight section length, z_0 case gives quite a big SCT for every straight section length.

5.3.3 Dispersion in an all-electric ring

If the particle is off magic-momentum, it moves on a closed orbit other than the ideal one. In magnetic rings, dispersion function (D) relates the radial deviation of the particle ($x(s)$) from the ideal orbit to the change in the momentum($\Delta p/p$) as given by Equation 5.5.

$$x(s) = D\frac{\Delta p}{p} \qquad \textbf{5.5}$$

However, the "normalized momentum change vs. radial deviation" graph of the case $\Delta p/p = 2 \times 10^{-4}$ and $x_0 = z_0 = 0$ case shows that dispersion function behaves in a much different way in electric rings (see Figure 5.11).

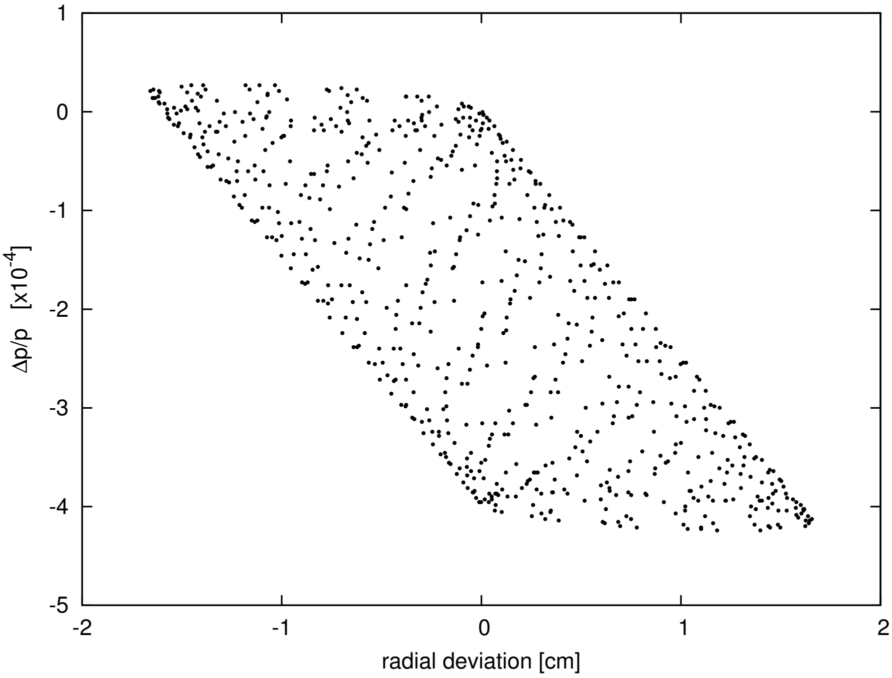

Figure 5.11: Dispersion relation given in Equation 5.5 requires a functional relationship between the normalized momentum change and the radial position of the particle. Unlike magnetic rings, this relation does not hold in electric rings.

5.3.4 Phase slip factor

The phase slip factor η relates the change in the momentum to the revolution time as shown in Equation 5.6. For a magnetic ring, η has a constant value and should be smaller than zero for a stable beam. Otherwise, the particles move bunch to bunch during storage, i.e. they are not captured within a single bunch, but they drift from one bunch to the next.

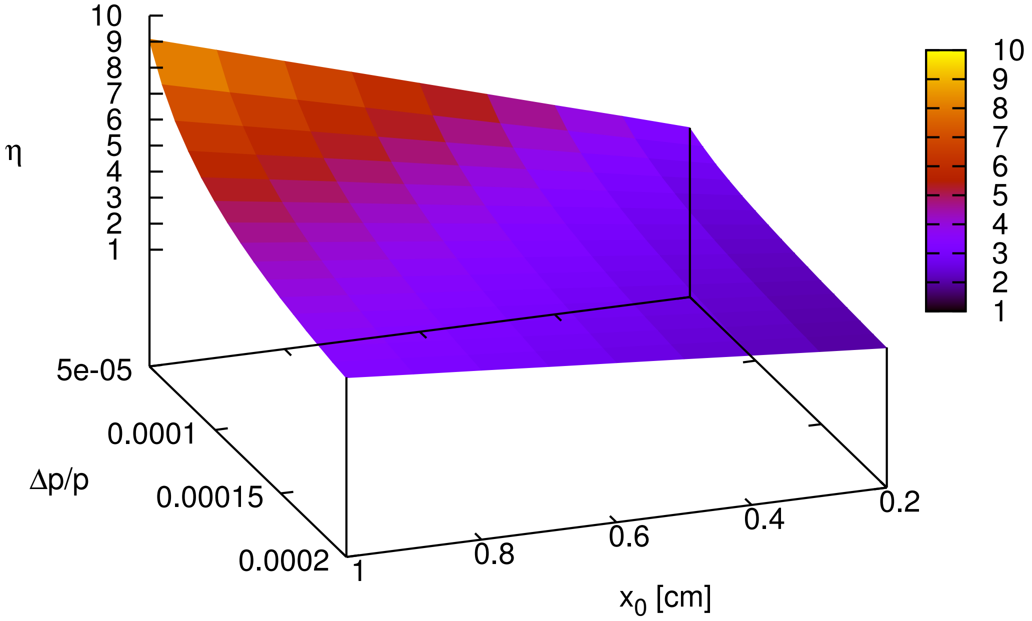

Figure 5.12: Unlike magnetic ring, phase slip factor η depends on $\Delta p/p$ and x_0 in electric ring.

$$\eta = \frac{\Delta T/T}{\Delta p/p} \qquad \mathbf{5.6}$$

This part of the study investigates the phase slip factor in an electric ring. The particle was given various initial values of x_0 (radial deviation) and $\Delta p/p$ (momentum deviation) for a constant straight section length ($L_{str} = 28$m). The RF cavity was turned off in this simulation. The revolution time of the ideal particle is subtracted from that of the particle with $\Delta p/p$ of momentum deviation to calculate η in Equation 5.6.

It is seen in Figure 5.12 that unlike magnetic ring, phase slip factor has a strong dependence on both $\Delta p/p$ and x_0.

5.3.5 Cancellation of the terms in g-2 spin precession

This part of the study is about the behavior of separate terms of the Equation 3.8. Integral of this equation gives the angle between spin and momentum (i.e. spin decoherence). The term in the parenthesis suggests that the angle does not change for a particle at magic momentum ($p_0 = m/\sqrt{a}$). The purpose of this part is to investigate the spin decoherence of a particle with off-magic initial momentum.

Table 5.1 shows the separate parts of Equation 3.8. The most important part of Y_1 is $\left[a-(m/p)^2\right]$. This means a finite SCT. The coefficient $(q/mc)\beta_0 E_0$ in Y_1 is for normalization.

Table 5.1: Separation of the parameters in Equation 3.8. The parameter Y_1 is multiplied by $(q/mc)\beta_0 E_0$ for normalization.

Y_1	Y_2	Y_3	Y_4
$\frac{q}{mc}\beta_0 E_0 \int \left[a-(m/p)^2\right] dt$	$\vec{\beta}\times\vec{E}$	$\vec{\omega}_a$	$\int \vec{\omega}_a dt$

The difference between Y_1 and Y_4 is the term $\vec{\beta}\times\vec{E}$. While it changes over time and hence weights $\left[a-(m/p)^2\right]$ at different rates at different positions in Y_4, Y_1 includes an average value $\beta_0 E_0$. (See Equation 3.8).

The separate terms in Table 5.1 are plotted for several configurations. The study was done for L_{str}=14m for the cases given in Table 5.2. In all cases, $z_0 = 0$.

Table 5.2: x_0 and $\Delta p/p$ configurations.

x_0	$\Delta p/p$	Figure
0	2×10^{-4}	5.13
1cm	2×10^{-4}	5.14
1cm	-2×10^{-4}	5.15
1cm	0	5.16

At first sight, SCT seems to be very small for a non-ideal particle, because its momentum will almost always be different from magic momentum due to betatron and synchrotron oscillations: To first order, it averages out to zero. But to second

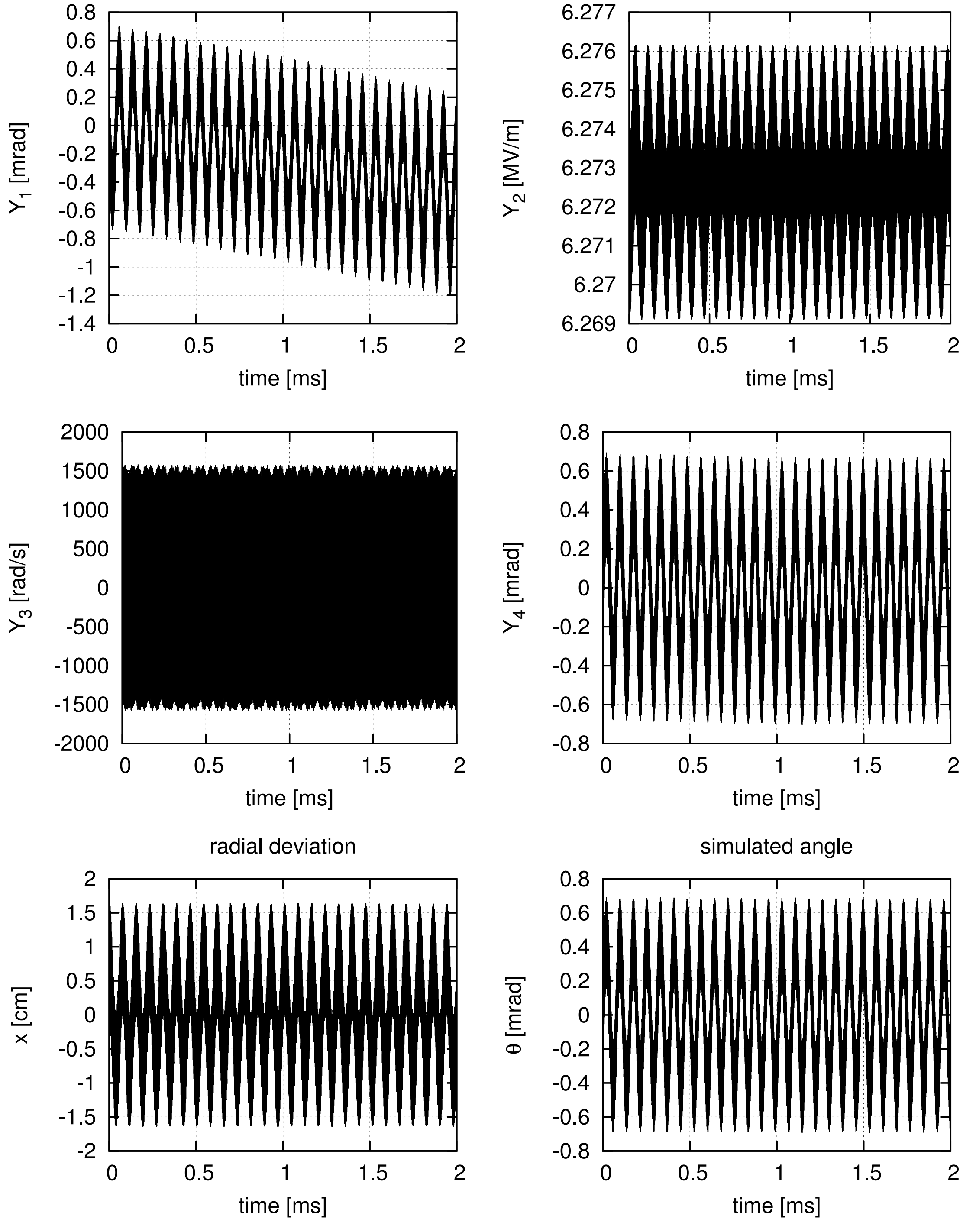

Figure 5.13: $x_0 = 0, \Delta p/p = 2 \times 10^{-4}$. While a clear slope is visible in Y_1, it has become very little in Y_4, hence a much longer SCT. This effect is due to Y_2, which is equivalent to $\vec{\beta} \times \vec{E}$. Y_4 and θ plots are essentially equal. The former is obtained from analytical calculations in each step, while the latter is obtained by calculating the angle between spin and momentum vectors of the particle.

order, it accumulates to some non-zero value. However, it is seen in the simulations that the g-2 spin precession (Y_4) is much smaller than expected, because of the Y_2 term. SCT is somehow recovered by $\vec{\beta} \times \vec{E}$, since it weights the term in the parentheses at

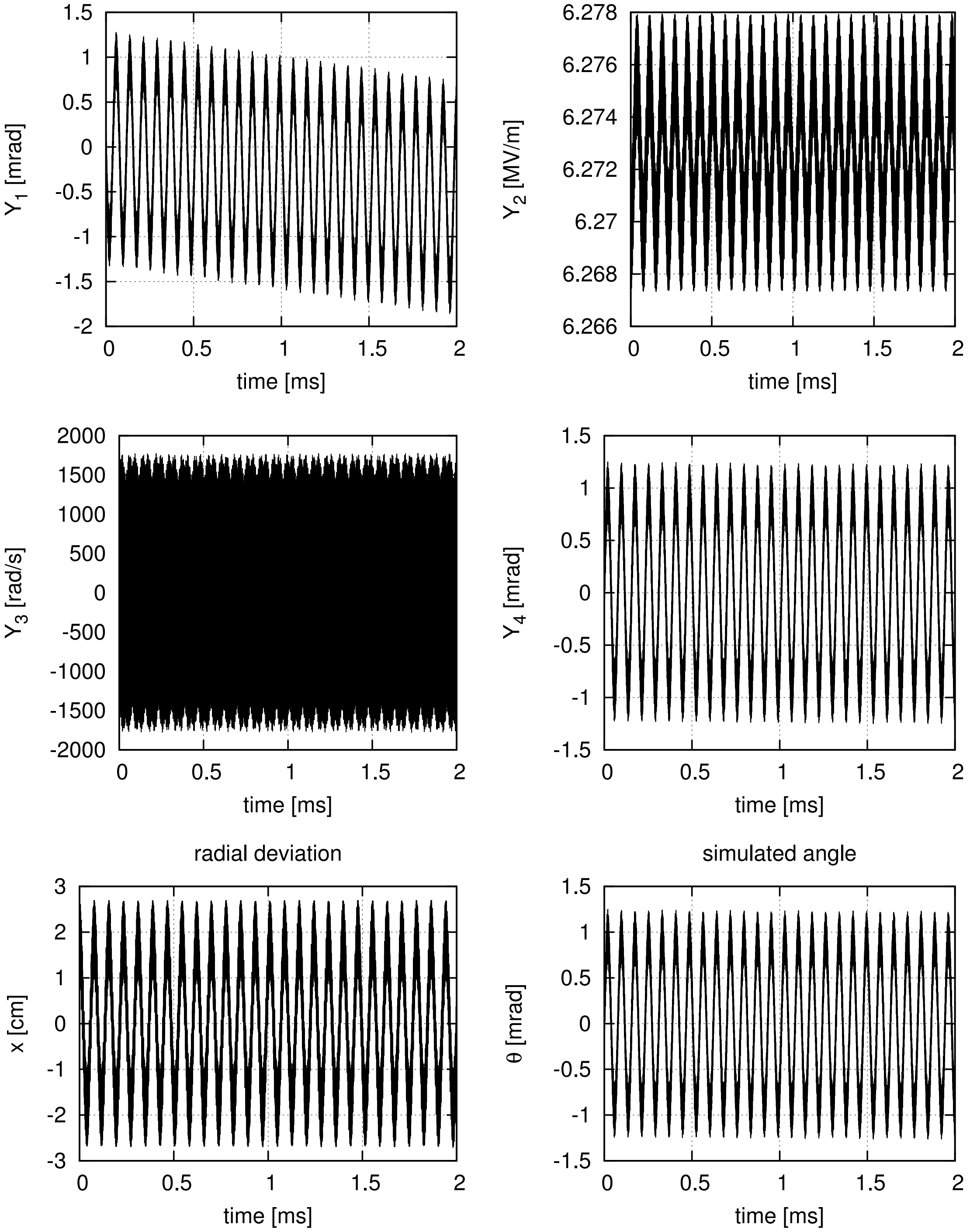

Figure 5.14: $x_0 = 1\text{cm}$, $\Delta p/p = 2\times10^{-4}$. Again, the tilt of Y_1 is recovered in Y_4. Because of 1cm of initial radial offset, the tilt is smaller than Figure 5.13. This effect will also be seen in Section 5.3.7.

different rates for different positions. To our knowledge, this effect is first mentioned in this study.

It is seen from Figures (5.13 - 5.16) that the term in parentheses in Equation 3.8 does not cancel by itself over time. However, the integration of the whole term almost cancels, because of the contribution of the term $\vec{\beta}\times\vec{E}$ as mentioned above. This

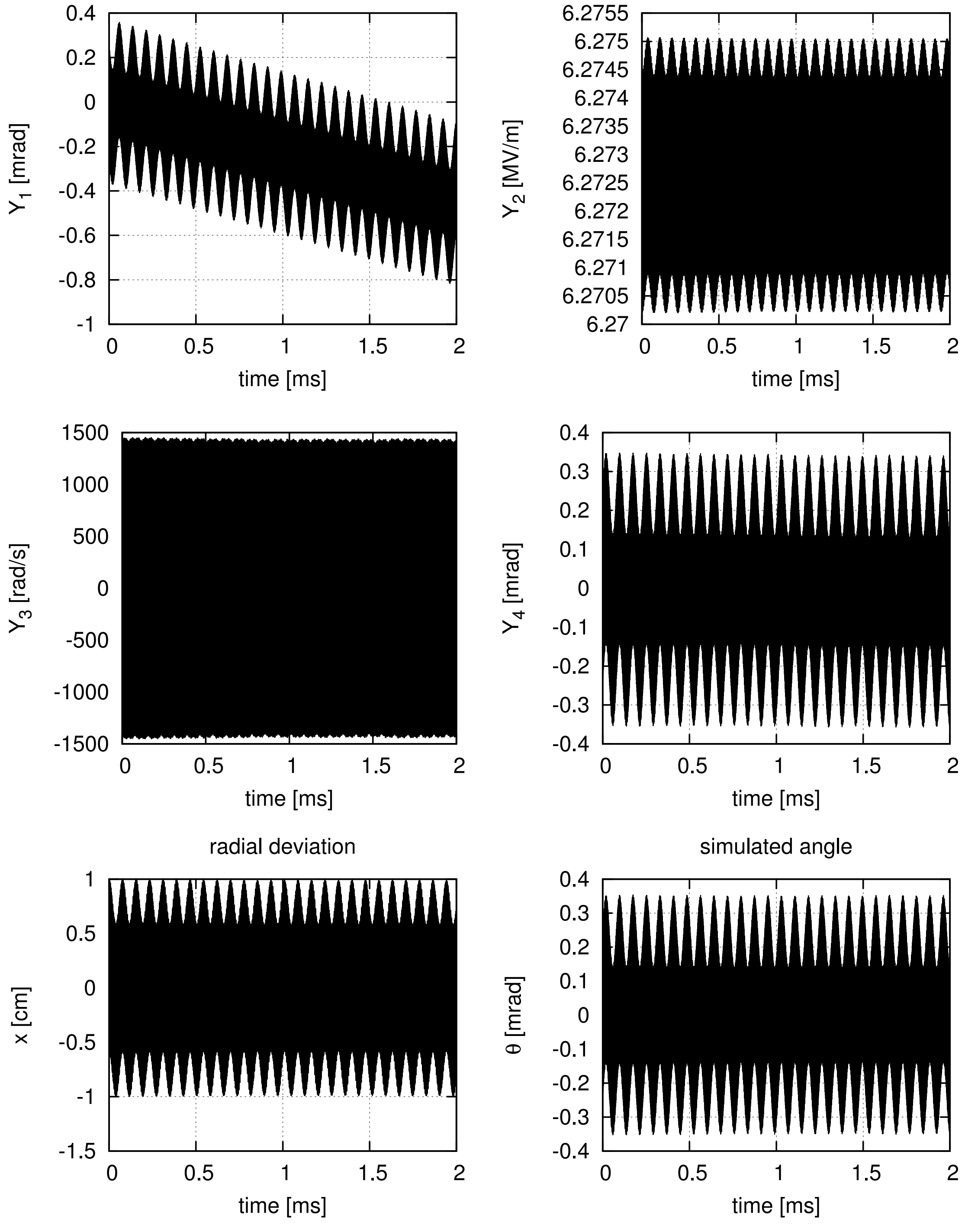

Figure 5.15: $x_0 = 1\text{cm}$, $\Delta p/p = -2\times10^{-4}$. This time, the tilt is bigger than Figure 5.13, because the signs of x_0 and $\Delta p/p$ are opposite. However, Y_2 compensates for this tilt too and Y_4 becomes much less inclined.

behavior makes the particles even with off-magic momentum have quite long SCT. Note that this behaviour is unique to electric ring, where both velocity and electric field depends strongly on position.

Figure 5.13 shows the above mentioned effect of Y_2 on Y_4, which prolongs the SCT. Here, g-2 spin precession is calculated in two ways: Y_4 gives the analytical calculation

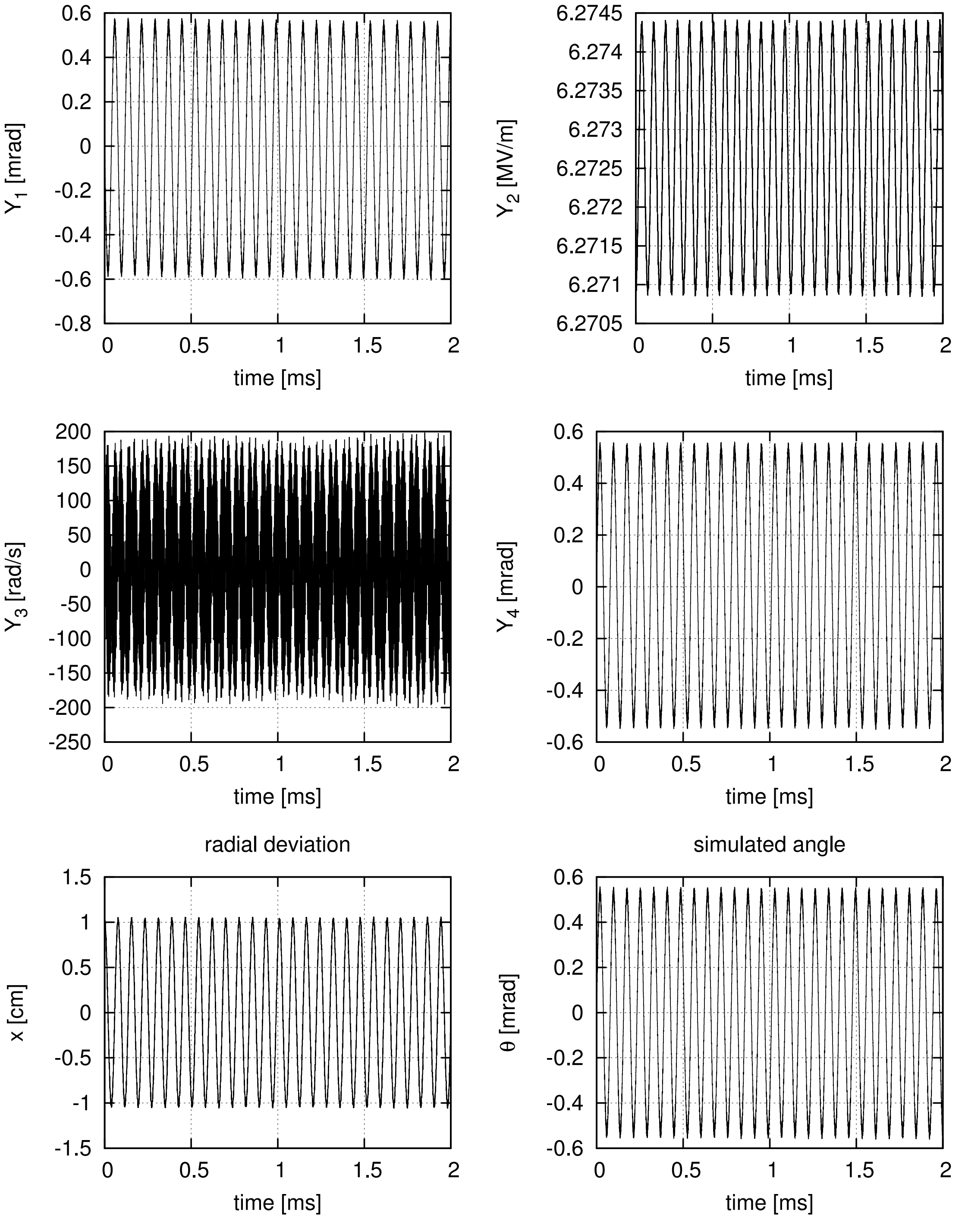

Figure 5.16: $x_0 = 1\text{cm}$, $\Delta p/p = 0$. Unlike the earlier cases, x_0 itself does not have a significant effect on Y_1 and the SCT.

(Equation 3.8) in each step, while the parameter θ records the angle between spin and momentum during the simulation.

When Figures 5.13, 5.14 and 5.15 are taken together into account, it is seen that the radial deviation of the particle increases when x_0 and $\Delta p/p$ have the same sign, while the slope of Y_1 decreases. The former effect will be seen also in Section 5.3.7.

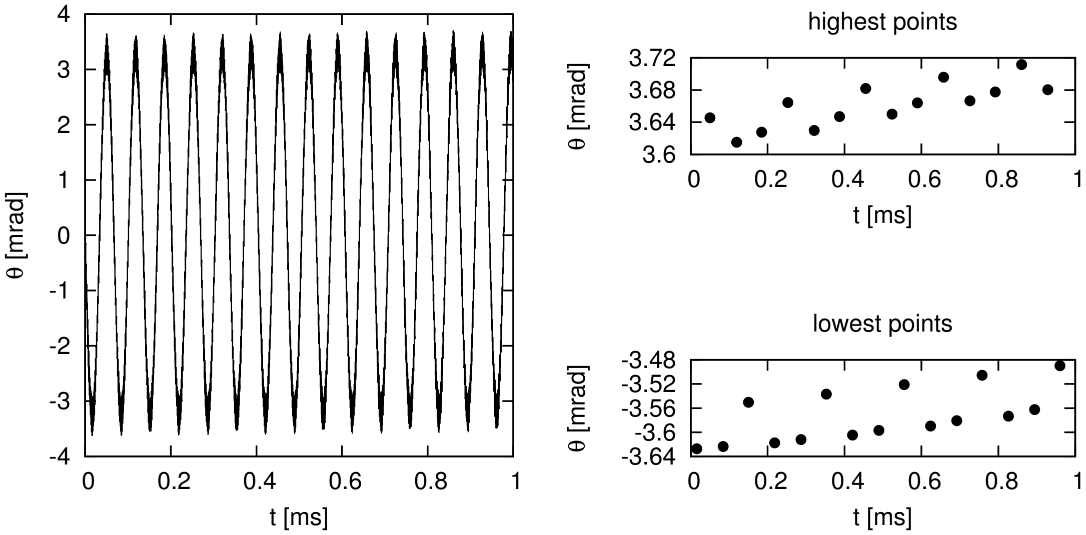

Figure 5.17: The graph on the left shows g-2 spin precession for the case of m=0.3. The highest and lowest points have slopes of 0.065 rad/s and 0.091 rad/s respectively. Averaging them gives 0.078 rad/s, which corresponds to about 13s of SCT.

If the particle starts at magic momentum even with a non-zero x_0, Y_1 oscillates around zero without a big deviation as seen in Figure 5.16. The fact that the maximum deviation is almost the same with the initial one shows that $\Delta p/p$ is a more dominant effect on radial deviation (Compare Figures 5.13 and 5.16).

5.3.6 Effect of the field index on g-2 spin precession

This part of the study includes the effect of the field index (m) on Y_4 of the earlier section. In these simulations, the initial values are set to $\Delta p/p = 2 \times 10^{-4}$ and $x_0 = z_0 = 0$ for all of the m values.

The spin coherence time is calculated using the slope of the g-2 precession over time. The angle diverges from zero, while oscillating around some average. The highest and the lowest points of the oscillation change with a certain slope as seen in Figure 5.17. SCT is calculated after averaging those two.

Figure 5.18 shows the spin coherence time for various field index values. Besides the asymmetry between the negative and positive m values, SCT seems to increase for m values closer to zero. In the above sections, the field index was taken to be 0.04, in order to have a vertical focusing of $Q_y = 0.2$. The slope of the highest and the lowest points of Figure 5.17 gets less clear for simulations over 1-2 milliseconds with m values closer to zero (See Figure 5.6 and 5.7). Therefore, the simulations were done

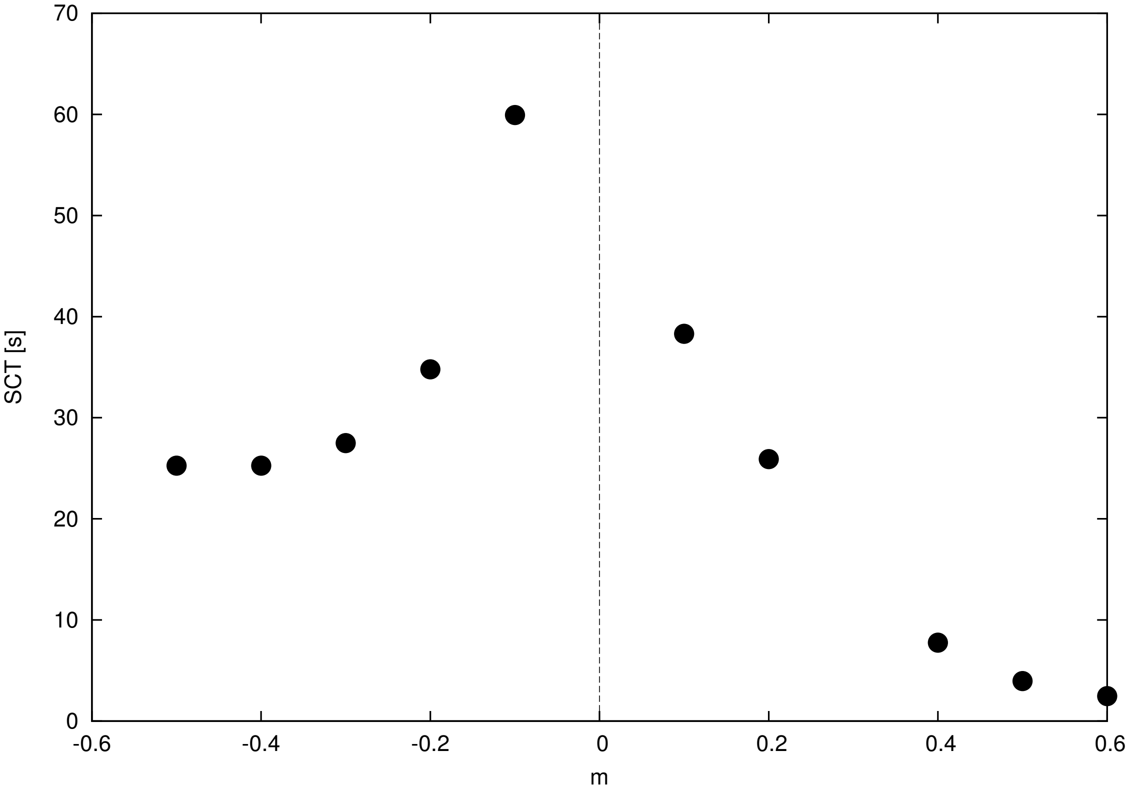

Figure 5.18: SCT is seen to increase while field index gets closer to zero. There is a visible asymmetry of SCT around zero field index.

for $|m| > 0.1$ only. Then, the SCT for $m = 0.04$ is calculated by fitting the data with positive m values.

Figure 5.19 shows the field index dependence of SCT in the logarithmic scale. Fitting the data to a line gives 58s of SCT for $m = 0.04$. See Figure 5.19).

Figure 5.20 shows the dependence of SCT on $\Delta p/p$ for $m = 0.04$. The particles with higher momentum spread are going to be at the edges of the beam. Therefore, they will be extracted before the others. In the experiments the highest momentum spread is planned to be $\Delta p/p = 2 \times 10^{-4}$. Therefore, the particles at the edge of the beam will have 58s of SCT and should be extracted in 58s. Then, the ones with $\Delta p/p = 10^{-4}$ should be extracted in 164s and so forth. It is seen from the figure that the SCT will be more than 1000s with this extraction method. Moreover, the field index will be set to m=0.01 after 100s, which will increase the SCT even more.

5.3.7 Admittance of the ring

In this part of the study, the admittance of the ring is calculated. The particle runs through the ring with several initial configurations of $x_0, \Delta p/p$ and θ_0 values and the

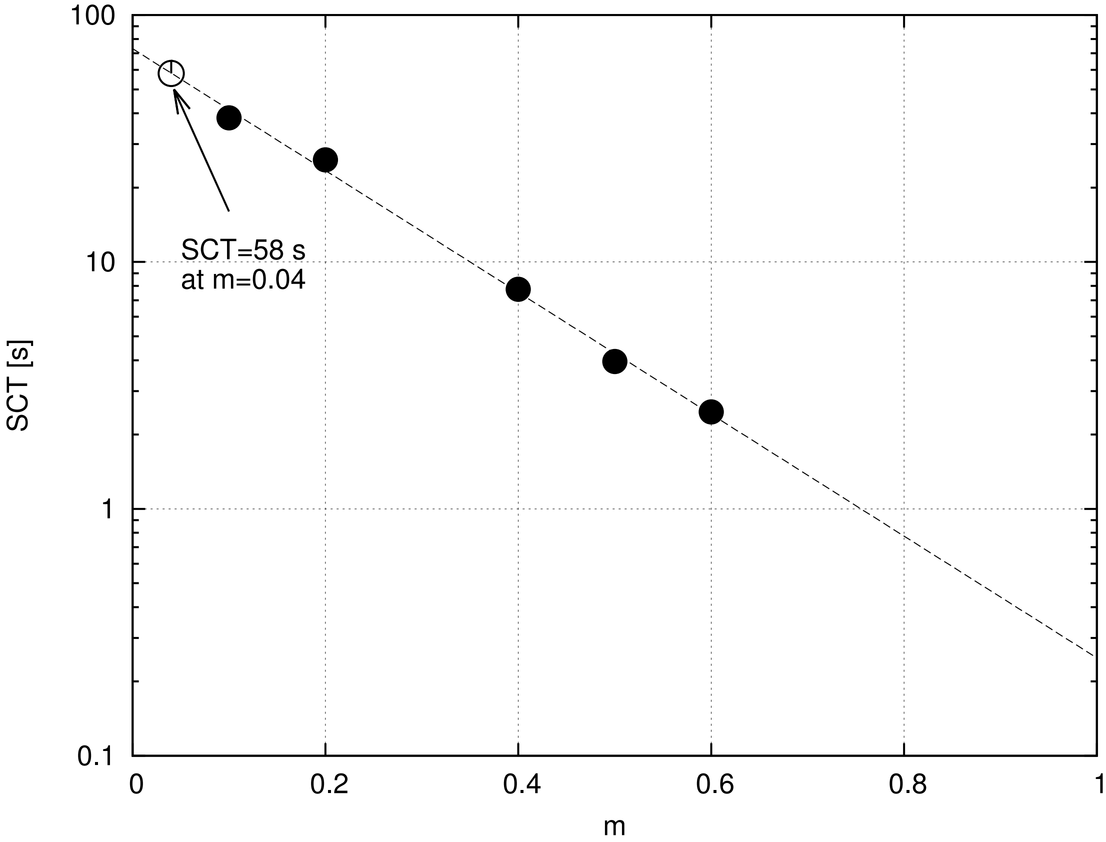

Figure 5.19: The positive m values of Figure 5.18 are fitted to a line in logarithmic scale. $m = 0.04$ gives 58s of SCT.

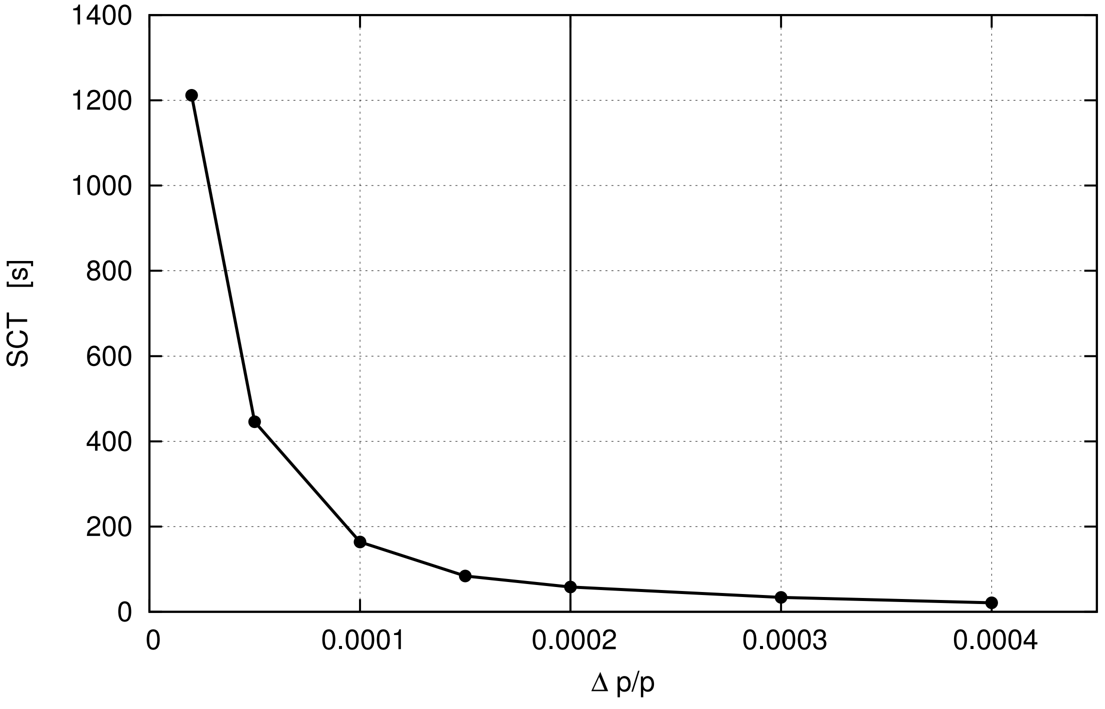

Figure 5.20: Dependence of SCT on $\Delta p/p$ for $m = 0.04$ shows that the beam can be stored for 10^3s, provided that the particles with higher momentum spread being extracted first.

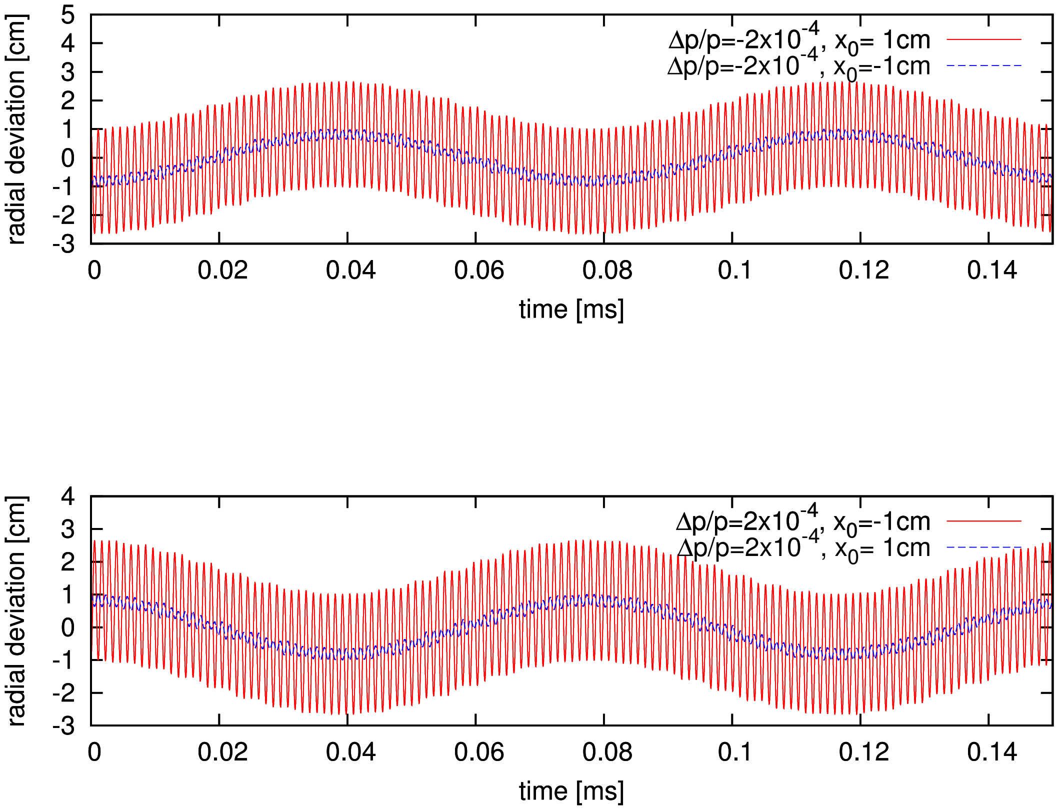

Figure 5.21: The radial oscillation amplitude of the particle is about 2.5 cm when $\Delta p/p$ and x_0 have the opposite signs and less than 1 cm when they have the same sign. The oscillation with smaller frequency comes from the RF cavity.

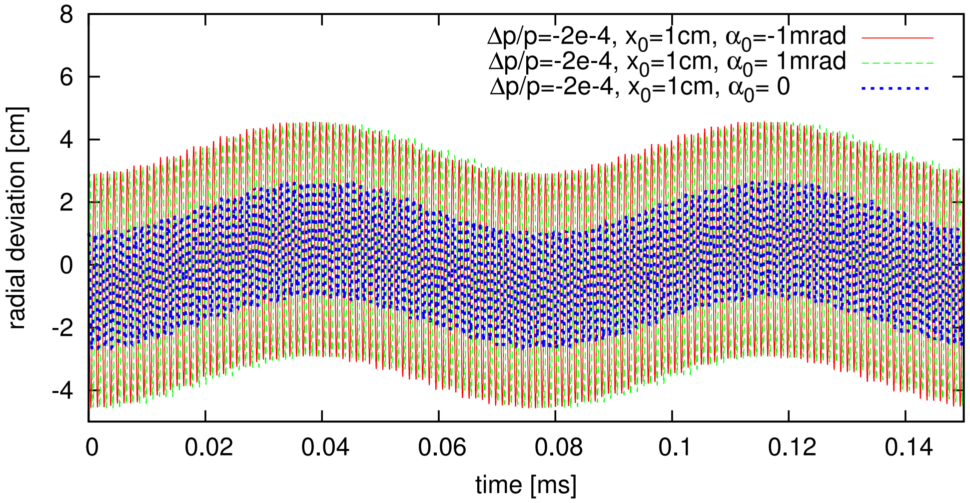

Figure 5.22: Radial oscillations for various configurations of $\Delta p/p$, x_0 and θ_0. 1 mrad of initial angle makes the radial oscillation amplitude twice bigger. $\theta_0 = 0$ gives an oscillation amplitude of about 2.5cm, while $\theta_0 = \pm 1$ mradgives a bit more than 4cm.

RF cavity is on. These configurations correspond to different radial oscillations. The particle starts from the straight section in the simulations.

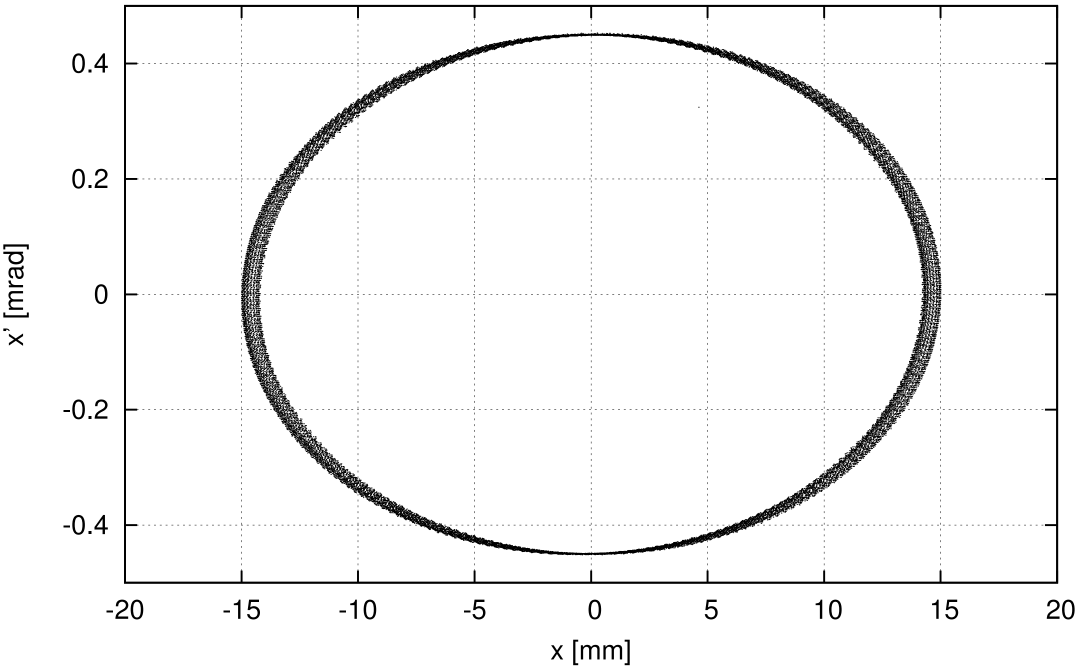

Figure 5.23: Phase space diagram of a particle starting with initial angle of 0.45 mrad at the design orbit with magic momentum. The particle has an oscillation amplitude of about 1.5cm.

Figure 5.21 shows that the initial radial deviation is the biggest when x_0 and $\Delta p/p$ have opposite signs. The radial oscillation decreases by about 1.5cm when they have the same sign.

Figure 5.22 shows the deviation for initial values of $\Delta p/p = -2 \times 10^{-4}, x_0 = 1$ cm and $\theta_0 = 0, \pm 1$ mrad. These extreme cases of momentum and initial position conditions are chosen to set a limit for the acceptance. 1 mrad of initial angle increases the oscillation amplitude by 4 cm. Therefore, having $\Delta p/p \leq 2 \times 10^{-4}$ and $x_0 \leq 1$cm, the initial angle should be limited to some value.

Figure 5.23 shows that $\theta_0 = 0.45$ mrad with $\Delta p/p = 0$ and $x_0 = 0$ gives an oscillation amplitude of 1.5cm. For a magnetic ring, this corresponds to admittance of:

$$\varepsilon = \pi x'^2 \beta = \pi x'^2 \frac{R}{Q_h} = (0.45 \times 10^{-3})^2 \times \frac{40}{1.3} \pi = 6.2\pi mm \cdot mrad \qquad \mathbf{5.7}$$

Besides the vertical admittance, the horizontal admittance is also at the same order of magnitude with the magnetic ring.

6. HIGH VOLTAGE TESTS ON METAL PARALLEL PLATES

The bending electric field in the pEDM experiment is proposed to be 10.5 MV/m at 3cm of gap in a ring with 40m of radius. Another critical question is if this high gradient at 3cm of gap is achievable. If achievable, how would a spark affect the plates and the field? Would it be recoverable after a spark? And finally, does the maximum field that plates can handle depend on gap?

Working with high gradient requires some conditioning on the plates followed by several treatments. These processes improve the plates against breakdowns. Hence, the conditioned plates can handle higher electric field. The condition of the plates is parametrized by two parameters: β and A_e.

This chapter starts with the definition of field index and the parameters β and A_e. Then, it gives an overview of breakdown mechanisms and the methods used for treatment and conditioning. Finally, it describes the test setup and discusses the results.

6.1 Field Emission and β Parameter

Field emission is the leakage of free electrons from the surface of a metal with high electric field. Essentially, it is quantum tunnelling of electrons through the potential barrier of the surface at high gradients (order of MV/m). The barrier width for an electron at Fermi level is about 1nm on the surface. Field emission is first modelled by Fowler and Nordheim in 1928 [43].

The model predicts a current density J for a given electric field and material:

$$J = \frac{1.54 \times 10^{-6} \times E_{loc}^2}{\phi} \times \exp\left(10.4/\sqrt{\phi}\right) \times \exp\left(-2.84 \times 10^9 \phi^{1.5}/E_{loc}\right) \qquad \textbf{6.1}$$

where E_{loc} is the electric field of the emitting region and ϕ is the work function of the current emitting material. For large surfaces, E_{loc} is typically much higher than the average electric field on the surface, since the emission is mostly due to the rough spots, such as micro-protrusions and surface inclusions. Therefore, the electric field E_{loc} of Equation 6.1 is $E_{loc} = \beta E_{avg}$, where E_{avg} is the average electric field on the plates and

β is called the "enhancement factor", which depends on the protrusion geometry of the surface. It can be concluded that the field emission is the least for smooth and hard surfaces.

Using $I = J \cdot A_e$ and $V = E \cdot d$, Equation 6.1 turns into:

$$log\left(\frac{I}{V^2}\right) = log\left(\frac{3.24 \times 10^{-5} A_e \beta^2}{d^2}\right) - \frac{31.75 \times 10^9 \times d}{\beta}\left(\frac{1}{V}\right) \qquad \textbf{6.2}$$

where A_e is the area of the emitting spot, V is the potential difference and d is the gap between parallel plates respectively. Fitting the $log(I/V^2)$ vs. $1/V$ data of Equation 6.2 to a line gives the total β and A_e values on the surface of the cathode plate.

6.2 Breakdown Mechanisms

Under certain circumstances field emission initiates breakdown. Although the breakdown mechanism is not understood completely, there are some models to explain this phenomena. (Details can be found in [44], [45] and [46]).

- For small gaps less than 2mm, the field emission results in melting of the cathode material. The melted particles form a plasma between the plates, then accelerate towards the anode to produce spark.
- At gaps larger than 4-5 mm, the accelerated particles mentioned above may cause some anodic droplets to be released. Then, these droplets hit the cathode to produce cathodic droplets. In some configurations, this process loops to result in sparks.
- Dust-like particles between the plates may be ionized and accelerated to produce droplets as in the second case [47].

Domination of the anode in the breakdown process starts at a few mm of gap (See [48], [49] and [50] for various discussions).

To minimize the breakdowns, the cathode material should have a big work function and a smooth surface to minimize the field emission, and the anode should be a hard material to avoid droplets to be released. This can be done by surface treatment and surface conditioning procedures explained below.

Still, there are some other parameters that affect the breakdown tendency, such as thermal conductivity, electrical conductivity, surface tension and so on [51]. Therefore, it is hard to decide the best combination of anode and cathode that gives the minimum breakdown rate (See [52], [53]).

6.3 Surface Treatment

Small field emission requires some surface treatment prior to its use. For high voltage works, the surface must be mirror finished. This is done by polishing the surface.

After polishing, several treatments can be applied to the surface:

- High pressure water rinsing (HPR): High purity deionized water of about 1000 psi bombards the surface for cleaning [54], [55].
- Ion Implantation: The surface is smoothed by implanting ions. After this process, the surface has a uniform work function and chemical composition [56], [57].
- Gas Cluster Ion Beam Implantation (GCIB): In this method, ions are sent to the surface in a cluster, with slower speed than the case of ion implantation. This minimizes the damage on the surface. The surface is coated uniformly in this case too [56], [58].

6.4 High Pressure Water Rinsing

HPR is a recently developed method for removing the particulate contaminants from the surface. Besides, it even alters the physical and chemical characteristics of the surface. Therefore, it also changes the work function of the metallic surface as in GCIB and ion implantation methods. Since it is a scalable process, it can be used in large areas as well.

The process is based on bombarding the surface with pure water jets. The typical pressure used is about 1000 psi and the jet speed can reach a few hundred m/s [59].

HPR gives one of the best results in treatment of plates.

6.5 Conditioning the Plate

Plates should be conditioned prior to their use, in order to increase the maximum E-field they can handle by another order of magnitude. There are several methods of conditioning a surface:

- Current conditioning: The idea behind this method is to keep the current passing through the gap between the parallel plates below breakdown current. This is achieved by resistors connected in series to the parallel plates. The voltage is increased by a small amount after the current stabilizes, which takes about 30 minutes. At each step, the current shows small activities at noise level, and sometimes micro-discharges [44].
- Spark conditioning: This method is used to clean the field emitting spots by the sparks that they generate. In this method, the voltage of the plates is firstly increased slowly until a dark current of nA level is achieved. Then, the voltage is increased in small steps, until a spark occurs. This process is repeated many times until the plates get conditioned. The recorded current-voltage values can be used to characterize the condition of the plates [60].
- Glow-discharge conditioning: This method is applied by filling the vacuum between the plates by some noble gas like Argon, or Helium. Then, increasing the voltage, the gap is filled by plasma, which cleans the surface either by sputtering (physical), or desorption (chemical). The pressure is typically kept at about μbar level [61].
- Gas conditioning: Like glow-discharge conditioning, the gap is filled by some gas at a μbar level pressure. Then the potential is increased progressively as in current conditioning. The period of increasing the potential is about 20 minutes [62].

6.6 Current Conditioning

The field emitting spots on the surface has the highest E-field. When the breakdown happens, the spark most probably hits those spots. Hence, the spark cleans off the spot that it originates from, provided that it is not too powerful. Otherwise, it forms new sparks where it hits (See Figure 6.1).

Figure 6.2 shows a typical readout of the voltage on the plates and the current from the cathode to the ground in a typical spark conditioning. The activities below 30 nA of current are considered to be small. They do not have much help to conditioning. Therefore, the current remaining below 30 nA for about 5 minutes means stability of the dark current. Then, the voltage should be increased for more conditioning.

Increasing the voltage before reaching the stability may lead to activities at high currents, even in μA range. Current at this range usually damages the conditioning of the plates.

Current is usually kept between 30 nA and 500 nA for an effective conditioning. Figure 6.2 has several distinct regions showing this. One of them starts at about 1000s. The conditioning current fluctuates around 130 nA. At about 5700s, the current suddenly drops to about 0.5 nA. This means, the spot causing the dark current was cleaned. Then, the voltage is increased after 5 minutes of stability.

The current measured on the cathode is negative. Yet, positive current measurements were taken at various times too. This is because of the ionized droplets from one plate to the other. Although these droplets carry high current, they normally do not change the condition of the plate.

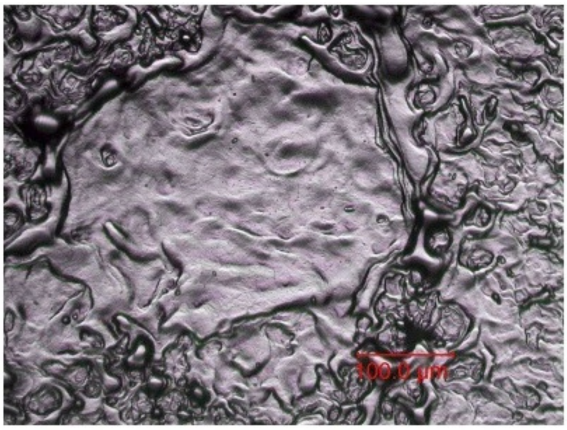

Figure 6.1: A powerful spark melts the surface once it hits there and produces a crater, which has some new-formed spikes at the edges. The picture covers an area of 0.56mm×0.4mm in one of our plates.

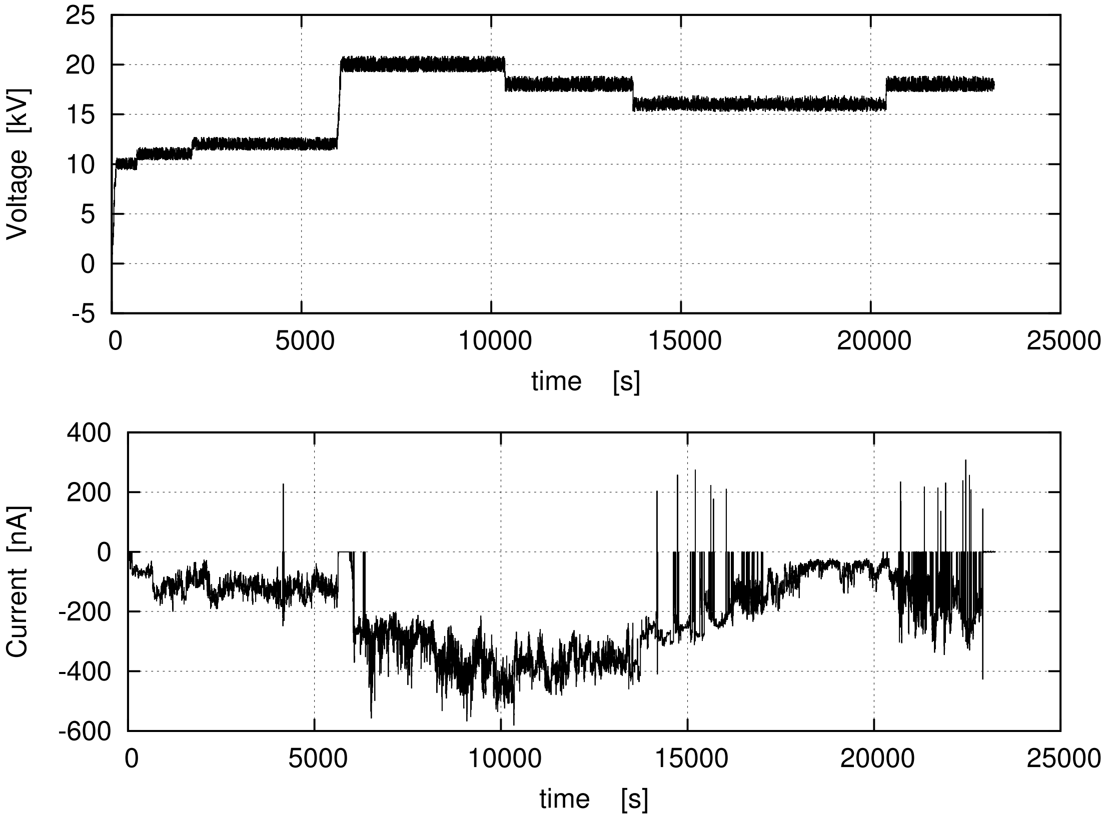

Figure 6.2: A typical readout of high voltage (HV) potential on the plates and the dark current vs. time.

On the other hand, sparks may have effects on the conditioning of the plate. Figure 6.3 shows two different conditioning data. In the left side of Figure 6.3, a spark of about 1.2μA improves the conditioning of the plate, so that the dark current decreases. In the right side of Figure 6.3, the first two sparks do not change the conditioning much. Yet after the third one, the dark current increases visibly, which means that conditioning gets worse.

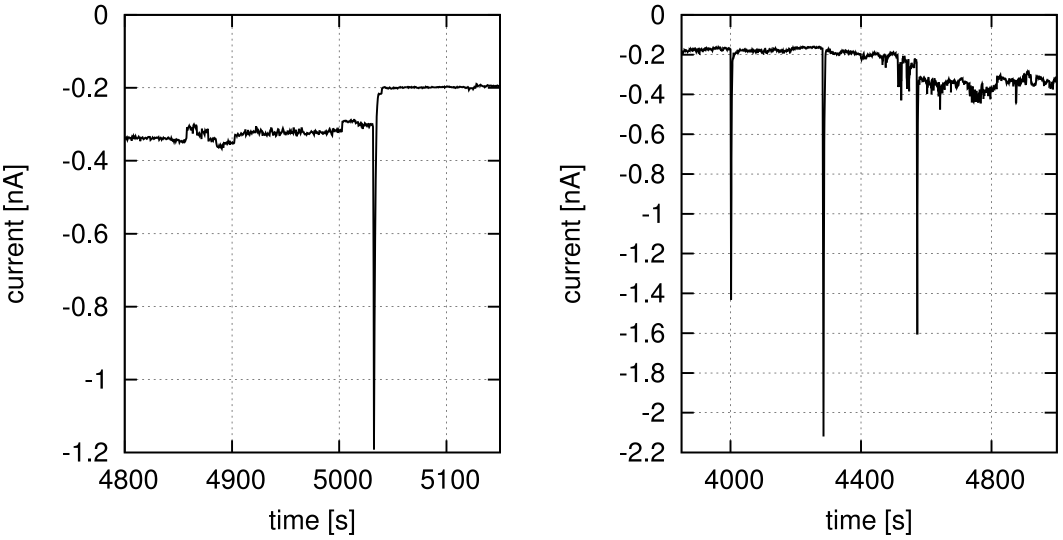

Figure 6.3: Some sparks affect the condition of the plates. (Left) The spark improves the condition of the plate. (Right) There are three sparks. The first two does not change the condition of the plate a lot, while the third one worsens it.

6.7 Test Setup

The test setup was borrowed from Cornell University. It basically consists of two stainless steel parallel plates in a vacuum tank (See Figure 6.5).

The plates in the tank have about 6cm of radius. The gap between them can be adjusted using three screws accessible via feedthroughs from the outside. The bottom plate sits on those screws. The resolution of the screws is 50 μm.

The top plate is connected to the high voltage power supply (with maximum voltage of 120 kV) through a rod and resistors to limit the current. It has a corona shield around the connection of the resistors with the rod. The bottom plate is connected to the ground through a 6485 Keithley picoammeter to measure the dark current (See Figure 6.6 for equivalent circuit).

It has a vacuum connection and a vacuum readout. The vacuum pressure is kept at about 10^{-8} Torr during the tests.

The HV control and the readout from the power supply are done using a DaqBook/2000 Series DAQ device. Both the HV I/O and the picoammeter readout were done using a Labview interface (See Figure 6.7).

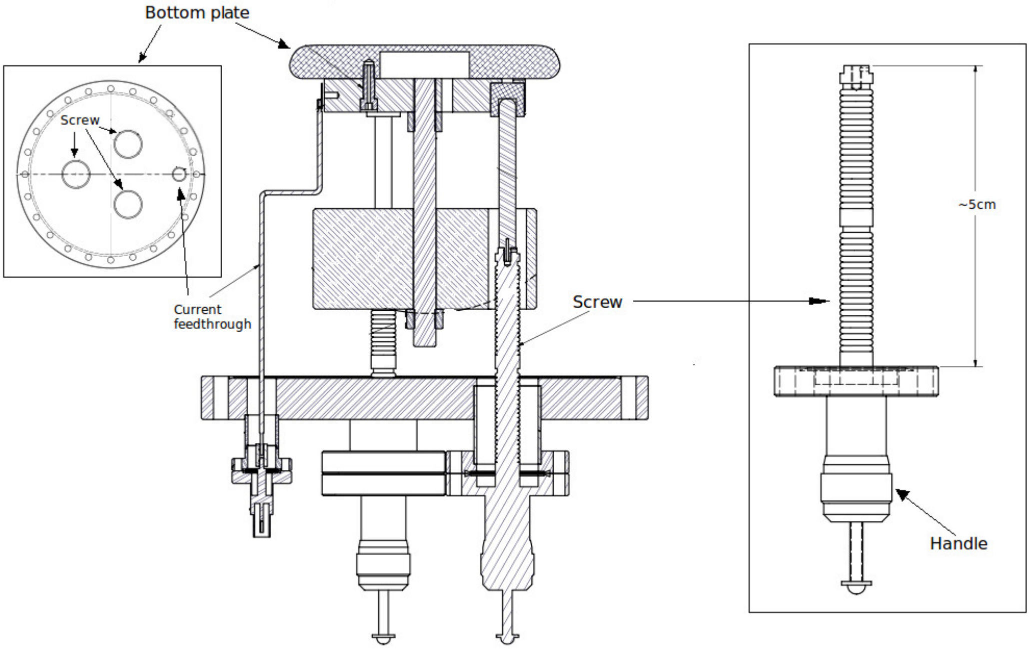

Figure 6.4: The bottom plate sits on three screws. The pitch is 1 mm. The resolution is 50 μm, since the handle of the screw has 20 divisions.

The plates were electropolished and HPR'ed before the tests. However, the cover was broken and they were scratched by an accident during the shipping. Therefore, the initial condition of the plates was not perfect.

The test system was set up in a clean room followed by a clean-up. Then, the air is pumped out prior to bake-out at 150^0C for 3 days.

The HV I/O and the current readout was done via computer and the data was stored to a text file. The data was taken twice a second.

A similar setup was used by two groups before. One of the groups had their plates treated by GCIB [63]. The other had them HPR'ed [64]. Both groups made the conditioning at 4mm gap between the plates. The first group have achieved 20 MV/m at 1pA, which is equivalent to 27 MV/m with 100 pA and about 35 MV/m with 100 nA. Before conditioning, the plates with GCIB treatment held about 8-10 MV/m less electric field for all currents in the range. And before the GCIB treatment, they held another 10 MV/m less. The results of the second group, whose plates were HPR'ed before, had similar results about 35 MV/m.

The spark has the power $P = V \cdot I$, where V is the potential difference between the plates and I is the current. Since the dark current is determined by electric field rather than the potential difference, it remains the same when the voltage and the gap are decreased by the same ratio. Then, one can initiate sparks with smaller energies, having a smaller gap between the plates. This means less damage on the plates. Therefore in this study, the conditioning was done at 1mm gap which is relatively small.

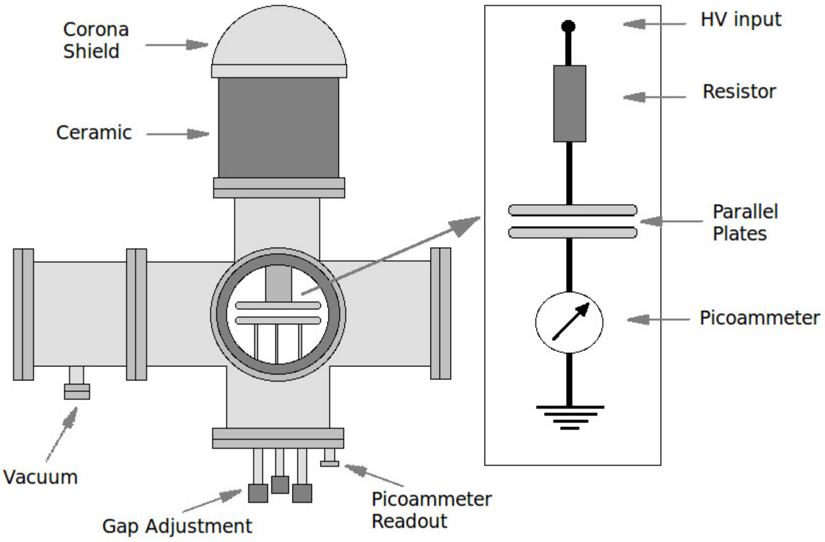

Figure 6.5: Test system used for conditioning the plates. It is about 150cm tall and 100cm wide. The box on the right shows the electrical circuit within.

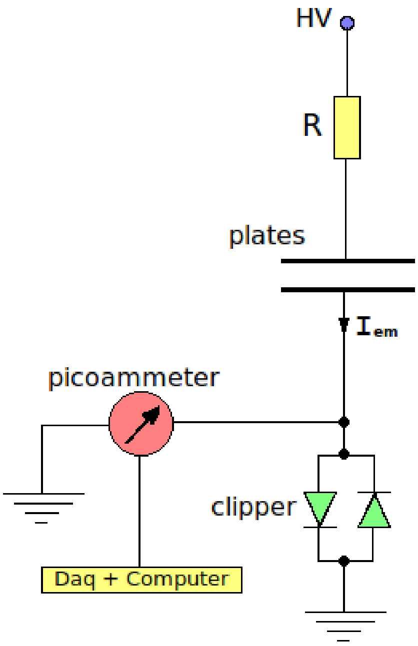

Figure 6.6: The equivalent circuit of the test system. High voltage is applied to the plates through 14GΩ resistors to limit the current (I_{em}) to about 10μ A, which is read by picoammeter. The diode clippers are connected parallel to the picoammeter for protection. Current readout, as well as high voltage control and readout are done using a DAQ device and a Labview interface.

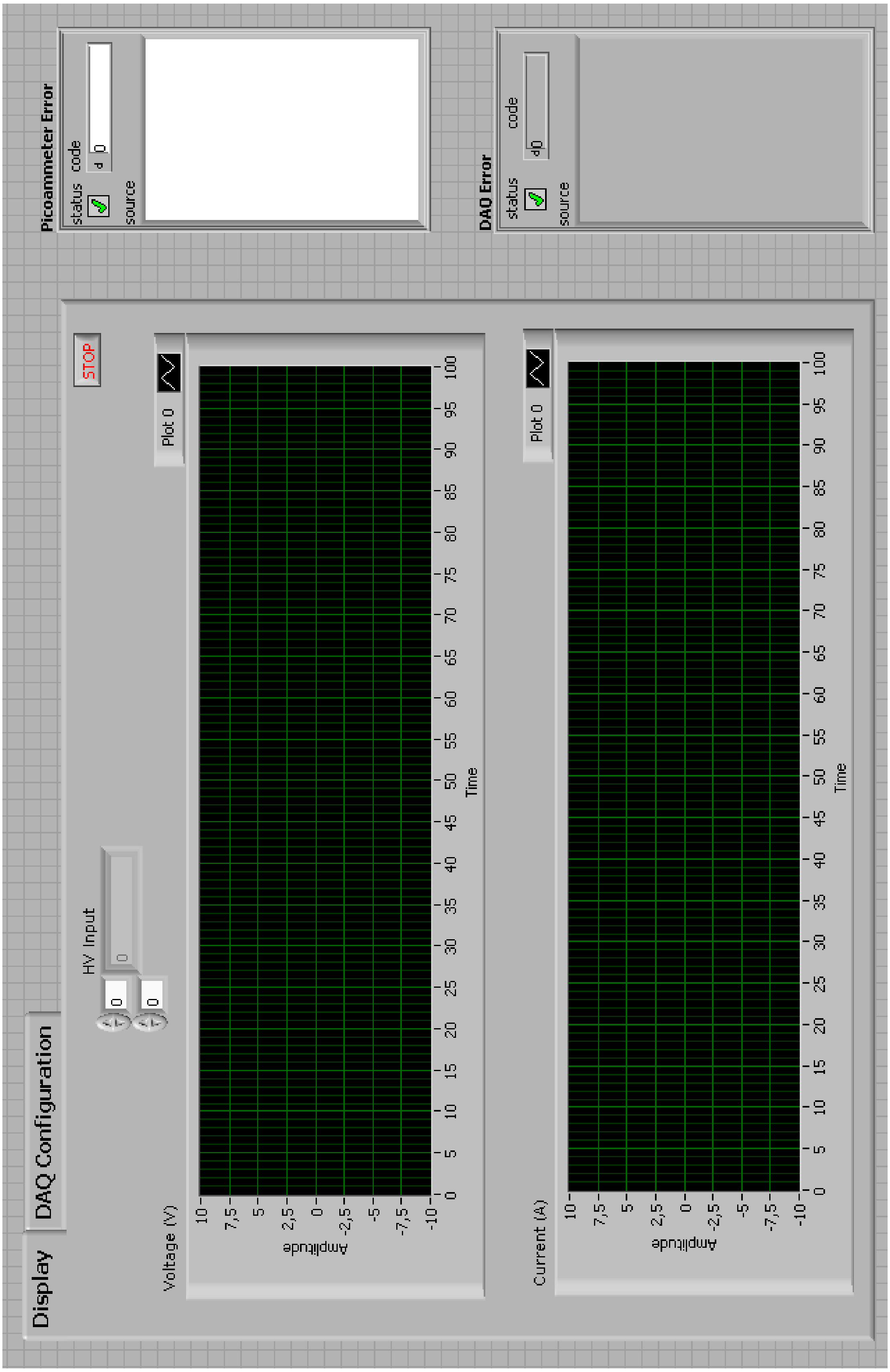

Figure 6.7: The Labview interface used for HV I/O and picoammeter readout. HV input can be changed by any specified amount. The HV and Labview readouts are plotted in the two graphs. The configuration of the I/O ports of the DAQ device can be done in the "DAQ Configuration" tab.

6.8 Data Analysis

The conditioning process changes the β and A_e parameters of Equation 6.2. The β and A_e values can be obtained by fitting $log(I/V^2)$ vs. $1/V$ data to a line (See Figure 6.8). The data in these calculations are taken by averaging current and voltage over some time intervals, where they are supposed to have a constant value. The current needs to be stable within the averaging interval, indicating the stability of the condition of the plates. The intervals were selected such that the data points corresponding to them sit on a line. So that the linearity of the data points indicates the constancy of the parameters β and A_e.

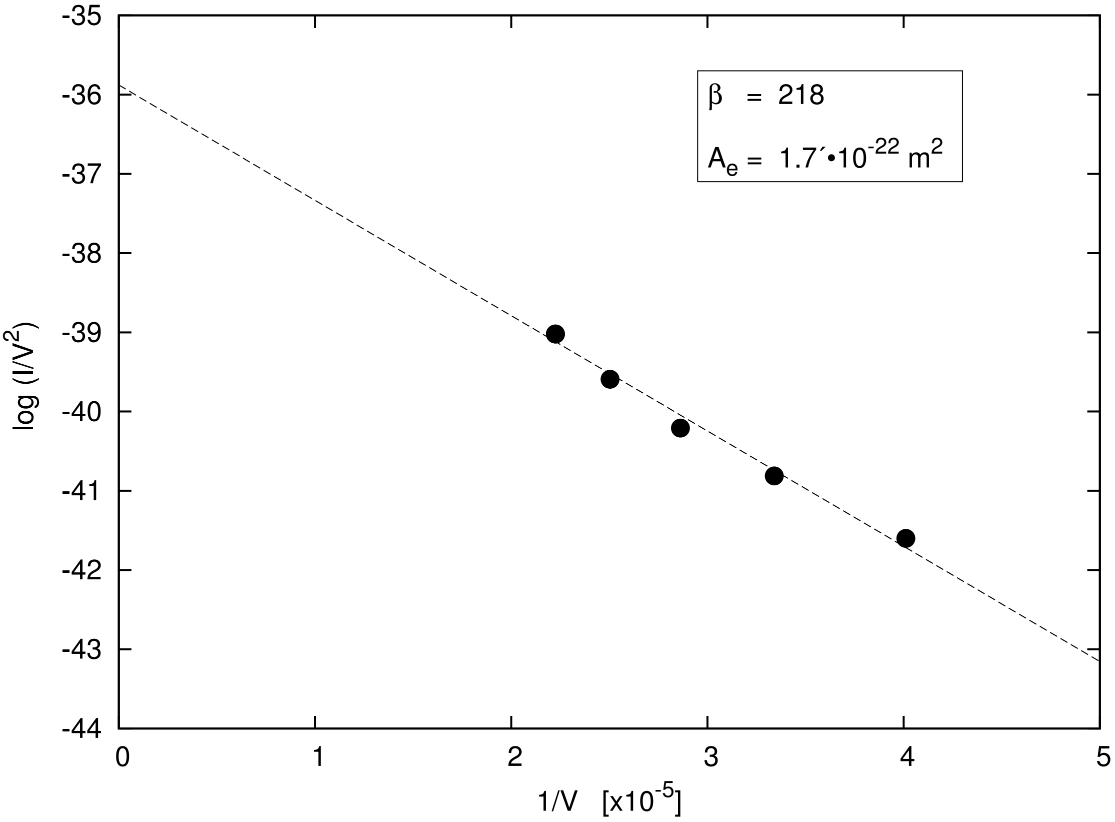

Figure 6.8: $log(I/V^2)$ vs. $1/V$ data is fitted to a line to give β and A_e values. Units of V and I are Volt and Ampere respectively. Linearity of the data shows that β and A_e are almost constant during the data taking.

6.9 Results

The conditioning has started from 1.06 mm of average gap, with plates not perfectly parallel. Initially, we could achieve about 8 MV/m of maximum E-field with 6 nA of dark current. It did not improve much until day 12 when we have made the plates

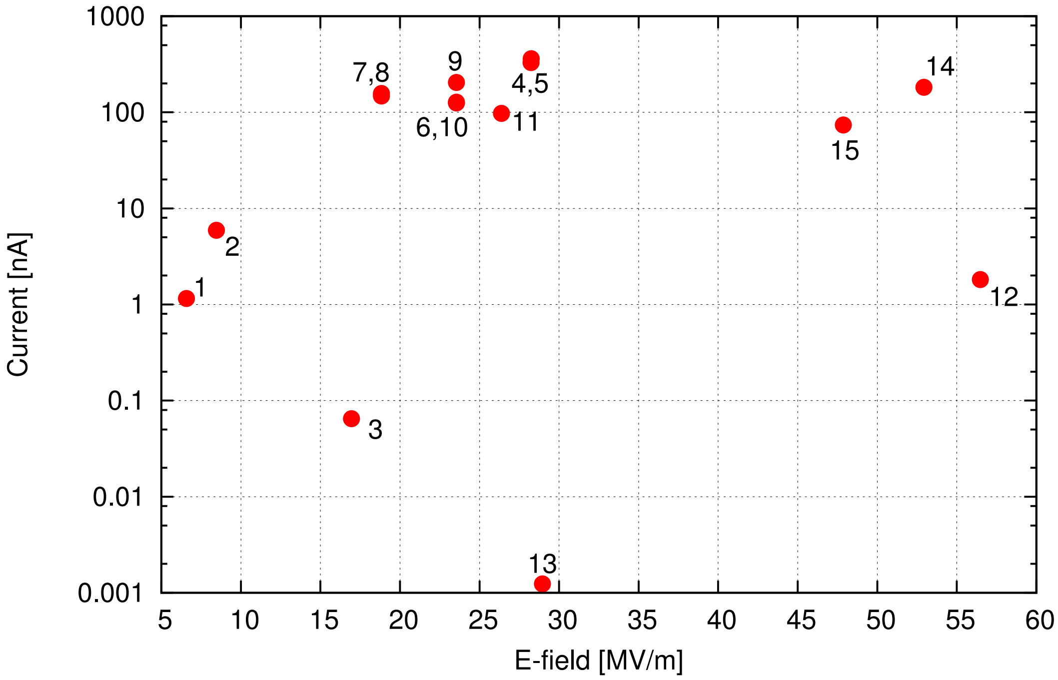

Figure 6.9: Current vs Electric field between the plates during conditioning. The numbers beside the points label the day of conditioning. The improvement from day 1 is clearly visible. The conditioning was done at 1.06mm from day 1 to 12, 4mm at day 13, and 1mm at day 14 and 15.

completely parallel at 1mm of gap (See Figure 6.9). Then, after a few sparks and some activities, the plates were conditioned to a very good state. Even at 57 MV/m, the dark current was only a few nA. It kept this condition more than 3 hours, until we turned off the system.

The next day, the gap was increased to 4mm. The plates did not need conditioning until about 25 MV/m. Then, with some more conditioning, 29 MV/m of maximum E-field was achieved at about 1 pA. We did not go further because of frequent sparking. These results are better than that were achieved by the groups mentioned above [63] [64].

At day 14 and 15, the conditioning at 1mm did not make an improvement. Finally, it was 48MV/m with 74 nA of dark current at day 15.

Figure 6.10 shows the evolution of β and A of Equation 6.2 during the conditioning. This was done by plotting $log(I/V^2)$ vs. $1/V$ data and fitting it to a line for each day.

It is seen in Figure 6.9 that in day 1 and day 2, the plates essentially are at the same condition. This is the case for the days 4-5 and 7-8 too. Those days in Figure 6.10 show that β or A_e individually may vary over time, while they correspond to the same condition of the plate.

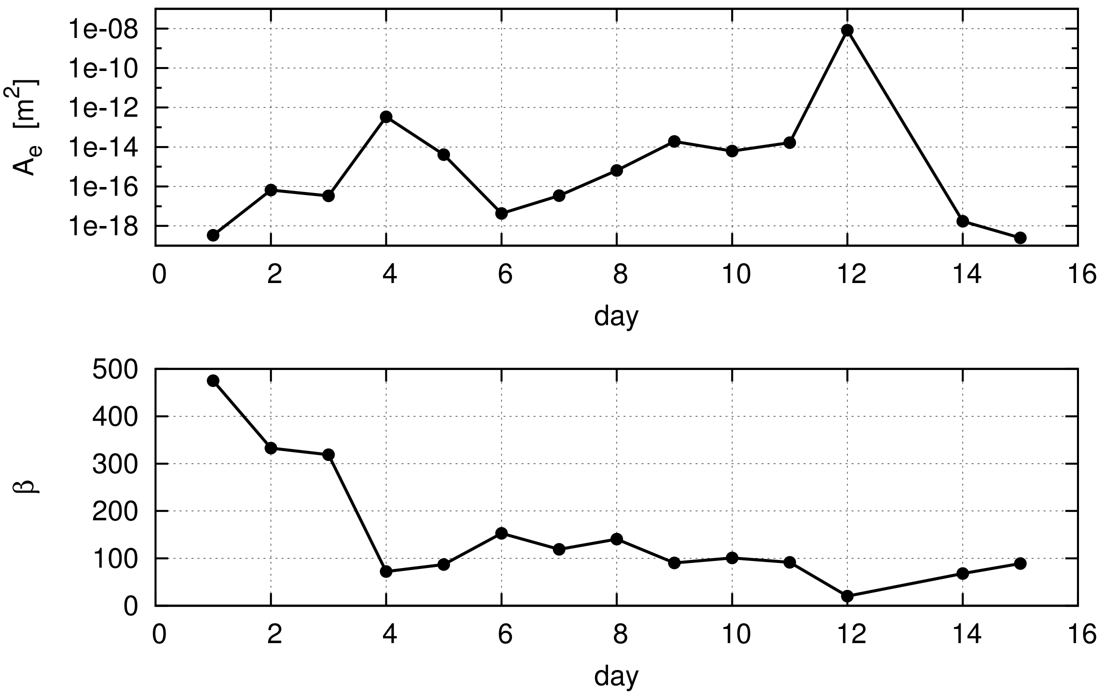

Figure 6.10: Evolution of β factor and the area of the field emitting surface A_e during conditioning. It is seen that β and A_e change individually even when the condition of the plate does not change (See days 4-5 and 7-8 of Figure 6.9). Also note that day 1 and day 15 have almost the same A_e value, while the β value has decreased by about 80%.

Figure 6.10 shows that while the A_e value is almost the same for both days, the β value at day 15 is about 20% of day 1, which means about 80% improvement in β.

7. CONCLUSIONS

There are several neutron electric dipole moment (nEDM) experiments in the world under preparation to improve the current limit of 3×10^{-26} e·cm by about two orders of magnitude. Even if the nEDM is found to be finite, by itself it will be hard to interpret it since a number of potential sources are possible. Knowing the proton and deuteron EDM will help clarify the EDM source. The storage ring EDM collaboration has proposed using an all-electric storage ring to probe the proton EDM (pEDM) with 10^{-29} e·cm sensitivity. This method provides a direct probe to charged particle EDM and it will improve the current indirect limit on the proton (using the Hg atom EDM limit) of 8×10^{-25} e·cm by several orders of magnitude.

The experiment will utilize the “Frozen Spin Method” in an all-electric storage ring. This method requires the momentum of the proton to be fixed at “magic momentum”, 0.7007 GeV/c, where the momentum and spin vectors precess at exactly the same rate horizontally. Satisfying this condition with all stored particles guarantees infinite "spin coherence time" (SCT), i.e. all particles would precess their spins in the horizontal plane at the same rate as their momentum. In practice, the momenta of all particles cannot be made precisely the same and therefore there is going to be a spread in their horizontal spin precession rates. The average momentum of the beam can be adjusted using feedback (adjusting the radio-frequency value) during storage to be made as close to "magic" as needed, but this cannot help if there is a spread in the momenta of the stored particles. In the proposed pEDM experiment, the SCT of the beam needs to be about 10^3 s, with the sensitivity scaling as the $\sqrt{SCT}$, i.e. if the SCT is improved by a factor of nine, the sensitivity is improved by a factor of three.

The first part of the thesis includes simulations on how long it will take for the horizontal spin component to precess 1 radian, with respect to the ideal particle, as a function of the particle phase-space and ring lattice parameters. The simulations were done by solving the beam and spin dynamics differential equations using the 4^{th} order Runge-Kutta method. The fringe fields were approximated to hard edges at the end of the plates. But the energy of the particle was adjusted to take into account the potential energy in the electric field region. A realistic fringe field is expected to slightly modify the lattice parameters but the main conclusions of this study should hold.

The simulation results show that the proposed frozen spin method in an all-electric ring provides a SCT that is adequate for a storage time of 10^3 seconds. Also, for a ring with a 3 cm of aperture, the acceptance of the ring is found to be about 6.2π mm mrad. Table 7.1 summarizes the SCT for various cases of $\Delta p/p$ and z_0. Note that, while SCT for $\Delta p/p = 2\times 10^{-4}$ is 58s, this will not be a problem. Because, those particles with high momentum spread are at the edge of the ring acceptance and will be taken out first (in 58s).

Table 7.1: Summary of the SCT calculations for several configurations of $\Delta p/p$ and z_0 for L_{str}=14m.

$\Delta p/p$	z_0 [cm]	Angular rate [mrad/s]	SCT [s]
0	0	≈0.1	$\approx 10^4$
0	2	≈1.1	$\approx 10^3$
2×10^{-4}	0	≈17	$\approx 0.5\times 10^2$

While the simulations were made for $Q_y = 0.2$ of vertical tune, it will be decreased to 0.1 after the first 10^2 s of storage time. Decreasing Q_y slows down the horizontal spin precession, increasing the SCT. We plan to start off with a larger Q_y in order to increase the vertical ring acceptance.

It is also seen that, there are some fundamental differences between all-electric and all-magnetic rings. One of them is the classical definition of the dispersion function. In an all-electric ring, the dispersion function shows a very different behaviour as opposed to an all-magnetic ring. Due to the significant change in the potential energy as a function of the radial direction, the particle kinetic energy is modified substantially during the horizontal betatron oscillations.

The phase slip factor is another parameter that shows different behavior in an all-electric ring having a strong dependence on $\Delta p/p$ and x_0.

Betatron oscillations also differ substantially between electric and magnetic rings. In the absence of an RF-cavity the equilibrium orbit depends on the particle initial position.

One of the most important findings in the present studies is understanding the origin of the small horizontal spin precession with respect to the momentum vector (a.k.a. g-2 precession) for particles with off-magic momentum. Specifically, for particles that have a momentum that is not exactly magic, in an all-electric ring with cylindrical symmetry and an RF-cavity present, the g-2 precession is found to be very small. Equation 3.8 suggests that the SCT is infinite for a particle with magic momentum. One may expect that for a particle with off-magic momentum, the term in parenthesis accumulates very fast due to its inherent non-linearity. However, the simulation results have shown that the $\vec{\beta} \times \vec{E}$ factor compensates to a great extend for this non-linearity resulting to a significantly larger SCT. This is a characteristics of electric rings, in which both velocity and electric field depend strongly on position. To our knowledge, this effect is first mentioned here.

All Runge-Kutta methods are slow and for high precision they require a very small time step. One way to avoid this problem is to use sequence acceleration methods, such as Richardson extrapolation. We plan to implement this method to improve the simulation execution time.

The second part of the thesis is on high voltage electric field tests on stainless steel metal plates of about 120 cm^2 surface area. When high voltage is applied to the plates, the high electric field causes dark current which initiates certain processes and that may end up in a spark. Therefore, high electric field between plates requires a clean and smooth surface in order to avoid sparks. Cleaning the surface includes initial treatments such as electropolishing, ion implantation, high pressure water rinsing etc. Another set of treatment is called “conditioning”, which can be done in several ways too. In our tests, we have applied a special spark conditioning. In some cases, the plates may be baked out too as another treatment.

Some sparks clean the plate, while some others can damage them, depending on the energy available in them. Therefore, the current must be limited to μA level during the conditioning. Even in that case, it may be damaging.

The energy of the spark is determined by $P = V \cdot I$, where V is the potential difference between the plates and I is the dark current, which depends exponentially on electric field. At small gaps such as 1-2 mm, high electric field can be achieved at smaller voltages because of $E = V/d$ dependence for parallel plates. This minimizes the damage on the plates because of the less energetic sparks.

In these tests, current conditioning was conducted for parallel plates of about 120 cm^2 of surface area at small gaps. It is seen that keeping the gap at small values like a few millimeters provides an effective conditioning. The β value, as defined by the Nordheim-Fowler equation, decreases by about 80% after conditioning. Besides, the test results (See Figure 6.9) showed that this procedure provided better plate conditioning than the above-mentioned groups [63] [64], who used similar test setups. Still, one should be cautious that the plates can be damaged in case of continuous sparking.

It is also seen in the tests that the parallellness of the plates plays an essential role in conditioning. Although the conditioning was poor for the first 11 days, once the plates were made parallel, they were cleaned in a short time.

Finally, the results also give a big enough E-field for the pEDM experiment, extrapolating to 3 cm using the fact that the electric field strength varies as using the $\propto 1/\sqrt{gap}$. However, this is an indirect answer.

REFERENCES

[1] **Yao, M.**, **Amsler, C.**, **Asler, D.**, **Barnett, R.**, **Beringer, J.**, **Burchat, P.**, **... and Carone, C.** (2006). Review of Particle Physics, *J. Phys. G: Nucl. Par. Phys.*, ***33***, 1.

[2] **Anastassopoulos, V.**, **Babusci, D.**, **Bai, M.**, **Baessler, S.**, **Berz, M.**, **Blaskiewicz, M.**, **... and Brown, K.** (2011), A Proposal to Measure the Proton Electric Dipole Moment with 10^{-29}e·cm Sensitivity by the Storage Ring EDM Collaboration, `www.bnl.gov/edm/Proposal.asp`.

[3] **Lee, T. and Yang, C.** (1956). Question of Parity Conservation in Weak Interactions, *Phys. Rev.*, ***104***(1), 254–258.

[4] **Wu, C.**, **Ambler, E.**, **Hayward, R.**, **Hoppes, D. and Hudson, R.** (1957). Experimental Test of Parity Conservation in Beta Decay, *Phys. Rev.*, ***105***, 1413–1415.

[5] **Christenson, J.**, **Cronin, J.**, **V.L, F. and Turlay, R.** (1964). Evidence for the 2π decay of the $K^0{}_2$ meson, *Phys. Rev. Lett.*, ***13***(4), 138–140.

[6] **Aubert, B.**, **Boutigny, D.**, **Gaillard, J.**, **Hicheur, A.**, **Karyotakis, Y.**, **Lees, J.**, **... and Robbe, P.** (2001). Observation of CP Violation in the B^0 Meson System, *Phys. Rev. Lett.*, ***87***(9), 091801 1–8.

[7] **Kobayashi, M. and Maskawa, T.** (1973). CP-Violation in the renormalizable theory of weak interaction, *Prog. of Th. Phys.*, ***49***(2), 652–657.

[8] **Sakharov, A.** (1967). Violation of CP in variance, C asymmetry, and baryon asymmetry of the universe, *Pis'maZh. Eksp.Teor. Fiz.*, ***5***, 32–35.

[9] **Bernreuther, W. and Suzuki, M.** (1991). The electric dipole moment of the electron, *Reviews of Moders Physics*, ***63***(2), 313–338.

[10] **Khatsymovsky, V.**, **Khriplovich, I. and Zhitnitsky, A.** (1987). Strange quarks in the nucleon and neutron electric dipole moment, *Z. Phys. C- Particles and Fields.*, ***36***, 455–460.

[11] **Donoghue, J.**, **Golowich, E. and Holstein, B.** (1981). Compendium of bag-model matrix elements of the weak nonleptonic Hamiltonian, *Phys. Rev. D.*, ***23***(5), 1213–1216.

[12] **Abel, S.**, **Khalil, S. and Lebedev, O.** (2001). EDM constraints in supersymmetric theories, *Nuc. Phys. B*, ***606***, 151–182.

[13] **Dirac, P.** (1928). The quantum theory of the electron, *Proc. R. Soc. A*, ***117***, 610.

[14] **Purcell, E. and Ramsey, N.** (1950). On the Possibility of Electric Dipole Moments for Elementary Particles and Nuclei, *Phys. Rev.*, ***78***(6), 807.

[15] **Smith, J.**, **Purcell, E. and Ramsey, N.** (1957). Experimental Limit to the Electric Dipole Moment of the Neutron, *Phys. Rev.*, ***108***(1), 120–122.

[16] **Ellis, J.** (1989). Theory of the neutron electric dipole moment, *Nuc. Instr. and Meth. in Phys. Res. A*, ***284***, 33–39.

[17] **Regan, B.**, **Commins, E.**, **Schmidt, C. and DeMille, D.** (2002). New limit on the electron electric dipole moment, *Phys. Rev. Lett.*, ***88***(7), 071805–1 – 071805–4.

[18] **Baker, C.**, **Doyle, D.**, **Geltenbort, P.**, **Green, K.**, **van der Grinten, M.**, **Harris, P.**, **... and Iaydjiev, P.** (2006). Improved Experimental Limit on the Electric Dipole Moment of the Neutron, *Phys. Rev. Lett.*, ***97***, 131801.

[19] **Griffith, W.**, **Swallows, M.**, **Loftus, T.**, **Romalis, M.**, **Heckel, B. and Fortson, E.** (2009). Improved Limit on the Permanent Electric Dipole Moment of ^{199}Hg, *Phys. Rev. Lett.*, ***102***, 11601 1–4.

[20] **Peccei, R.** (2008). *The Strong CP Problem and Axions*, volume741 of *Lecture Notes in Physics*, Springer Berlin Heidelberg, `http://dx.doi.org/10.1007/978-3-540-73518-2_1`.

[21] **Liu, C. and Timmermans, R.G.E.** (2004). P- and T-odd two-nucleon interaction and the deuteron electric dipole moment, *Phys. Rev. C*, ***70***, 055501.

[22] **Khriplovich, I. and Korkin, R.** (2000). P and T odd electromagnetic moments of deuteron in chiral limit, *Nuclear Physics A*, ***665***(3–4), 365 – 373.

[23] **Pospelov, M. and Ritz, A.** (2005). Electric dipole moments as probes of new physics, *Annals of Phys.*, ***318***, 119–169.

[24] **Ramsey, N.** (1950). A molecular beam resonance method with separated oscillating fields, *Phys. Rev.*, ***78***(6), 695–699.

[25] **Schiff, L.** (1963). Measurability of Nuclear Electric Dipole Moments, *Phys. Rev*, ***132***(5), 2194–2200.

[26] **Commins, E.**, **Jackson, J. and DeMille, D.** (2007). The electric dipole moment of the electron: An intuitive explanation for the evasion of Schiff's theorem, *Am. J. Phys.*, ***75***(6), 532–536.

[27] **Flambaum, V. and Ginges, J.** (2002). Nuclear Schiff moment and time-invariance violation in atoms, *Phys. Rev. A*, ***65***, 032113 1–9.

[28] **Ginges, J. and Flambaum, V.** (2004). Violations of fundamental symmetries in atoms and tests of unification theories of elementary particles, *Phys. Rep.*, ***397***, 63–154.

[29] **Liu, Z. and Kelly, H.** (1992). Analysis of atomic electric dipole moment in thallium by all-order calculations in many-body perturbation theory, *Phys. Rev. A*, ***45***(7), R4210–R4213.

[30] **Hudson, J.**, **Sauer, B.**, **Tarbutt, M. and Hinds, E.** (2002). Measurement of the Electron Electric Dipole Moment Using YbF Molecules, *Phys. Rev. Lett.*, ***89***(2), 23003–1 – 23003–4.

[31] **DeMille, D.**, **Bay, F.**, **Kawall, D.**, **Krause, D.**, **Maxwell, S. and Hunter, L.** (2000). Investigation of PbO as a system for measuring the electric dipole moment of the electron, *Phys. Rev. A.*, ***61***, 52507 – 1–8.

[32] **Sandars, P.** (1967). Measurablility of the proton electric dipole moment, *Phys. Rev. Lett.*, ***19***(24), 1396–1398.

[33] **Altarev, I.**, **Ban, G.**, **Bison, G.**, **Bodek, K.**, **Burghoff, M.**, **Cvijovic, M.**, **... and Daum, M.** (2009). Towards a new measurement of the neutron electric dipole moment, *Nuc. Instr. and Met. in Phys. Res. A*, ***611***, 133–136.

[34] **Bennett, G.**, **Bousquet, B.**, **Brown, H.**, **Bunce, G.**, **Carey, R.**, **Cushman, P.**, **... and Danby, G.** (2006). Final report of the E821 muon anomalous magnetic moment measurement at BNL, *Phys. Rev. D*, ***73***, 072003 – 1–41.

[35] **Bennett, G.**, **Bousquet, B.**, **Brown, H.**, **Bunce, G.**, **Carey, R.**, **Cushman, P.**, **... and Danby, G.** (2009). Improved limit on the muon electric dipole moment, *Phys. Rev. D*, ***80***, 052008 – 1–18.

[36] **Jackson, J.** (1998). *Classical Electrodynamics Third Edition*, Wiley, third edition.

[37] **Silenko, A.** (2006). Equation of spin motion in storage rings in the cylindrical coordinate system, *Phys. Rev. Spec. Top. Accel. and Beams*, ***9***, 034003–1–034003–9.

[38] **Farley, F.**, **Jungmann, K.**, **Miller, J.**, **Morse, W.**, **Orlov, Y.**, **Roberts, B.**, **Semertzidis, Y.**, **Silenko, A. and Stephenson, E.** (2004). New Method of Measuring Electric Dipole Moments in Storage Rings, *Phys. Rev. Lett.*, ***93***(5), 052001 – 1–4.

[39] **Mane, S.** (2008). Orbital dynamics in a storage ring with electrostatic bending, *Nuc. Instr. and Meth. in Phys. Res. A*, ***596***, 288–294.

[40] **Mane, S.** (2012). Orbital and spin motion in a storage ring with static electric and magnetic fields, *Nuc. Instr. and Meth. in Phys. Res. A*, ***687***, 40–50.

[41] **Edwards, D. and Syphers, J.** (2008). *An Introduction to the Physics of High Energy Accelerators*, Wiley Series in Beam Physics and Accelerator Technology, John Wiley & Sons, `http://books.google.com.tr/books?id=s0yWaw9o2ykC`.

[42] **Conte, M. and MacKay, W.** (2008). *An Introduction To The Physics Of Particle Accelerators*, World Scientific.

[43] **Fowler, R. and Nordheim, L.** (1928). Electron emission in intense electric fields, *Proc. Roy. Soc. A*, ***119***, 173–181.

[44] **Latham, R.** (1995). *High voltage vacuum insulation*, Academic Press.

[45] **Farrall, G.** (1985). Electrical breakdown in vacuum, *IEEE Trans. Electr. Ins.*, ***EI-20***, 815.

[46] **Morrow, R. and Weisser, D.** (1996). Vacuum breakdown mechanisms, and X-ray pulses in accelerators, *Nuc. Instr. and Meth. in Phys. Res. A*, ***382***, 66–72.

[47] **Cranberg, L.** (1952). The initiation of breakdown in vacuum, *J. Appl. Phys.*, ***23***(5), 518–522.

[48] **Utsumi, T.** (1967). Cathode- and anode-induced electrical breakdown in vacuum, *J. Appl. Phys.*, ***38***, 2989.

[49] **Juttner, B.** (1988). Vacuum Breakdown, *Nuc. Instr. and Meth. in Phys. Res. A*, ***268***, 390–396.

[50] **Davies, D. and Biondi, M.** (1977). Emission of electrode vapor resonance radiation at the onset of dc breakdown in vacuum, *J. Appl. Phys.*, ***48***, 4229.

[51] **Descouedres, A.**, **Ramsvik, T.**, **Calatroni, S.**, **M., T. and Wuensch, W.** (2009). DC breakdown conditioning and breakdown rate of metals and metallic alloys under ultrahigh vacuum, *Phys. Rev. Spec. Top., Acc. and Beams*, ***12***, 032001.

[52] **Pimpec, F.**, **Ganter, R. and Betemps, R.** (2007). Field emission dark current of technical metallic electrodes, *Nuc. Instr. and Meth. in Phys. Res. A*, ***574***, 7–16.

[53] **Furuta, F.**, **Nakanishi, T.**, **Okumi, S.**, **Gotou, T.**, **Yamamoto, M.**, **Miyamoto, M.**, **... and Kuwahara, M.** (2005). Reduction of field emission dark current for high-field gradient electron gun by using a molybdenum cathode and titanium anode, *Nuc. Instr. and Meth. in Phys. Res. A*, ***538***, 33–44.

[54] **Dunham, B.**, **Sinclair, C.**, **Bazarov, I.**, **Li, Y.**, **Liu, X. and Smolenski, K.** (2007). Performance of a very high voltage photoemission electron gun for high brightness, high average current ERL injection, *Proceedings of PAC07, Albuquerque, New Mexico, USA*, pp.1224–1226.

[55] **Cavailere, E.**, **Fusetti, M.**, **Michelato, P.**, **Pagani, C.**, **Pierini, P.**, **Paulon, R. and Sertore, D.** (2006). High pressure rinsing parameters measurement, *Physica C*, ***441***, 254–257.

[56] **Sinclair, C.** (2006). DC photoemission electron guns as ERL sources, *Nuc. Instr. and Meth. in Phys. Res. A*, ***557***, 69–74.

[57] **Sinclair, C.**, **Dylla, H.**, **Siggins, T.**, **Manos, D. and Verhaus, T.** (2001). Dramatic Reduction of DC field emission from large area electrodes by plasma-source ion implantation, *Proceedings of the 2001 Particle Accelerator Conference, Chicago*, pp.610–612.

[58] **Yamada, I.**, **Matsuo, J.**, **Toyoda, N. and Kirkpatrick, A.** (2001). Materials processing by gas cluster ion beams, *Mat. Sci. Eng. R*, ***34***, 231–295.

[59] **Dangwal, A.**, **Reschke, D. and Muller, G.** (2006). DC field emission scanning measurements on electropolished niobium samples, *Physica C*, ***441***, 83–88.

[60] **Williams, D. and Williams, W.** (1972). Effect of electrode surface finish on electrical breakdown in vacuum, *J. Phys. D: Appl. Phys.*, ***5***, 1845.

[61] **Steib, G. and Moll, E.** (1973). High-voltage conditioning at large gaps in industrial vacuum, *J. Phys. D: Appl. Phys.*, ***6***, 243.

[62] **Zeitoun-Fakiris, A. and Juttner, B.** (1991). On the dose of bombarding residual gas ions for infuencing pre-breakdown field emission in a vacuum, *J. Phys. D: Appl. Phys.*, ***24***, 750.

[63] **Swenson, D.**, **Wu, A.**, **Degenkolb, E. and Insepov, Z.** (2007). Gas cluster ion beam surface treatments for reducing field emission and breakdown of electrodes and SRF cavities, *Nucl. Instr. and Meth. in Phys. Res. B*, ***261***, 630–633.

[64] **Dunham, B.**, **Sinclair, C.**, **Bazarov, I.**, **Li, Y.**, **Liu, X. and Smolenski, K.** (2007). Performance of a very high voltage photoemission electron gun for a high brightness, high average current ERL injector, *Proceedings of PAC2007 Albuquerque, New Mexico, USA*, pp.1224–1226.

[65] **Press, W.**, **Teukolsky, S.**, **Vetterling, W. and Flannery, B.** (2007). *Numerical Recipes : The Art of Scientific Computing*, Cambridge University Press.

APPENDICES

APPENDIX A : CALCULATION OF E_R AND E_z

APPENDIX B : 4^{TH} ORDER RUNGE-KUTTA METHOD

APPENDIX C : SOURCE CODE FOR THE 4^{th} ORDER RUNGE-KUTTA SIMULATIONS

APPENDIX A: CALCULATION OF E_R AND E_z

Electric field between the parallel plates can be calculated from Maxwell's equations using the symmetries of the ring. The Maxwell's Equations for the electric field state that

$$\vec{\nabla}\cdot\vec{E} = \left(\frac{1}{R}+\frac{\partial}{\partial R}\right)E_R + \frac{\partial E_z}{\partial z} = 0 \qquad \textbf{A.1}$$

and

$$\vec{\nabla}\times\vec{E} = \left(\frac{\partial E_R}{\partial z}-\frac{\partial E_z}{\partial R}\right) = 0 \qquad \textbf{A.2}$$

where R and z show the radial and vertical directions in the ring and E_R and E_z are the corresponding electric fields respectively. Symmetry of the ring suggests that

$$E_R(R,-z) = E_R(R,z); E_z(R,-z) = -E_z(R,z) \qquad \textbf{A.3}$$

Using these symmetries, E_R and E_z can be expanded as

$$E_R = A_0(R) + A_2(R)z^2 + A_4(R)z^4 + ... \qquad \textbf{A.4}$$

$$E_z = A_1(R)z + A_3(R)z^3 + ... \qquad \textbf{A.5}$$

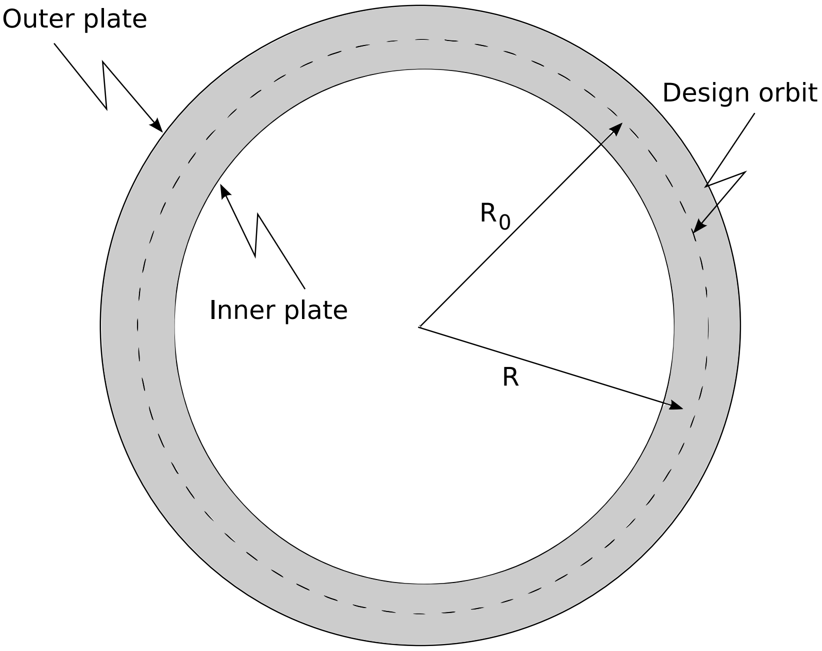

Figure A.1: The circular ring is made of parallel plates. The distance from the center of the ring to the middle of the plates is R_0. R is an arbitrary position between the plates. The electric field between the plates is both a function of radial position R and the vertical position z, out of the plane.

Rewriting the $\vec{\nabla}\cdot\vec{E}$ and $\vec{\nabla}\times\vec{E}$ with the above expansion gives

$$\vec{\nabla}\cdot\vec{E} = \frac{A_0}{R} + \frac{A_2}{R}z^2 + \frac{A_4}{R}z^4 + \frac{\partial A_0}{\partial R} + \frac{\partial A_2}{\partial R}z^2 + \frac{\partial A_4}{\partial R}z^4 + A_1 + 3A_3z^2 = 0 \qquad \textbf{A.6}$$

and

$$2A_2z + 4A_4z^3 - \frac{\partial A_1}{\partial R}z - \frac{\partial A_3}{\partial R}z^3 = 0 \qquad \textbf{A.7}$$

Assuming $A_0 = E_0\left(\frac{R_0}{R}\right)^n$ and solving the above two equations E_R and E_z are found to be:

$$E_R = E_0\left(\frac{R_0}{R}\right)^n\left[1 - \frac{n^2-1}{2}\frac{z^2}{R^2} + \frac{1}{24}(n^2-1)(n+1)(n+3)\frac{z^4}{R^4} + O(z^6)\right] \qquad \textbf{A.8}$$

$$E_z = E_0\left(\frac{R_0}{R}\right)^n\left[(n-1)\frac{z}{R} - \frac{1}{6}(n^2-1)(n+1)\frac{z^3}{R^3} + O(z^5)\right] \qquad \textbf{A.9}$$

APPENDIX B: 4^{TH} ORDER RUNGE-KUTTA METHOD

Runge-Kutta methods are iterative methods for solving ordinary differential equations numerically [65]. The order of the Runge-Kutta method gives the order of magnitude in the error over an interval of integration.

Let an initial value problem be given as follows:

$$\dot{y} = f(y,t) \tag{B.1}$$

with an initial condition of $y(t_0) = y_0$ at $t = t_0$. At any step $n+1$ of the 4^{th} order Runge-Kutta integration, t and y are given as:

$$t_{n+1} = t_n + \Delta t \tag{B.2}$$

$$y_{n+1} = y_n + \frac{\Delta t}{6}(k_0 + 2k_1 + 2k_2 + k_3) \tag{B.3}$$

where Δt is the time step, and

$$k_0 = f(t_n, y_n), \tag{B.4}$$

$$k_1 = f(t_n + \frac{\Delta t}{2}, y_n + \frac{\Delta t}{2} \cdot k_0), \tag{B.5}$$

$$k_2 = f(t_n + \frac{\Delta t}{2}, y_n + \frac{\Delta t}{2} \cdot k_1), \tag{B.6}$$

$$k_3 = f(t_n + \Delta t, y_n + \Delta t \cdot k_2) \tag{B.7}$$

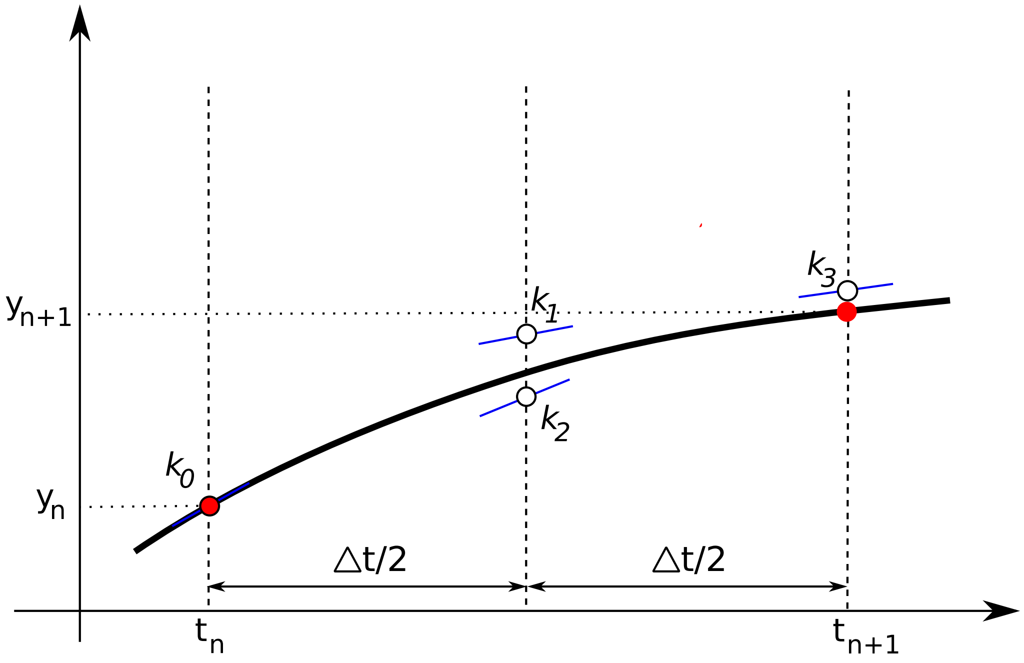

Figure B.1: The calculation begins and ends at the red spots. k_0, k_1, k_2 and k_3 are the estimated slopes corresponding to t and y values within the stepsize.

Evaluation of the function at t_{n+1} is done by estimating slopes at various points (k_0, k_1, k_2 and k_3) within the stepsize (See Figure B.1). The approximate value y_{n+1} of the next step is found by adding the weighted average of those slopes to the earlier value of y_n.

In 4^{th} order Runge-Kutta method, the error per step is on the order of $(\Delta t)^5$, hence the total error has order $(\Delta t)^4$. Note that Euler's method uses only k_0, which corresponds to a total error on the order of Δt. This shows the huge improvement achieved in the 4^{th} order Runge-Kutta method.

APPENDIX C: SOURCE CODE FOR THE 4^{th} ORDER RUNGE-KUTTA SIMULATIONS

The simulation code was written from scratch, using C/C++. Besides the main file (main.cpp), a header file (vector.h) was also written for definitions of 3-d vectorial operators such as vector initialization, dot product, cross product etc.

The initialization of some variables are done by reading a file called “parameters”. The variables should be defined using the “key” and the “value” separated by a space. Each line should include only one variable. Empty lines are allowed in the file. All the variables to be used should be declared in the function “initialize_variables()” of main.cpp. The parameters file should end with the term “#end”. Below is an example of the parameters file:

```
R0 40
eRatio .9999999995

direction -1

momError 0
dev0 1e-2
z0 2e-2
theta0 0

nSect 14

t2 1e-5
dt 1.5e-12
t_pr 10000

quadLen 1e-10

rfSwitch 0
rfLen 0.01
rfPhase 180
rfV0 1e6
rfHarmonic 1

strLen .1
E0_power 1.06

contSwitch 0

#end
```

Full version of the code is provided in a CD. The source code main.cpp is as follows:

```
#include <iostream>
#include <cstdlib>
#include <cmath>
#include <fstream>
#include <string>
#include "vector.h"
using namespace std;
//====================================
#define eV 6.24150974e18  // joule to eV
long double Q=1.602176487e-19;  // electron charge
long double M1=1.672621637e-27;  // proton mass in kg
long double M2=0.938272013705579; // proton mass in GeV/c^2
long double C=299792458;      // speed of light
long double AMU=1.7928473565;    // (g-2)/2
long double R0=28.;          // radius of the bending section
long double TOL=1e-4;         // m (to be chaged in the code)
long double beta0,p_magic,E0,GAMMA,strLen=0.,rfLen=0.,eRatio=1,
quadK=.508e17, rfPhase=90,rfOmega=0,rfE0=1e7,rfV0=1e7,rfTime=1,
revTime=1,momError=0, mPot=-1.2,dev0=0,z0=0;
int rfHarmonic=4,rfSwitch=0, t_pr, revTimeCalculated=0,
nSect,quadSwitch=0,contSwitch=0,index,direction, isCW=0,isCCW=1;
double t1,t2,dt,E0_power=0,quadA=1,quadE0=0,quadLen=0,R_sh=1,
R_str=1, thS, thB, betaMagic, theta0, t_glob;
ofstream fout, rfOut("rf"); // prints after rf
ofstream gammaOut("tRev_vs_gamma"); // prints at bending section
//====================================
int sign(long double x){ if (x<0) return -1; return 1;}
//====================================
double atan3(long double y, long double x){
double a=atan2(y,x); if (a<0) a+=2*M_PI; return a;}
//====================================
int initialize_variables(){
  string key,explanation; long double E_tot, value;
  ifstream fin("parameters"); cout.precision(10);   key="";
  if(!fin.is_open()){
    cout<<"ERROR: file named 'parameters' not found\n";
    return -1;  }
 // file named 'parameters' is read and using the keywords,
 // initial values of various parameters are given
  while((!fin.eof())&&(key.compare("#end"))){
    fin >> key >> value;
    cout<<key<<"\t"<<value<<endl;
    if (!key.compare("R0")) R0=value;
    if (!key.compare("direction")) direction=value;
    if (!key.compare("eRatio")) eRatio=value;
    if (!key.compare("strLen")) strLen=value;
    if (!key.compare("t2")) t2=value;
    if (!key.compare("dt")) dt=value;
    if (!key.compare("t_pr")) t_pr=value;
    if (!key.compare("rfLen")) rfLen=value;
    if (!key.compare("rfPhase")) rfPhase=value*M_PI/180.;
    if (!key.compare("rfV0")) rfV0=value;
    if (!key.compare("rfHarmonic")) rfHarmonic=value;
    if (!key.compare("rfSwitch")) rfSwitch=value;
    if (!key.compare("momError")) momError=value;
    if (!key.compare("dev0")) dev0=value;
    if (!key.compare("z0")) z0=value;
    if (!key.compare("theta0")) theta0=value;
    if (!key.compare("E0_power")) E0_power=value;
```

```
      if (!key.compare("quadK")) quadK=value;
      if (!key.compare("quadLen")) quadLen=value;
      if (!key.compare("quadSwitch")) quadSwitch=value;
      if (!key.compare("contSwitch")) contSwitch=value;
      if (!key.compare("nSect")) nSect=value;  }
  isCW=(1+direction)/2; isCCW=(1-direction)/2; mPot=-(1+E0_power);
  rfPhase-=isCW*M_PI;  // if clockwise, change phase
  p_magic=M2/sqrt(AMU);  E_tot=sqrt(p_magic*p_magic + M2*M2);
  GAMMA=E_tot/M2;  beta0=betaMagic=p_magic/E_tot;
  revTime=(2*M_PI*R0+nSect*strLen)/(beta0*C);
  E0=-eRatio*(p_magic*beta0 / R0)*1e9;
  rfOmega=rfHarmonic*2*M_PI/revTime; // gives wrong results if
// rfHarmonic!=1, it should be fixed for rfHarmonic>1
  // add error to momentum p_magic
  p_magic*=(1+momError);  E_tot=sqrt(p_magic*p_magic + M2*M2);
  GAMMA=E_tot/M2;  beta0=p_magic/E_tot;
  // error added in p_magic
  fin.close(); return 0;}
//===================================
void print_data(double t, double dev, int zone, cVector beta, cVector
r, cVector s, cVector E,double &eKin,double &ePot, int index){
  long double bdots,angle,phase,gamma=1./sqrt(1-beta*beta),
mom=gamma*beta.magnitude()*M2,angleBeta, angleS, rDotBeta, rDotS;
  static long double Y1=0,Y4=0; int nCycle;
  cVector betaY(0,beta.y,0), sY(0,s.y,0);
  bdots=(beta*s)/(sqrt(beta*beta)*sqrt(s*s));
   rDotBeta=(beta*r)/(beta.magnitude()*r.magnitude());
   rDotS=(s*r)/(s.magnitude()*r.magnitude());
   angle=acos(rDotS)-acos(rDotBeta);  // angle with sign
   Y1+=t_pr*dt*Q/M1/C*beta0*E0*(AMU-M2*M2/mom/mom);
   phase=rfOmega*t+rfPhase; // shows when the particle gets into rf
   nCycle=(int)(.5*phase/M_PI);  // decrease the value of phase
   phase-=nCycle*2*M_PI;      // to a value between 0 and 2pi
      fout<<t<<"\t"<<r.x<<"\t"<<r.y<<"\t"<<r.z <<  // 1-4
      "\t"<<beta.x<<"\t"<<beta.y<<"\t"<<beta.z<<   // 5-7
      "\t"<<dev<<"\t"<<beta.magnitude()<<"\t"<<index<< // 8-10
      "\t"<<s.x<<"\t"<<s.y<<"\t"<<s.z<<// 11-13
// don't put new parameters above, or change the readFile function too
      "\t"<<bdots<<"\t"<<angle<< // 14-15
      "\t"<<E.x<<"\t"<<E.y<<"\t"<<E.z<<"\t"<< sqrt(E*E)<<// 16-19
      "\t"<<ePot*eV<<"\t"<< eKin*eV<<"\t"<<mom<<  // 20-22
      "\t"<<phase<<"\t"<<zone<<"\t"<<  // 23-24
      "\t"<<Y1<<"\t"<<endl; // 25
}
//===================================
void set_angles(){
// sets the array of beg. and ending angles of plates using R0
// R0, strLen and nSect also calculates R_sh
  cout.precision(20);
  R_sh=.5*strLen/sin(M_PI/nSect);  R_str=R_sh*cos(M_PI/nSect)+R0;
  thS=2*atan2(.5*strLen,R_str);  thB=2*M_PI/nSect-thS; }
//===================================
void rotate_ring(cVector &b, cVector &r, cVector &s, double angle){
  b.rotate(angle); r.rotate(angle); s.rotate(angle);}
//===================================
cVector db_dt(cVector beta, cVector null, cVector E){
 // db/dt (relativistic lorentz equation)
 return (E - (beta*(beta*E)))* Q/(M1*GAMMA*C) ;}
//===================================
```

```
cVector ds_dt(cVector beta, cVector s, cVector E){
 // ds/dt (T-BMT equation with B=0 and no edm effect)
 return -s^((beta^E)*(AMU + 1./(GAMMA+1)))*Q/(M1*C);}
//===================================
double V_rf(cVector &r, double t){
 // change of potential in the rf cavity
  return rfV0*cos(rfOmega*t+rfPhase);}
//===================================
void find_angles(cVector r,double &plateAng,double &theta,int &index){
  double R=r*r, signY=sign(r.y);
  theta=atan3(r.y,r.x); // global coordinate of the particle in ring.
  plateAng=(index+.5)*(thS+thB); // angle of the mid. point of plate.
  r.x-=R_sh*cos(plateAng);   r.y-=R_sh*sin(plateAng);
  theta=atan3(r.y,r.x);  // local coordinates of the particle
}
//===================================
cVector get_E(cVector r, double &dev, int index){
/* the angle of the particle (theta) between the middle of the str.
sections.  plateAngle is the angle of the center of the plate */
  cVector E(0.,0.,0.);  double n, E_r, R, theta, plateAngle;
  cout.precision(10);
//************ for bending section ******************
  find_angles(r, plateAngle, theta, index); // where is the particle
  r.x-=R_sh*cos(plateAngle);r.y-=R_sh*sin(plateAngle); // local coord.
  dev=sqrt(r.x*r.x+r.y*r.y)-R0; // deviation from the ideal orbit
 R=R0+dev;n=E0_power;E_r=E0*pow(R0/R,n)*(1 -.5*(n*n-1)*pow(r.z/R,2) +
(n*n-1)*(n+1)*(n+3)*pow(r.z/R,4)/24 );
  E.z=E0*pow(R0/R,n)*((n-1)*(r.z/R) - (n*n-1)*(n+1)*pow(r.z/R,3)/6);
 E.x=E_r*cos(theta);  E.y=E_r*sin(theta); // E-field
//************ for bending section ******************
  return E;}
//===================================
double get_ePot(cVector r,double dev){// pot. en. in the bending sect.
  double R=dev+R0, n=E0_power;
  return -Q*E0*pow(R0/R,n) * (R/(1-n) + .5*(n-1)*r.z*r.z/R -
(n*n-1)*(n+1)*pow(r.z,4)/pow(R,3)/24) + Q*E0*R0/(1-n); }
//===================================
void change_beta_y(cVector &b, double eKin){
// keeps b.x and b.y constant, changes b.y accor. to value of kin. en.
  double beta;  GAMMA=1+eKin/(M1*C*C);
  beta=sqrt(1 -1./(GAMMA*GAMMA));//new beta corr. to the new kin. en.
  b.y=sqrt(beta*beta - b.x*b.x - b.z*b.z)*sign(b.y);} //update velocity
//===================================
void nullify_potential(cVector &b,double &eKin,double &ePot){
//when the particle enters the str. sect., its pot. en. should be zero
  eKin+=ePot; ePot=0;  // Epot=0, Etot=const
  change_beta_y(b,eKin); }// update beta value
//===================================
void share_total_energy(cVector &b, cVector r,double &eKin,double
&ePot){
 // changes the value of pot. en. from zero to non-zero
 // when it enters the bending section
  double dev=fabs(r.x)-R_str; // calculate deviation
  // the energy was totally kin. now, substract the pot. part
  ePot=get_ePot(r,dev);eKin-=ePot;change_beta_y(b,eKin);} //update beta
//===================================
void add_rf_energy(cVector &b, cVector r, double t,double &eKin){
//the energy of the particle changes when it passes through rf cavity
  double beta,phase; eKin+=rfSwitch*Q*V_rf(r,t);// change the kin.en.
```

```
   phase = fmod((double)(rfOmega*t+rfPhase),2*M_PI)*180./M_PI;
   change_beta_y(b,eKin); }// update beta value
//===================================
int check_boundary(double &t, cVector &beta, cVector &r,cVector
&s,double &eKin,double &ePot, double &dev, int &index, cVector
&rPrev, cVector &betaPrev, cVector &sPrev){
 // checks if the particle is at the boundary
   double delta_t, t_init=t, smallQuadLen=1e-4, theta, plateAngle,
rotateAngle,angleDifference=0,endOfPlate=(index+1-isCW)*2*M_PI/nSect;
int rfOn=0,stepRatio=100000;static int nCycle=0,nStep=0,smallSteps=0;
   cVector v(0,0,0),Erf(0.,0.,0.),delta_v(0,0,0),delta_s(0,0,0);
   cout.precision(10);nStep++;find_angles(r, plateAngle, theta, index);
   angleDifference=fabs(endOfPlate-theta);
   // angle between the angle of the particle and
   // the end of the bending section w.r.t. the ring center
   if (angleDifference >2*TOL/R0) return 0;//particle not at boundary
  else{  // if at the boundary
   if (!smallSteps){ // if big steps
/*here we decrease the step size at the edge of the bend.sect. to
increase the precision. once it passes to the str. sect., the step
size will be increased again (see end of this function) */
    r=rPrev; beta=betaPrev; s=sPrev; t-=dt;  // take one step back
    TOL/=stepRatio;dt/=stepRatio;smallSteps=1;return -1;} }
//comes to this line only if it is at the boundary with small steps.
 // each bending section has an index number
   index=(nSect+index-direction)%nSect;  // update index at each jump
   if (index==(isCCW-1+nSect)%nSect) rfOn=1;// if final plate: rf=on
   rotateAngle=index*(thS+thB)*isCCW-(nSect/2-index-1)*(thS+thB)*isCW;
   // the particle is about to enter the straight section
   rotate_ring(beta,r,s,-rotateAngle);//now the str. sect. is vertical
   dev=fabs(r.x)-R_str; ePot=get_ePot(r,dev);
   nullify_potential(beta,eKin,ePot); //Epot=0, starting the str. sect.
   v=beta*C;
   // jump to rf over straight section, update t and r
   delta_t=(.5*strLen-quadLen)/(fabs(v.y)); t+=delta_t; r=r+v*delta_t;
   // jump over rf
   if (rfOn) add_rf_energy(beta,r,t,eKin);//change E_kin and velocity
   v=beta*C;               // update velocity
   // jump from rf to the end over straight section
   delta_t=(.5*strLen-quadLen)/(fabs(v.y)); // time to jump to the end
   t+=delta_t;r=r+v*delta_t; // update t and r
   dev=fabs(r.x)-R_str; share_total_energy(beta,r,eKin,ePot);
   // passed the str. sect. and there is pot. en.
   rotate_ring(beta, r, s, rotateAngle); // rotate the ring back
   TOL*=stepRatio;dt*=stepRatio;smallSteps=0;// replace the stepsize
   return 1;}
//===================================
int read_file(double &t, cVector &r, cVector &beta, cVector &s){
//reads output file to continue the simulation. requires *nix platform
double empty;system("tail -n 2 output | head -n 1 >output_last_line");
   ifstream last("output_last_line");
   last >> t >> r.x >> r.y >> r.z >> beta.x >> beta.y >> beta.z >>
empty >> empty >> index >> s.x >> s.y >> s.z;
   last.close();t_glob=t;GAMMA=1./sqrt(1-beta*beta);
   system("rm output_last_line");
   if (t>=t2){
   cout<<"\n ERROR: \n Cannot continue the earlier  simulation...\n\n";
   return -1; }
  return 0; }
```

```
//===================================
double RK4(int t_pr, double t1, double t2, cVector &s, cVector &beta,
cVector &r){
cVector b1(0,0,0), b2(0,0,0), b3(0,0,0), b4(0,0,0),beta_(0,0,0);
cVector s1(0,0,0), s2(0,0,0), s3(0,0,0), s4(0,0,0),s_(0,0,0);
cVector r1(0,0,0), r2(0,0,0), r3(0,0,0), r4(0,0,0),r_(0,0,0);
cVector E(0,0,0),db(0,0,0),ds(0,0,0),dr(0,0,0),
rPrev(0,0,0),betaPrev(0,0,0), sPrev(0,0,0);
// s,beta and r are the values of spin, beta and position in 3d
int i=0,zone,isAtBound=0,nCycle=1;
double t,dev=0,deltaEKin=0,eKin,ePot,dev_,t_pr_default=t_pr,tRf,tRev;
  fout.setf(std::ios::scientific);   fout.precision(10);
  if (index==-1) index=nSect/4;
  for (t=t1; t<t2; t+=dt){  // simulation time
    t_glob=t; deltaEKin=0;
    if (strLen && !contSwitch) isAtBound=check_boundary(t,beta,r,s,
    eKin,ePot,dev,index, rPrev, betaPrev, sPrev);
  if (contSwitch){isAtBound=-2; contSwitch=0;}
  if (isAtBound==-1) continue;
    if ((isAtBound==1) && (strLen>0.)) {
      if (!index) nCycle++;
      print_data(t,dev,zone,beta,r,s,E,eKin,ePot,index);
      t-=dt; continue; }
//*   RK4
    r1=beta*C*dt; E=get_E(r+r1/2,dev,index);
    s1=ds_dt(beta,s,E)*dt; b1=db_dt(beta,s,E)*dt;
    r2=(beta+b1/2)*C*dt; E=get_E(r+r2/2,dev_,index);
    s2=ds_dt(beta+b1/2,s+s1/2,E)*dt;   b2=db_dt(beta+b1/2,s,E)*dt;
    r3=(beta+b2/2)*C*dt;   E=get_E(r+r3/2,dev_,index);
    s3=ds_dt(beta+b2/2,s+s2/2,E)*dt; b3=db_dt(beta+b2/2,s,E)*dt;
    r4=(beta+b3)*C*dt;   E=get_E(r+r4/2,dev_,index);
    s4=ds_dt(beta+b3,s+s3,E)*dt; b4=db_dt(beta+b3,s,E)*dt;
    ds=(s1 + s2*2 + s3*2 + s4)/6; db=(b1 + b2*2 + b3*2 + b4)/6;
    dr=(r1 + r2*2 + r3*2 + r4)/6;    //   RK4 */
    ePot=get_ePot(r,dev);eKin=M1*C*C*(GAMMA-1);
    rPrev=r; betaPrev=beta; sPrev=s; s=s+ds; beta=beta+db;
   GAMMA=1./sqrt(1-beta*beta); r=r+dr;// gamma and position updated
    if(!(i%t_pr) && (t>0))  // printing condition
      print_data(t+dt,dev,zone,beta,r,s,E,eKin,ePot, index);
    i++; }
  fout.close();   rfOut.close(); gammaOut.close();   }
//===================================
int main(){
  t1=0; t2=1e-5; dt=.5e-12;t_pr=20000;// t_pr: printing period
  if (initialize_variables()==-1) return -1;
  TOL=beta0*C*dt;  /* for boudary decisions*/ set_angles();
  cVector s(direction*1,0,0),beta(direction*beta0*cos(theta0),
  beta0*sin(theta0),0),r(0,(R0+R_sh+dev0),z0); // initial values
 index=-1;
  if(!contSwitch)fout.open("output");// if the simul. isnt continuation
 else {  if (read_file(t1,r,beta,s)) return -1;
  fout.open("output", ios::app); }
  RK4(t_pr,t1,t2, s, beta, r); // loop with 4th order runge-kutta
  return 0; }
```

CURRICULUM VITAE

Name Surname: Selçuk Hacıömeroğlu

Place and Date of Birth: İstanbul - 09.12.1975

E-Mail: haciomeroglus@itu.edu.tr

B.Sc.: Middle East Technical University- Physics Programme

M.Sc.: Marmara University University- Physics Programme

Professional Experience: Research Assistant (2005-2013)

List of Publications and Patents:

PUBLICATIONS/PRESENTATIONS ON THE THESIS

- **Hacıömeroğlu S.**, Semertzidis Y.K., 2011: Proton EDM Simulations Using Fourth-Order Runge-Kutta Integration
  Proceedings of 7th Patras Workshop on Axions, WIMPs and WISPs, June 27-July 2, 2011 Mykonos, Greece.
- **Hacıömeroğlu S.** 2012: Spin tracking and testing of electrostatic deflectors for pEDM at BNL
  Workshop - EDM Searches at Storage Rings, October 1-5, 2012 Trento, Italy.